Check for updates

View Article Online
View Journal

Journal of
Materials Chemistry A

Materials for energy and sustainability

Accepted Manuscript

This article can be cited before page numbers have been issued, to do this please use: B. Singh, T. Fischer and S. Mathur, *J. Mater. Chem. A*, 2025, DOI: 10.1039/D5TA01081K.

This is an Accepted Manuscript, which has been through the Royal Society of Chemistry peer review process and has been accepted for publication.

Accepted Manuscripts are published online shortly after acceptance, before technical editing, formatting and proof reading. Using this free service, authors can make their results available to the community, in citable form, before we publish the edited article. We will replace this Accepted Manuscript with the edited and formatted Advance Article as soon as it is available.

You can find more information about Accepted Manuscripts in the Information for Authors.

Please note that technical editing may introduce minor changes to the text and/or graphics, which may alter content. The journal's standard Terms & Conditions and the Ethical guidelines still apply. In no event shall the Royal Society of Chemistry be held responsible for any errors or omissions in this Accepted Manuscript or any consequences arising from the use of any information it contains.

ROYAL SOCIETY OF CHEMISTRY

rsc.li/materials-a

View Article Online
DOI: 10.1039/D5TA01081K

ARTICLE

# Field-enhanced Chemical Vapor Deposition: New Perspectives for Thin Film Growth

Received 00th January 20xx,
Accepted 00th January 20xx

DOI: 10.1039/x0xx00000x

Bhupendra Singh[a], Thomas Fischer[a], Sanjay Mathur[a, b]*

Chemical vapor deposition (CVD) is a versatile technique for producing thin films and coatings of functional materials with diverse mechanical, electrochemical, electrical, tribological, and optical properties. The CVD process is governed by various experimental parameters including precursor chemistry, feed rate, growth temperature, pressure, and carrier or reactive gases. The growth kinetics depends on precursor decomposition that can be influenced by plasma-chemical or photo-dissociation processes to supplement thermal energy. More recently, the application of electric or magnetic fields during the CVD process has impacted the film growth beyond the conventional parametric space. This review highlights the influence of external field effects (plasma, photo-radiations, electric field, and magnetic field) on key steps of thin film processing, such as nucleation, grain growth, texture, density, phase formation, anisotropy, and kinetic stabilization. Emphasis is on recent technical, material, and phenomenological innovations in CVD technique, with applied fields as extrinsic processing parameters offering new insights gained into the future directions in research and development of high-fidelity functional films and coatings.

## 1. Introduction

Chemical vapor deposition (CVD) and its variants represent a platform technology to deposit a diverse range of materials as thin films and coatings that find large-scale applications from the food industry (e.g., antibacterial coatings) to precision-engineered semiconductor devices (e.g., light emitting diodes).[1–6] By definition, CVD involves the deposition of a solid material by vapor phase decomposition of chemical species (precursors) on a substrate maintained at a specific temperature. When compared with the physical vapor deposition techniques, such as evaporative deposition, sputtering, and pulsed laser deposition involving the generation of a plume of atomic or molecular species from a source material followed by their deposition (condensation) on a substrate, the CVD process relies upon chemical reactions of gaseous or aerosol precursors, occurring in gas phase and/or onto the substrate surface (Fig. 1 (a)).[2,7]

The fundamental parameters controlling the CVD process are the temperature of the substrate, pressure in the CVD reactor, precursor feed rate (flux), and the chemical nature of used precursors, as well as carrier gas that can be reactive or non-reactive. The film growth rates are governed by chemical kinetics and energy input that influence the characteristics of the material, such as adhesion, morphology, microstructure, and crystallinity.[8–13]

The CVD technique encompasses numerous phenomenologically related processes (Fig. 1 (a))[2,14] that differ in energy input provided to activate the chemical precursors thermally, optically, or photochemically, resulting in different categories of CVD processes (Fig. 1 (b)). In conventional CVD reactors, thin film deposition proceeds by thermal energy provided by resistive heating of the entire reaction zone (hot-wall CVD) or through a susceptor that selectively heats the substrate (cold-wall CVD). Alternatively, utilization of photons or plasma to decompose precursor species has led to the development of photo-assisted CVD (PACVD) and plasma-enhanced CVD (PECVD). The modification of CVD reactors and processes is largely driven by the necessity of achieving conformal coverage and chemically homogeneous deposition, which relies on the vapor pressure and chemical reactivity of the used precursor gases and chemicals. In addition, the necessity of applying functional coatings on temperature-sensitive substrates (e.g., aluminum, glass, polymers) has triggered the use of non-thermal plasmas (so-called cold plasma) in the CVD processes. The benefits of plasma-enhanced processes are two-fold: they can activate the substrate surface before deposition, remove any adsorbate layer that is inevitably present, and facilitate the growth kinetics. The attempts to diversify the range of precursors and to have greater control over the precursor chemistry, overcoming the barriers of non-volatility of precursors, have led to the development of aerosol-assisted CVD (AACVD) and metalorganic CVD (MOCVD). Similarly, the requirements for substrate cleaning in the semiconductor industry and the non-thermal initiation step in polymerization of thermally sensitive materials have led to the development of low energy and/or pulsed plasma CVD.[15–17]

[a] Institute of Inorganic and Materials Chemistry, University of Cologne, Greinstraße 6, 50939 Cologne, Germany.
[b] Department of Metals and Materials Engineering, Indian Institute of Technology Madras, 600036 Chennai, India.
* Corresponding author, Email: sanjay.mathur@uni-koeln.de

Open Access Article. Published on 15 2025. Downloaded on 2025/6/3 7:37:30.
This article is licensed under a Creative Commons Attribution 3.0 Unported Licence.

Journal of Materials Chemistry A Accepted Manuscript

View Article Online
DOI: 10.1039/D5TA01081K

Open Access Article. Published on 15 2025. Downloaded on 2025/6/3 7:37:30.
This article is licensed under a Creative Commons Attribution 3.0 Unported Licence.

Journal of Materials Chemistry A Accepted Manuscript

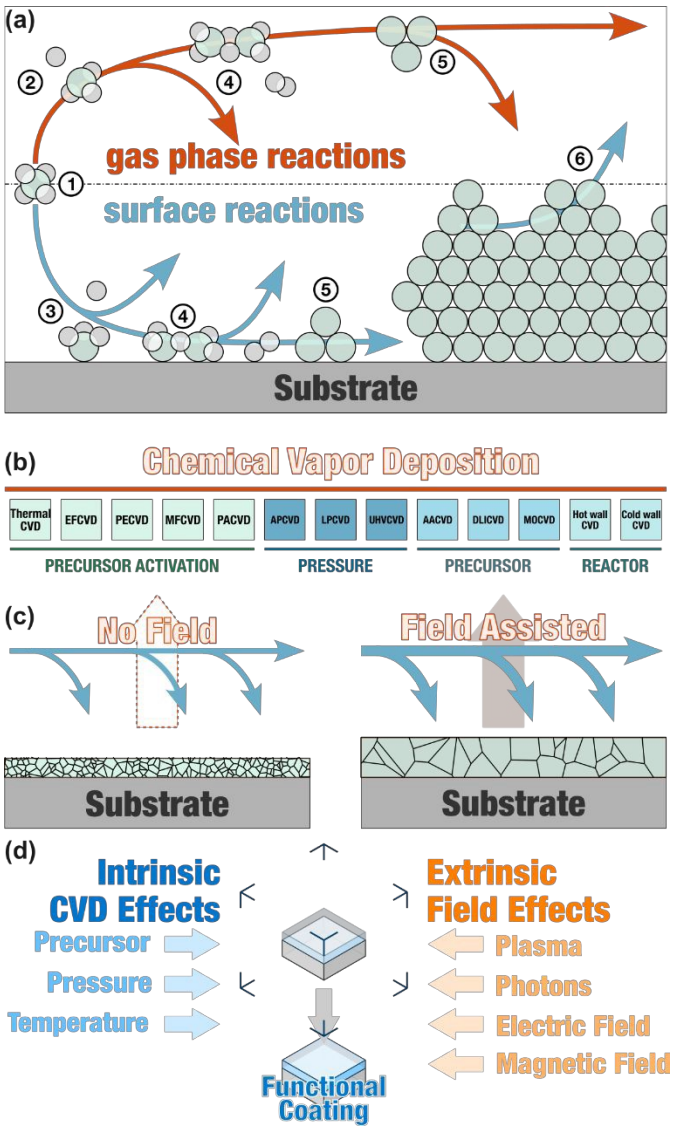


In thermal CVD, the role of temperature has been to fulfill the energy requirements for precursor decomposition, although it has further influenced the nucleation and growth kinetics.[18–20] Temperature and other precursor-specific intrinsic parameters (composition, flow rate, precursor chemistry, etc.) are thermodynamics-dependent and often need macro-level control to execute micro-level variations in properties of the resulting deposition. On the other hand, the characteristics of precursor-independent extrinsic parameters (photons, plasma, electric field, magnetic field) are controlled, independent of thermodynamics (Fig. 1(c), (d)). Therefore, while using photon or plasma as an agent fulfilling the energy requirements, manipulations in their characteristics have provided additional means to manipulate and control the CVD process at the microscopic level. For example, besides providing energy for precursor decomposition, plasma also provides energetic species–electrons, photons, ions, excited atoms, and molecules–to the substrate/growth surface, causing surface reconstruction, stoichiometric change, and alteration in reaction rate and growth kinetics. Moreover, the interaction of precursor with plasma species initiates an alternative decomposition pathway, enabling the deposition without temperature assistance or at a significantly lowered temperature.[15] Similarly, the use of laser radiations for precursor dissociation localizes the thermal energy and generates free carriers that further influence the thermodynamics and kinetics of the CVD steps.[21] Additionally, photolysis and photosensitization reduce the energy of activation ($E_a$) of gaseous or surface-adsorbed species, accelerating the reaction kinetics.[22]

*Fig. 1: (a) Schematic of general elementary steps of a typical CVD process consisting of (1), decomposition (2), absorption (3), and intermolecular reactions (4), cluster formation (5) and diffusion (6). (b) Classification of various CVD processes, categorized according to precursor activation, pressure, precursor delivery and reactor type; PECVD, RPECVD- remote plasma enhanced CVD, APCVD- atmospheric pressure CVD, LPCVD- low pressure CVD, UHVCVD- ultrahigh vacuum CVD, AACVD- aerosol-assisted CVD, DLICVD- direct liquid injection CVD, MOCVD- metalorganic chemical vapor deposition. (c) and (d) Schematic representation of intrinsic CVD process parameters and extrinsic field effects enabling an auxiliary control over the CVD process.*

The energy associated with an electric field (EF) or magnetic field (MF) generated in a normal laboratory environment may not be sufficient to overcome the $E_a$ for precursor decomposition in CVD. However, when applied in CVD environment, the field associated with them interacts with various components (precursor, decomposition products, substrate, plasma, etc.), influencing the growth rate or modifying the film properties.[23] For example, an external EF-assisted bias-enhanced nucleation has been key in the ''seed-free'' deposition of diamond on smooth surfaces.[24,25] Similarly, the application of MF in the course of precursor flow or around the substrate, inside the reactor, has provided directional control over the movement of polar/charged species, altering the deposition and growth parameters.[26] Moreover, coupling of an external MF with other CVD modulators, such as EF,[27,28] plasma,[29,30] or both,[26,31] has generated a synergistic effect, imparting unique microstructure and morphology to the deposited films.

The development of novel functional materials for targeted applications drives the need for new strategies to modulate the CVD process beyond conventional control parameters. In this context, the use of plasma and photo-irradiation, as well as the integration of external electric (EF) and magnetic fields (MF) into CVD setups, has shown significant potential to control intrinsic materials characteristics. These external fields can influence reaction kinetics and overcome constraints of conventional CVD methods, enabling, low-temperature deposition, alternative nucleation and growth mechanism, selected area deposition, directional grain growth, molecular-scale engineering, and substrate versatility. This review is motivated by recent advances in CVD methodology that leverage such **field effects** – both contact-based (plasma and photo-irradiation) and non-contact (electric and magnetic fields)—to exert additional control at the microscale. These approaches help transcend the restrictions imposed by



This journal is © The Royal Society of Chemistry 20xx

View Article Online
DOI: 10.1039/D5TA01981K

Open Access Article. Published on 15 2025. Downloaded on 2025/6/3 7:37:30.
This article is licensed under a Creative Commons Attribution 3.0 Unported Licence.

Journal of Materials Chemistry A Accepted Manuscript

macroscopic parameters on growth rate, composition, phase, morphology, and microstructure.

This account highlights the key achievements made in field-assisted CVD, emphasizing how these techniques enable the fabrication of thin films with enhanced material properties. The review is organized into focused subsections; each begins with an introduction to the field-matter interaction during CVD, followed by a discussion of field as an external parameter to control the CVD process, either independently or in combination with conventional parameters. Each section is concluded by outlining the influence of fields on precursor decomposition, nucleation, film growth, and resulting characteristics.

## 2. Plasma-assisted/enhanced chemical vapor deposition

### 2.1 Plasma-matter interaction during chemical vapor deposition

The PECVD process primarily utilizes the high energy electrons present in the non-equilibrium plasma of partially ionized gases (reactive and/or carrier), having electron temperature $T_e \leq 10$ eV (1 eV = 11600 K) and gas temperatures ranging from room temperature to $10^4$ K, to excite atomic and molecular precursor species to higher electronic and vibrational states.[32] This initiates or/and promotes the dissociation of chemical bonds, consequently facilitating thin film deposition at significantly lower temperatures compared to conventional thermal CVD processes. Plasma electrons, owing to their low mass and high mobility, lead in receiving energy from the ionization source (electric field, heat, light, magnetic field, etc.) and transmit it to other species via inelastic collisions, leading to numerous gas-phase plasma-chemical processes, such as ionization/recombination, excitation/relaxation, dissociation/association, and charge-transfer reactions.[33] The electron energy distribution function (EEDF; f(ε)), denoting the probability density for an electron to possess energy ε and described by Eq. (1)

$$f(\varepsilon) = 2\sqrt{\varepsilon/\pi(kT_e)^3}\exp\left(-\varepsilon/kT_e\right) \quad (1)$$

where k is Boltzmann constant and $T_e$ is the electron temperature, which becomes key in determining the rate of these processes. The EEDF indicates how electrons acquire energy from electric field and lose it in collision with the background gas. In low-density plasma, electrons have a Druyvesteyn energy distribution, whereas in high-density plasma they have a Maxwellian energy distribution.[34] The f(ε) depends on gas composition and electric field frequency used to generate plasma. Nevertheless, the ions, radicals, excited atoms/molecules, and photons present in the complex mixture resulting from plasma-materials interaction also play an important role in the efficiency of a PECVD process.[35,36]

During the PECVD process, the quasi-neutrality of plasma bulk breaks due to the buildup of charge near the substrate surface, and an electrically non-neutral region known as the plasma sheath is formed. The sheath thickness, which is of the orders of Debye length, depends on electron energy and electron density. As the potential attained by the substrate (floating potential) is less than plasma potential ($V_P$), positive ions diffuse through the plasma sheath, acquiring some additional energy en route to the substrate surface, which can be regulated by substrate biasing ($V_B$) leading to maximum kinetic energy given by Eq. (2)

$$E_{i,\,max} = e|V_P - V_B| + (\Delta E/2) \quad (2)$$

where term $(\Delta E/2)$ corresponds to periodic modulation (excitation frequency) of sheath voltage. The optimization of plasma-assisted modulation of CVD encompasses the identification of discharge characteristics suitable for the generation of high densities of free radicals and ions diffusing toward the surface and leading to deposition. To this, external parameters (pressure, gas composition and flow, discharge excitation frequency, and power) are administered to modulate the resulting plasma characteristics (plasma density, electron temperature, EEDF, electrical potentials, fluxes of species). In practice, ion energy ($E_i$) and ion flux ($\Phi_i$), key parameters affecting the film characteristics, are governed by the prevailing excitation frequency (radio frequency, RF or microwave, MW), pulsed direct current (DC), or RF-induced negative substrate bias.[35,37] Accordingly, based upon the power frequencies for plasma generation, the PECVD is often sub-classified as microwave PECVD (0.5–10 GHz), radio frequency PECVD (1–500 MHz), and direct current PECVD.[38] Additionally, depending upon the mode of plasma confinement using electrical, magnetic, or both, affecting the plasma density, the PECVD is further sub-classified as capacitively/inductively coupled PECVD,[39,40] helicon wave PECVD,[41,42] electron cyclotron resonance PECVD,[43,44] and so on.[45]

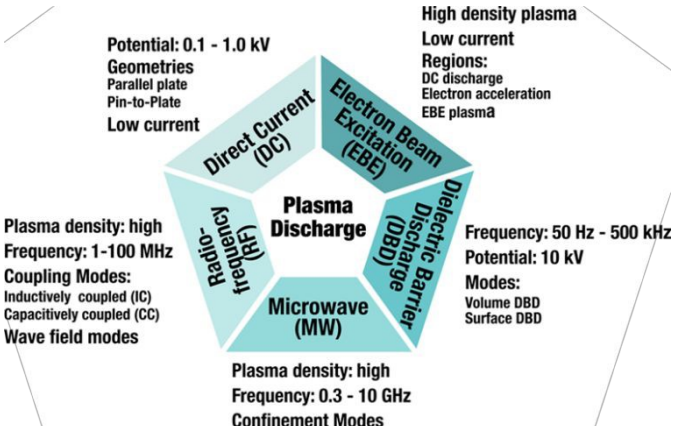


*Fig. 2. A brief overview of different plasma systems used in PECVD.*[46,60]

Santhosh et al.[46] presented an interesting overview of different modes of generation and confinement in plasma systems used in PECVD (Fig. 2). The PECVD process relies on a complex interplay of plasma characteristics, precursor chemistry, and reactor design.[47,48] Notwithstanding, high precursor decomposition efficiency, even at room temperature, is ensured by the energy transfers in the form of kinetic and



Please do not adjust margins

View Article Online
DOI: 10.1039/D5TA01091K

potential energies through plasma electrons and charged particles to the precursors, leading to the formation of free radicals and charged ions that are critical in influencing the deposition and growth.[49,50] Additionally, the plasma-surface interaction under appropriate plasma conditions, apart from initiating/promoting precursor decomposition, also promotes adsorption, desorption, nucleation, adatom migration, implantation, sputtering and displacement of atoms, thus tuning the composition, phase, microstructure, and morphology of the deposited material.[37,51,52]

### 2.2 Overview of plasma-enhanced chemical vapor deposition

The plasma-assisted modulations in CVD induce gas-phase chemistry mediated by energetic plasma species, enabling the decomposition of precursors, even of low reactivity, leading to the deposition on temperature-sensitive and morphologically intricate substrates.[53,54] A recent review by Snyders et al.[47] provides an impressive historical background of stages of development and conceptual foundations of PECVD, tracing the origin of PECVD to 1911. Several other reviews discussing the basic chemical and physical phenomena associated with the PECVD process have been reported.[17,46,47,49,55–60]

The PECVD process has been successfully used for depositing metals and ceramics,[49,61–66] carbon-based materials,[57,58,67–71] and organic polymers[17,47,72]. In recent years, plasma-assisted modulations have focused on enhancing deposition and growth rates,[73] achieving directional growth and crystallographic orientation of nanostructures,[58,74–76] surface modification,[77–80] doping and vacancy generation,[81–85] and manipulating phase composition and crystallinity[86–89]. **Table 1** presents selected recent reports on PECVD, displaying its utility in thin film fabrication for a range of materials.

**Table 1.** Some recent reports on plasma-enhanced CVD of functional materials.

| Material/ substrate | Plasma-type | Key Features | Application | Ref. |
|---|---|---|---|---|
| ***Carbon-based materials*** | | | | |
| Diamond films on 3D Si spheres | MW, ($CH_4$, $H_2$), 10 kPa | Uniform EF and plasma distribution by Faraday cage | Uniform diamond coating on complex 3D geometries | 73 |
| Diamond films/ Si | MW, 600-900 W, ($H_2$, Ar, $CH_4$), 12.6 kPa, 750 °C | Bias-enhanced nucleation led azimuthal texturing; Raman peak ~1332 $cm^{-1}$ | Quantum devices; coatings with aligned N vacancy defect centres, ~70% azimuthal orientation | 90 |
| DLC/ tungsten carbide | Cathode arc discharge (120 A DC), ($N_2$, Ar, $C_2H_2$), 0.9 Pa, 450 °C | Role of particle energy on structure and properties | Cutting tool protection film; coefficient of friction=0.112 | 91 |
| (n-diamond)-carbon nanowalls hybrid/ Si (100) | CCP-RF, 300W, (CO, $CH_4$, Ar, $H_2$), ~33 Pa, 450 °C | Large area (4 inch) simultaneous deposition | - | 92 |
| Fluorescent nanodiamond with Si impurity/ Si | MW, ($H_2$, $CH_4$), 2.5 kPa, 700 °C | A vertically aligned Si source in plasma path gives highly fluorescent (7-10 times enhanced) diamond film | Photoluminescent films | 85 |
| Vertical graphene (VG)/ quartz | RF, 500 W, ($C_2H_2$, $H_2$), ~1x$10^5$ Pa, 900 °C | Position-induced control over morphology; superhydrophobicity and ultrahigh emissivity (0.999) | Black body and infrared thermometer | 93 |
| Graphene/ sapphire | ECR, 500 W, ($C_2H_2$, $H_2$), ~0.54-5.4 kPa, 600-700 °C | Direct growth of uniform and continuous graphene on insulators at reduced temperature | Graphene film for optoelectronic device; transmittance > 90%, sheet resistance < 1 kΩ) | 94 |
| Vertical graphene/ $SiO_2$ | RF (Remote), 300W, ($CH_4$, Ar), 0.1 Pa, 300–1000 °C | Interfacial EF between plasma and substrate-governed vertical growth | - | 95 |
| ***Metalloids*** | | | | |
| $SiN_x$/SiOF/$SiN_x$ flexible moisture barrier film/ Polymer substrate | MW, 1500 W, (Ar, $SiF_4$, $N_2O$), 9 Pa, 45 °C | Films with high WVTR ($3.94\times10^{-4}$ g $m^{-2}$ $day^{-1}$) and visible light transmittance (93.32%) | Roll-to-roll processing of optical devices | 96 |
| Amorphous hydrogenated silicon carbonitride/ Si | MW (Remote), 120 W, (TMDS/HMDS, $H_2$, $N_2$), 43–90 Pa, 30–400 °C | Precursor with Si-H bonds are necessary for initiation of remote plasma-CVD with single-source | Tribological coatings | 97 |
| Si film on different substrates | CCP-RF, 15 W, ($SiF_4$, $H_2$, Ar), 306 Pa, 150 °C | Area-selective Si deposition; surface-dependent nucleation delay due to fluorinated Si precursor | - | 98 |
| Hydrogenated silicene/ polycrystalline Ag | - | First report of silicone synthesis by PECVD | - | 99 |
| Phosphorus-doped nanocrystalline $SiO_x$/ glass | RF (13.56, 27, 40 MHz), (318, 333, 256 W), ($SiH_4$, $H_2$/$CO_2$/$PH_3$), 200 °C | Industrial-scale deposition using a very high-frequency PECVD system | Si heterojunction solar cells | 100 |
| 2D hexagonal-boron nitride (h-BN)/ $SiO_2$/Si | RF, 30 W ($BH_3$-$NH_3$, Ar/$H_2$), ~115 kPa, 300 °C | First report of catalyst-free directly-on-substrate growth | Dielectric interface for $WSe_2$ field-effect transistor | 101 |
| Multilayered h-BN/ Si, $SiO_2$/Si, and quartz | ICP-RF, 40-180 W, (Borazine, Ar, $N_2$, $H_2$) 10-100 Pa, 300-900 °C | Catalyst-free low-temperature growth of multilayered (>50 nm) h-BN | Optoelectronics; comparable/better optical characteristics than commercial h-BN, $E_g$=5.8 eV | 40 |
| h-BN/ Si | MW, 1000W, ($H_2$, $NH_3$, $B_2H_6$), 2 kPa | Regardless of $B_2H_6$ flow rate (0.6–3.0 sccm), h-BN with B/N ratio=1 are formed | High-hardness coatings | 102 |

Open Access Article. Published on 15 2025. Downloaded on 2025/6/3 7:37:30.
This article is licensed under a Creative Commons Attribution 3.0 Unported Licence.

Journal of Materials Chemistry A Accepted Manuscript



This journal is © The Royal Society of Chemistry 20xx

Please do not adjust margins

View Article Online
DOI: 10.1039/D5TA01081K

| | | | | |
|---|---|---|---|---|
| 2D Boron carbonitride ($BC_xN$)/ $SiO_2$/Si or $SiO_2$ | 30W, ($BH_3.NH_3$, $CH_4$, Ar, $H_2$), 80 Pa, 450-620 °C | First report of catalyst-free temperature-dependent $BC_xN$ growth; $E_g$=2.3 eV | Field effect transistors and sensor; $H_2O_2$ detection limit= 0.1 μM | 103 |
| Boron film on (100) Si | RF, 1000W, (Ar, $B_2H_6$ ), 133-239 Pa | Comparison of PECVD films with other related deposition techniques | Mask layer/ structural material in micro-machining | 104 |
| ***Metals, oxides, chalcogenides, nitrides*** | | | | |
| Fe, Co, and Ni metallic films on different substrates | DC hallow cathode, 50-150 W, 50 Pa, 70-100 °C | Plasma electrons as reducing agents; electrical conductivity of substrate plays a major role | Catalysts and electronic devices | 105 |
| $Cu_2O$ on different substrates | CCP-RF, 10 W, (Ar), 26 Pa, 200 °C | Large area (2.88×3.13 m²) uniform deposition | Thin-film semiconductors; $\rho=10^5$ Ω cm; $E_g$=2.53-2.59 eV $\mu_H=1.48$ cm²(V s)$^{-1}$ | 106 |
| $MoS_2$/ sapphire or $SiO_2$/Si | RF direct/remote plasma, 300 W, ($MoO_3$, $H_2S$, Ar), 400 °C | Photoluminescence (direct plasma deposited only at 2.0 eV; remote plasma dep. at 1.8 and 2.0 eV) | Hydrogen evolution reaction (HER) | 107 |
| N-alloyed $Ga_2O_3$ films ($Ga_2O_3$, GaON, and GaN)/ *c*-$Al_2O_3$ | RF, 200 W, (Ga, Ar, $N_2$, $O_2$), 850 °C | Bandgap tuning and O vacancy density ($V_o$) reduction by adjusting $N_2$:$O_2$ gas ratio | Photodetectors; $E_g$=4.64-3.25 eV, $V_o$= 32.89-19.87% | 108 |
| $MoS_2$ | ICP-RF, 300 W, ($S_8$, Ar), 29-53 Pa, 500 °C | Single-step deposition using elemental S and $MoCl_5$ as precursors | - | 109 |
| $Mo_2C/MoS_2$ or $Mo_2C/MoSe_2$ on Cu foil | RF, 150 W, (S/Se, $H_2$, $N_2$), 750-350 °C | Phase-engineering of $Mo_2C$ by plasma-assisted selenization and sulfurization | HER; (Tafel slope/mV dec$^{-1}$: $Mo_2C/MoS_2$=83, $Mo_2C/MoSe_2$= 66); (Overpotential/mV: $Mo_2C/MoS_2$=2263, $Mo_2C/MoSe_2$=257) | 110 |
| Amorphous carbon–tin film/ glass | Glow discharge (40 kHz), 500 W, 4.2 Pa | Coupling capacitance of reactor controls the semiconductor/ insulator characteristics | HER or $CO_2$ reduction; Transport gap= 5.2 eV, $E_g$=3.1 eV, electron affinity= 2.1 eV, ionization potential=7.3 eV | 111 |
| Cr-N coating on Cr layer | MW, 5000 W, ($H_2$ and $N_2$), ~22.6 kPa, 750-950 °C | MW plasma-assisted in-situ reactions on a chromium pre-coated substrate | Tribological coatings; coefficient of friction <0.55 (in 750-950 °C range), wear resistance=0.085 and resistance to plastic deformation=0.142 at 800 °C | 112 |
| GaS on different substrate | RF (40.68 MHz) discharge, 50 W, 13.3 Pa, 250 °C | Influence of substrate on stoichiometry, structure, and surface morphology investigated | - | 113 |
| TiN, TiBN or $TiB_2$ hard coating/ steel | Pulsed DC, ($BBr_3$, $TiCl_4$, $N_2$, $H_2$, Ar), ~933-1200 Pa, 500 °C | Use of $BBr_3$ as B precursor; hardness of TiN, TiBN and $TiB_2$ films was 15.74, 19.44 and 23.47 GPa, respectively | Tribological coatings; for $TiB_2$ coating, elastic modulus=298 GPa and coefficient of friction =0.23 | 75 |
| GeSn film on Si | RF, 30 W, ($GeCl_4$, $SnCl_4$, $H_2$), 53 Pa, 180 °C | Low-temperature GeSn film without any buffer layer or post-annealing (growth rate ≈15 nm/min at 180 °C) | Short-wave infrared Si photonics; high Sn (>9%) and low threading dislocation density (1×10$^7$ cm$^{-2}$) | 114 |
| ***Others*** | | | | |
| Methyl ammonium iodide (MAI) | RF, 60 W, (MAI, $H_2O$, Ar), ~13 Pa | First report of MAI deposition using PECVD for $MAPbI_3$ films; $E_g$=1.57 eV, Refractive index=3.07, extinction coefficient=0.13 | perovskite/Si photodiode; rectifying ratio= 1.58×10$^4$ at 1.0 V, photo-sensitivity= 7.46×10$^2$ | 115 |
| Poly(DPAEMA) film | RF, 20-80 W, (Diisopropyl aminoethyl methacrylate, $N_2$), ~13--67 Pa, 10-40 °C | Initiator-free polymerization; large area (>16 cm diameter) deposition rate =18.6 nm/min at 40 °C | pH-responsive polymers | 116 |

*CCP– Capacitively coupled plasma; ICP– Inductively coupled plasma; DLC– Diamond-like carbon; DPAEMA– 2-Diisopropyl aminoethyl methacrylate; $E_g$– Optical band gap; h-BN– hexagonal boron nitride; HMDS– hexamethyldisilazane; n-diamond– new-diamond (Face centered cubic-carbon); TMDS– 1,1,3,3-tetramethyldisilazane; WVTR– water vapor transmission rate; ρ– resistivity; $\mu_H$=hall mobility;*

In PECVD, the excitation frequency of plasma source provides a key tool to modulate the deposition process.[100,117–122] Generally, an RF plasma source uses industrial 13.56 MHz frequency for plasma excitation, and for increasing the plasma density to accelerate the precursor decomposition and subsequent film growth rate, the plasma power is increased. However, an increase in power also causes increased ion bombardment, which often proves detrimental to the film quality. To overcome this, very high frequency (VHF; 30–300 MHz)[123–125] or dual frequency[126–129] plasma configurations are employed. With VHF plasma, increased frequency imparts higher energy to electrons via so-called stochastic heating but reduces the sheath thickness and lowers the electrical field intensity, thereby reducing the ion-bombardment energy.[120] A dual frequency configuration involves two different frequencies on the same electrode or on separate electrodes, where high frequency imparts a stable discharge generating the reactive species and the low frequency controls the ion bombardment.[119] The dual frequency configuration has proven its utility in improving the deposition quality in terms of film stress, step coverage, and stability.[129]

In catalyst-mediated PECVD processes, plasma-catalyst interactions play a key role during the pretreatment step and deposition. Such plasma-assisted restructuring or activation has proven to be important for controlling mechanism, growth rate, composition, morphology, and microstructure.[130–135]

Open Access Article. Published on 15 2025. Downloaded on 2025/6/3 7:37:30.
This article is licensed under a Creative Commons Attribution 3.0 Unported Licence.

Journal of Materials Chemistry A Accepted Manuscript



Please do not adjust margins

View Article Online
DOI: 10.1039/D5TA01081K

Open Access Article. Published on 15 2025. Downloaded on 2025/6/3 7:37:30.
This article is licensed under a Creative Commons Attribution 3.0 Unported Licence.

Journal of Materials Chemistry A Accepted Manuscript

Restructuring of metal catalysts used for the growth of carbon nanostructures,[130–134] silicon nanowires[135–139] and other metal/metal oxide nanowires[140,141] by plasma pre-treatment or/and during plasma-assisted catalytic vapor-liquid-solid[142,143] and solid-liquid-solid[141,144] growth mechanisms are well documented. For example, Zheng et al.[141] demonstrated that during GeSn nanowires growth using Sn nanoparticle catalysts $H_2$ plasma-assisted annealing inhibited the wetting of Sn during and at the end of nanowires growth, preventing the pinning of Sn NPs around the nanowires. Similarly, during in situ fabrication of graphitic nanosheet supported N-doped carbon-coated $LiFePO_4$ (LFP@NC/GNS), plasma assisted the reduction of $Fe^{2+}$ ions to $Fe^0$, which catalyzed in situ formation of graphitic nanosheets on LFP@NC, and simultaneously removed $Fe^{\bullet}_{Li}$ antisites, a commonly observed detrimental defect in LFP for its performance in Li-ion batteries.[134]

Over the years, there has been a growing trend to integrate PECVD with other deposition techniques for the deposition of a diverse range of materials. In PECVD of rare-earth element-doped Si-based materials, metal-organic precursors are used for in situ metal doping. However, the use of metal-organics causes significant hydrogen contamination. To overcome this limitation, a hybrid deposition technique was developed by in situ coupling PECVD with a magnetron sputtering source having the rare-earth target.[145–150] Kulczyk-Malecka et al.[150] proposed a high-power impulse magnetron sputtering-PECVD system where the magnetron-generated plasma also acted as an electron source to drive the precursor decomposition in the PECVD process, thus requiring only a single power supply. Moreover, the application of a variable magnetic field strength magnetron resulted in a precise control over dopant content without adjusting the power supply. Lee et al.[151] used a similar PECVD-sputtering hybrid system to fabricate Ti-doped diamond-like carbon (DLC) coatings, where metal doping helped overcome the residual stress in the deposits. Moreover, a multi-step PECVD or its integration with other deposition techniques resulted in specific nanostructured assembly.[152–156] For example, Huang et al.[153] reported an anode-assisted reactive magnetron sputtering coupled with a DC PECVD system to fabricate amorphous hydrogenated DLC coatings with CrC interlayers, ameliorating the adhesion properties of DLC coatings by reducing the residual stress. Dias et al.[157] reported large-volume deposition (~19 mg $min^{-1}$) of metal oxide/sulfide anchored N-graphene for supercapacitor applications by spraying a controlled metal-oxide(sulfide) microparticles jet into the plasma afterglow region, leading to plasma-induced size reduction and subsequent binding to the N-graphene sheets. Furthermore, Su et al.[158] reported an integrated process encompassing plasma-assisted roll-to-roll deposition of vertical graphene (VG, which are graphene-containing carbon nanosheets grown vertically onto the substrate) and simultaneous syngas production from greenhouse gas mixtures. Such hybrid approaches have effectively expanded the application spectrum of PECVD, overcoming the technological barriers of limited precursor availability.

Over the years, manipulation of plasma characteristics and plasma delivery have envisaged the CVD process for tailoring film properties for desired applications. In this regard, PECVD using pulsed plasma flow with dynamic pulse parameters such as pulse frequency, duty ratio, and peak power has displayed remarkable effects on the deposition qualities.[159,50,160–164] Pulse modulation, in combination with other plasma parameters, has been successful in significantly decreasing deposition temperature while maintaining or even enhancing characteristics like growth rate and composition.[159,165,166] Interestingly, significant film growth also occurred during the ''off'' plasma duration[167] and the pulsed mode resulted in additional morphological variations.[168,169] For example, during PECVD growth of 2D copper sulphide superstructures, Taplick et al.[169] observed that site-dependent charging–discharging dynamics during plasma pulsing played a crucial role in the directed assembly of nanoplatelets in the gas phase. The plasma pulsing promoted side-by-side growth, whereas continuous plasma additionally caused pronounced spike-like growth perpendicular to the basal plane. Similarly, pulsed PECVD displayed great usefulness in PECVD of insulating thin films, where substrates are needed to be under alternating signal.[170] In this regard, it is worthwhile to mention the hybrid plasma-immersion ion implantation and deposition systems for DLC coatings from hydrocarbon precursors, where ion-implantation renders improved tribological and mechanical properties.[171–173] Recently, Tran et al.[160] used similar hybrid system to fabricate high surface area activated carbon coatings for biomedical applications, where the growing coatings were subjected to implantation of ion-aggregates formed in the plasma in a high voltage dielectric barrier discharge PECVD.

Moreover, efforts have been made to further modulate pulsed PECVD by coupling it with externally-controlled MF for plasma confinement.[162,163,174] To fabricate pinhole-free amorphous silicon carbo-nitride, SiCN, at a high deposition rate, e.g., Matsutani and coworkers[162] designed MF coupled pulsed PECVD system, where a permanent magnet kept below the plasma electrode (which also holds the substrate) in a parallel electrode setup led to increase in plasma current and deposition rate, as compared to that without MF. In a subsequent study, they generated pulsed plasma alternatively on both electrodes, while keeping the permanent magnet below the substrate electrode, to overcome the etching-induced film thinning due to the charging effect.[163] The MF confinement of plasma during the plasma-immersion ion implantation and deposition of DLC coating resulted in improved diamond-like character with defect-free morphology and reduced roughness in as-grown films.[174]

Plasma-assisted processes have been demonstrated for large-scale fabrication of various carbon nanostructures for electronics, optoelectronics, energy and environment, applications.[58,67,175–179] In addition, the PECVD processing has enabled the controllable preparation strategy for the growth of desirable carbon nanoarchitectures at significantly lower temperatures[112] and even without the need of catalysts,[180] ensuring high purity by eliminating metal contamination. The catalyst-free growth of VG,[181] where high-energy ion bombardment activated the surface for nucleation by inducing defects and facilitated growth mainly from the surface of

 This journal is © The Royal Society of Chemistry 20xx

Please do not adjust margins

DOI: 10.1039/D5TA01081H



substrate.[176,180] PECVD has enabled substrate-independent growth of graphene, facilitating its growth at 700 °C on Si and 3C-SiC/Si surfaces, important in electronics/optoelectronics heterojunction devices, which could not be achieved by thermal CVD due to extremely low diffusion of carbon over these surfaces, as indicated by the theoretical studies.[182] For deposition of amorphous carbon/DLC films, the control over plasma-ion energy by adjusting the bias power and bias voltage has conferred control over the H-content and $I_D/I_G$ and $sp^2/sp^3$ ratios, regulating their amorphous or DLC characteristics and resulting mechanical, electrical, optical, or tribological properties. For example, high ion density plasma, such as microwave plasma and magnetically enhanced plasma, promoted low H-content whereas low-density RF plasma promoted high H-content growth.[68,69] A high ion density helped the removal of H atoms from C-H bonds and raised the $sp^2/sp^3$ ratio in the deposited films.[69]

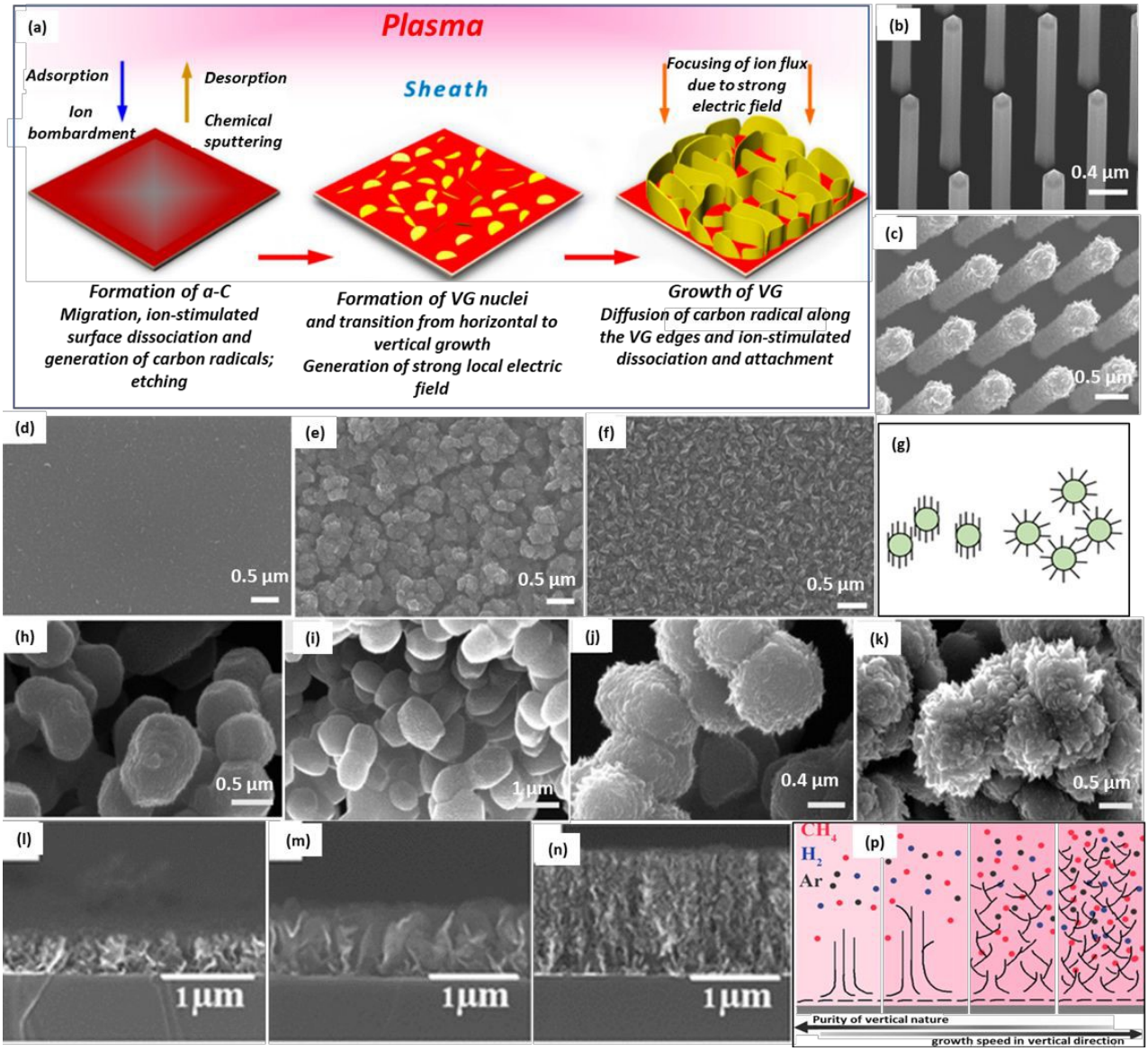


*Fig. 3. Schematic diagram of plasma-assisted vertical growth of carbon nanostructures (a), Adopted with permission from MDPI;[46] Scanning electron microscopy (SEM) images of GaN nanowires (b) before and (c) after the VG growth in remote PECVD; SEM images of growth on $SiO_2$/Si substrate surface, nearly complete growth inhibition VG growth when EF is completely screened (d), growth along the mesh holes when EF is partly blocked (e), normal VG growth without screening (f); Schematic illustration of possible growth modes of VG on nanoparticles- (left) perpendicular to the substrate and (right) alongside the normal directions of the nanoparticles (g); SEM images confirming that the latter growth mode with increasing flow rates of $C_2H_2$ and growth times (h)-(k), Reused with permission from American Chemical Society (ACS).[186] SEM images of VG deposited at 600 °C with different plasma powers, 100 (l), 200 (m), and 300 (n); and schematic showing difference in growth behavior of VG under different plasma densities (p), Reused with permission from ACS.[95]*

Open Access Article. Published on 15 2025. Downloaded on 2025/6/3 7:37:30.
This article is licensed under a Creative Commons Attribution 3.0 Unported Licence.

Journal of Materials Chemistry A Accepted Manuscript



Please do not adjust margins

View Article Online
DOI: 10.1039/D5TA01081K

An important aspect of catalyst-aided or catalyst-free PECVD of various carbon nanomaterials is its ability to aid in vertically aligned growth, as the electric field associated with the plasma sheath helps the nanofibers grow vertically from the substrate.[58,95,183–185] Various studies demonstrate, however, that the mechanistic implications of the role of plasma and other process parameters on the vertical growth mechanism are not well understood.[95,186,187] Theoretical studies suggest that during VG growth, the Coulombic repulsion due to the accumulated electrons on the flakes eventually push the growth to change from 2D to 3D mode.[186] Sun et al.[186] studied the role of plasma sheath EF in the mechanism for the growth of vertically grown graphene nanostructures. Using GaN nanowires grown onto silicon substrate (GaN/Si) (Fig. 3(a)), much denser and longer growth of VG flakes was observed at the nanowire tips than on the nanowire bodies (Fig. 3(b)), indicating a local field-enhancement effect due to the higher field strengths and charge accumulation at the wire tips (Fig. 3(c)). Furthermore, when EF is selectively screened by employing metal meshes of different sizes, growth occurred only along the holes (Fig. 3(d)-(f)), due to partial blocking of electric field formed in the plasma sheath. Moreover, using $SiO_2$ nanoparticles as substrate, out of two possible modes of growth (Fig. 3(g)), the VG exclusively grew perpendicular to the particles' surface (Fig. 3(h)-(k)).[186] These findings set the foundations for further mechanistic studies on the vertical growth of 2D materials.

Zhang and coworkers[188–191] demonstrated the use of auxiliary vapors (chloroform, fluorobenzene, water, etc.) along with the chemical precursor to generate a special collection of plasma and reactive species to enhance the growth rate of VG in an electric field-assisted PECVD. For example, the introduction of fluorobenzene and water in the deposition chamber promoted the decomposition of carbon source and etching of amorphous carbon, respectively, to enable higher growth rates (~14.4 μm $h^{-1}$).[189] Zhang et al.[95] observed that milder plasma and temperature conditions are helpful for vertical growth, as the higher growth temperatures, precursor and carrier flow rates, as well as applied plasma power also promoted branching (Fig. 3(p)), apart from increasing the growth rate (Fig. 3(i)-(n)).

In vacuum or atmospheric PECVD, plasma-assisted effects have demonstrated synergistic regulation of nanostructure and defect engineering in carbon nanostructures.[46,93,192–197] For example, Ma et al.[93] demonstrated a continuous variation of morphology, from "porous" to "tree-like" and then to "wall-like" structure, by adjusting the growth positions during PECVD of VG. Similarly, Dias et al.[198] reported a PECVD approach capable of varying the density and energy of basic building blocks within the high energy-density plasma environment in the assembly zone, allowing precise control over the energy and material fluxes directed towards the evolving nanostructures for sustained gram-scale (30 mg/min) production of graphene and allied derivatives from a low-cost feedstock of ethanol and acetonitrile. Moreover, plasma-assisted vertically-aligned growth is not limited to carbon-based nanostructures and it has been successfully used in the growth of vertically aligned metal oxides, nitrides, and chalcogenides[168,199–206] as well as polymeric and heterostructures[207,208].

Plasma-assisted CVD of functional inorganic materials with specific composition, phase, morphology and microstructure have led to promising applications in integrated electronics, energy storage and conversion, catalysis, and sensors.[106,168,209–211] Among chalcogenides, transition metal dichalcogenides (TMDs) present unique properties depending on their polymorphic phases, such as 1T (metallic), 1T' (semimetal-like), and 2H (semiconductor).[212] In recent years, the fabrication of phase-pure and polymorphic heterostructure of these compounds has been realized by temperature-controlled plasma-assisted sulfurization/selenization of metal.[84,89,110,200,210,213–218] Kim et al.[201,210] reported an optimized PECVD system with Ar+$H_2S$ plasma for 1T-$WS_2$ and 1T-$MoS_2$ synthesis, which is otherwise challenging due to their metastable nature. The pre-deposited metal was sulfurized by accelerating the $H_2S^+$, ionized through the penning effect, in the plasma (positive) to the substrate (relatively negative) by the electric field in the sheath region. The ion bombardment caused the metal layer to break into nanocrystals and the $H_2S^+$ simultaneously penetrated it for efficient sulfurization. Unlike the microcrystalline nature of the deposits obtained from other chemical methods, the nanocrystalline structure of 1T-TMDs obtained from PECVD transformed it from metastable to a highly stable 1T phase structure with a lower surface energy than the 2H phase. However, in plasma-assisted sulfurization/selenization at higher temperatures, 2H phase is predominantly formed.[89,219]

PECVD has been proven to be a convenient method for the fabrication of few-layer TMD-TMD heterostructure interfaces that exhibit interesting properties for diverse applications, due to their uniform band edges and tunable band gap through numerous layers.[200,220] Kim et al.[221] executed Ar plasma-induced phase transformation of $SnS_2$ to SnS for the fabrication of vertical SnS-$SnS_2$ p-n junction heterostructure. The bombardment of $Ar^+$ radicals on $SnS_2$ surface to preferentially cleave Sn-S bonds leading to selective etching of more volatile sulfur, thereby inducing the formation of SnS phase. Similarly, Li et al.[222] reported fabrication of vertical SnSe/$SnSe_2$ p–n heterojunction by $NH_3$ plasma-induced phase transformation. Seok et al.[200] reported wafer-scale $MoS_2$–$WS_2$ vertical heterostructures via a single-step plasma sulfurization of sequentially deposited seed layers of W and Mo (1 nm each) onto the $SiO_2$/Si substrate. By optimizing plasma and deposition temperature, Seok et al.[220] reported wafer-scale growth of phase-selective 1T-$MoS_2$/1T-$WS_2$ or 2H-$MoS_2$/2H-$WS_2$ vertical heterostructures. Likewise, Sino et al.[213] demonstrated a similar top-down approach for high-yield MoSSe asymmetric structures from $MoS_2$ flakes where plasma-assisted selenization resulted in a Janus MoSSe layered structure at low temperature (200 °C) and a polymorphic alloy MoSSe at high temperatures (400-600 °C). Moreover, plasma-assisted sulfurization/selenization has also been extended for the fabrication of heterostructures of TMDs with metal oxides and carbides.[110,218,223,224]

Open Access Article. Published on 15 2025. Downloaded on 2025/6/3 7:37:30.
This article is licensed under a Creative Commons Attribution 3.0 Unported Licence.

Journal of Materials Chemistry A Accepted Manuscript



This journal is © The Royal Society of Chemistry 20xx

Please do not adjust margins

View Article Online DOI: 10.1039/D5TA01082H

For the fabrication of photovoltaic devices, PECVD is extensively employed in the deposition of antireflection coatings, passivation layers, dielectric layers, and so on.[59,225–228] To ensure high throughput, avoiding the standing wave effect in large-area uniform deposition process, it is essential to control the spatial distribution of plasma parameters and the complex interplay of plasma physics and chemistry with the deposition-chamber dimensions. Accordingly, numerous theoretical and experimental studies have been performed to address the uniformity of plasma over a large area.[122,229] Zhang et al.[229] investigated plasma density distribution under different voltage and pressure conditions in $H_2$ capacitively coupled plasma (CCP) discharge sustained by multiple consecutive harmonics. Using a 2D fluid model, Kim et al.[230] analyzed the nature of substrate and reactor sidewall material on plasma density distribution in a CCP reactor. They also investigated the role of dilution gas on the spatial distribution of the plasma parameters in a CCP reactor.[231] Similarly, in deposition of hydrogenated nanocrystalline silicon oxide (nc-$SiO_x$:H), Yu et al.[100] designed industrial-scale VHF PECVD system with a minimized standing wave effect, by using a curved electrode and a glass plate over it, thus reducing the degree of non-uniformity for VHF1 (27 MHz) and VHF2 (40 MHz) to ±4.6% and ±10%, respectively, as against to ±27% and ±70%, for the same frequencies using flat electrode configuration and without glass plate. As a result, the thickness uniformity was improved in nc-$SiO_x$:H layers. When employed in a metric 6 mm screw thread (M6)-size bifacial silicon heterojunction solar cells with silver electrodes, high power conversion efficiency with a narrower distribution range (25.7–25.9%) under VHF1 was observed as compared to the VHF2 (25.3–25.9%). On replacing the Ag with Cu electrodes, the device displayed a power conversion efficiency of 26.41%. Besides enhancing the growth rate, dual-frequency PECVD operations have effectively improved film stress, chemical composition, step coverage, and stability.[37,126,232,233]

As plasma characteristics are highly dependent upon plasma sources or/and coupling mechanisms, some desirable effects for specific applications may be attained only by a particular plasma source.[32] For example, during the growth of carbon nanostructures using an RF plasma source, the ICP led to vertical graphene, whereas the CCP led to carbon nanotubes (CNT) due to the coupling mechanism affecting the plasma density.[234] From the standpoint of innovation in plasma processing and confinement for PECVD, magnetized plasma sources such as helicon wave plasma (HWP) and electron cyclotron resonance plasma, in which the excited electrons are launched as spiral beams along the MF lines as a function of the MF and excitation frequency, enables a resonant-like increase of plasma density useful in various applications.[235–239] The HWP source, with its electrodeless and magnetized plasma features, has provided important means to regulate the energetic ion-bombardment flux on stress level, structure, and resulting properties of the deposited films. Along with the flow rate, parameters–RF power and MF strength–can be used to regulate the high-density HWP.[240] Accordingly, HWP-CVD is employed for the deposition of carbonaceous,[42,239,241–243] metal carbide,[244,245] and metal oxide[246] coatings. During PECVD of DLC coatings, high plasma density of HWP enabled a high growth rate.[247,248] Qian et al.[249] reported room temperature PECVD of DLC in HWP with different magnetic field ($B_0$=1200-2400 G). The optical emission spectroscopy analyses indicated that the precursor decomposition followed the pathway ($CH_4+e^- \rightarrow CH_3+CH_2+CH+C+H$), along with the formation of $C_2$ species by the recombination of $CH_4$ and other C-containing radicals. An increased MF provided high plasma density for achieving a higher growth rate. The $C_2$ and CH emission intensities increased to a maximum value at $B_0$=2100 G, leading to enhanced deposition rate (800 nm/min) and $sp^3/sp^2$ ratio, as numerous energized H atoms generated by HWP helped the graphitic carbon removal and hydrogen incorporation.

Electron cyclotron resonance plasma source is another example where MF-assisted electron confinement plays key role in plasma density enhancement, influencing the PECVD growth rate.[236,238,250,251] For example, during epitaxial growth of silicon thin film, the MF variation shifted ECR plasma zone close to the $SiH_4$ outlet, causing increased concentration of free radicals responsible for deposition and resulting in increased growth rate.[236] Nevertheless, the MF-assisted plasma confinement for enhanced growth and/or microstructural evolution has not been limited to magnetized plasma sources alone, as demonstrated by Miller et al.[237] with a RF-powered hollow cathode PECVD system for DLC films. The MF applied via an electromagnetic coil around the hollow cathode tube influenced the magnitude of cathode DC self-bias, with an MF of ~95G inducing maximum DC self-bias, indicating an optimal gas ionization that was independent of the applied RF power. Similarly, in a CCP system, the application of an MF (typically order of ~$10^2$ G) parallel to the electrodes normally enhanced the performance of CCP, although stronger MF may cause plasma non-uniformity.[252] Moreover, combined plasma, magnetic and electric field (substrate bias voltage) modulation to control the number of electrons and their movement path, influencing the ability of electrons to collide and ionize the gas for the deposition of DLC films is reported.[91] Nevertheless, recently, some efforts focusing on plasma diagnostics and measurement of flux and energy of plasma and reactive species in magnetically confined plasma has been reported,[252–256] which could be valuable for a better understanding of plasma chemistry to design suitable deposition conditions for film growth and microstructure.

In recent years, the requirements of fast processing with minimal crystalline defects in many device fabrication processes with enhanced plasma density at controlled ion-bombardment has prompted to test a variety of plasma excitation and delivery methods, such as gas-jet electron beam plasma,[257–260] hallow-anode plasma,[45,261,262] and radical injection plasma[45,263–266]. There have been reports on the usage of highly ionized plasma, designed using continuous or pulsed high power schemes and often coupled with substrate bias to impart a high degree of energetic bombardment, influencing the deposition conditions and resultant phase, microstructure and quality.[267–270] High-power plasma conditions involving excited ions with high power densities and ion energy have been important in the 3D growth

Open Access Article. Published on 15 2025. Downloaded on 2025/6/3 7:37:30. This article is licensed under a Creative Commons Attribution 3.0 Unported Licence.

Journal of Materials Chemistry A Accepted Manuscript



Please do not adjust margins

View Article Online
DOI: 10.1039/D5TA01084K

of carbon nanostructures (thickness, branching, alignment height, etc.).[271] For example, the nucleation of carbon nanowalls in the initial growth period occurred only under optimal balance between ion and radical fluxes, with ion bombardment modifying the surface adsorption mechanism from physical to chemical.[266,272] It is important to mention here, however, that although it is generally accepted that high ion energies (~200–250 eV) and ion fluxes (~3.3–3.8 μA $cm^{-2}$) are necessary to induce the nanowalls deposition, there are many reports of PECVD growth of nanowalls in low-energy ions, following a different growth mechanism.[58,273,274]

Plasma-enhanced chemical vapor deposition is also extended to the deposition of organic polymer films as an initiated-PECVD (i-PECVD) process where usually a plasma of low power density is used for quasi-selective breaking of weak peroxide bond (O–O) in the initiator molecules, facilitating subsequent polymerization of monomers.[275–280] Alternatively, i-PECVD is also performed directly with monomers only, without using any initiator.[281,282] However, limiting the purview of this review, the reader is referred to the existing literature[283,284] for detailed information. Similarly, as an alternative to plasma-assisted precursor decomposition, localized substrate-heating by high-energy (often in keV range) focused ion or electron beam is used, enabling nanoscale-level control over the material fabrication in CVD. For detailed information about such focused ion/electron beam-assisted CVD, relevant references[285–290] can be referred to. Here, the recent reports of plasma electron-assisted CVD of metallic films[105,291–293] are noticeable, which rely upon electron-induced redox chemistry, unlike the thermal effects in focused ion/electron beam-assisted CVD.

### 2.3 Perspective on plasma-enhanced chemical vapor deposition

Modulations based on nonconventional energy vectors (plasma and photons) and fields (electric field and magnetic field) have significantly enriched the landscape of CVD, enabling the facile deposition of unique nanoarchitectures with desired properties at significantly low temperatures and faster rates compared to the conventional thermal CVD. The use of auxiliary gases along with the key precursor to generate a special collection of plasma and reactive species in the reactor has constantly been popular, enabling lowered deposition temperature and/or increased deposition rate [74,189,190,294]. The future opportunities lie in designing novel configurations of plasma power, precursor and reactor design, controlling the plasma parameters (energy density and the composition and density of species such as photons, ions, excited fragments, etc.) for better control over the kinetics and imparting added functionalities (vacancies, dopants, etc.) in the deposited materials. With a judicious selection of plasma chemistry and substrate attributes, for example, PECVD can perform area selective deposition.[98,293,295–298] The PECVD has been more interested in utilizing the energy of plasma electrons, often ignoring the role of ionic species, which can be partially due to the emergence of related technology of plasma-immersion ion implantation and deposition. Increased attention towards tuning the plasma ionic species can provide an additional degree of freedom for influencing the properties of the thin films grown by PECVD.[37,299,300]

Given the fact that the plasma-assisted processes are quite complex and involve numerous physical and chemical processes, the study of deposition and growth mechanism has always been challenging. Additionally, most of the reported data on PECVD are largely based on in-house plasma source and reactor, making the comparison of data somewhat challenging. Therefore, generalized relations between film characteristics and growth parameters such as temperature, dosage of precursors and carrier gases, and plasma power are still less established to date, hindering its utility in large-scale production of advanced materials and devices for specific applications. To overcome this, greater attention on establishing a generalized and direct correspondence between the plasma state, thermodynamic conditions and characteristics of deposited structures is required.

## 3. Photo-assisted chemical vapor deposition

### 3.1 Photoirradiation-matter interaction during chemical vapor deposition

Photoirradiation-based processing serves various applications, including deposition, doping, chemical etching and ablation.[301–303] Photo-assisted or photo-initiated CVD utilizes photons generated from sources such as gas discharge lamp, inert gas-ion lasers, solid-state lasers, or excimer lasers to drive precursor decomposition. Typically, photons in the visible or ultraviolet (UV) spectrum (wavelength ~100-700 nm) are used, though infrared (IR) lasers are occasionally employed for precursor decomposition.[304,305] Precursor decomposition may occur through thermal effects (pyrolytic decomposition), non-thermal effects (photolytic/photochemical decomposition), or by a combination of both photophysical processes.[306,307] In addition to temperature, factors such as pressure, nature of the reactant, and thermal conductivities of the substrate, gas, and resulting deposit also influence the deposition rate during the pyrolytic process.[308]

In the pyrolytic process, a suitable laser is typically used to heat the substrate locally, creating a Gaussian distribution of irradiance on the focused region. This ensures that only the central part of the focused spot reaches the desired temperature for precursor decomposition and deposition. Conversely, in the photolytic process, directed radiation activates precursor molecules (e.g., AB) on the substrate or in the gas phase (Eq. (3)), leading to dissociation (Eq. (4)) or reactive dissociation (Eq. (5)), resulting in decomposition and deposition.

Absorption: $AB + h\upsilon \rightarrow AB^*$ (3)

Dissociation: $AB^* \rightarrow A + B$ (4)

Reactive decomposition: $AB^* + D \rightarrow E + F$ (5)

Additionally, if the energy supplied by the UV lamp or laser is high enough, ionization (Eqs. (6)-(8)) and radical formation (Eq. (9)) are concomitant reactions, leading to the formation of reactive species.[309,310]

Open Access Article. Published on 15 2025. Downloaded on 2025/6/3 7:37:30.
This article is licensed under a Creative Commons Attribution 3.0 Unported Licence.

Journal of Materials Chemistry A Accepted Manuscript



This journal is © The Royal Society of Chemistry 20xx

Please do not adjust margins

View Article Online DOI: 10.1039/D5TA01081K

Ionisation: $AB + h\upsilon \rightarrow [AB]^+ + e^-$ (6)

$AB + h\upsilon \rightarrow A^+ + B + e^-$ (7)

$AB + h\upsilon \rightarrow A^+ + B^-$ (8)

Radical formation: $AB + h\upsilon \rightarrow A^{\cdot} + B^{\cdot}$ (9)

In the photolytic process, precursor decomposition can occur at temperatures significantly lower than the pyrolysis temperature. This is achieved through energy transfer from the excited electronic states to the vibrational states of the precursor molecules.[311] The fraction of excited molecules undergoing bond dissociation and the corresponding reaction rate ($R_a$) can be represented using a modified Beer´s relationship, Eq. (10)

$$R_a = \left({}^{I_0}/_{h\nu}\right) F \exp\left(-\,{}^{\sigma_\lambda p l}/_{kT}\right) \quad (10)$$

where $I_0$ is the incident UV intensity, $h\nu$ is the photon energy, F is the photochemical quantum efficiency, k is Boltzmann's constant, $\sigma_\lambda$ is absorption cross-section for incident wavelength $\lambda$, p is partial pressure, $l$ is optical path length, and T is the absolute vapor temperature.[312] In the pyrolytic process, decomposition occurs at the substrate surface, and the deposition rate is kinetically controlled, with a high activation energy ($E_a$) of ~100 kJ mol$^{-1}$. In contrast, photolytic decomposition occurs in the gas phase where the deposition rate is diffusion-controlled, with a significantly lower $E_a$ of ~10 kJ mol$^{-1}$.[313] Additionally, the absorption of incident radiation by the substrate, such as a semiconductor, alters its surface charge state, which can induce catalytic activity, promoting reactions between the organic ligands of metalorganic precursors to form stable by-products or leaving groups. Their desorption facilitates enhanced film growth at temperatures much lower than those required for conventional thermal CVD.

Photolytic PACVD typically employs vacuum ultraviolet (VUV, wavelength <200 nm) lamps or lasers, emitting high-energy (5–15 eV) photons capable of cleaving most chemical bonds, as the initiation source. However, the limited light transmission at these wavelengths necessitates specialized reactor windows, such as $MgF_2$ and LiF, or advanced reactor designs. To overcome these limitations, short-wave UV light (200–280 nm) is often used, which can be transmitted through cost-effective quartz windows. This approach requires careful selection of precursors with reactive chemical bonds that can be activated at these wavelengths. To broaden the range of applicable precursors, especially for the deposition of polymers, photosensitizers and/or photo-initiators are used along with the monomers.[315]

### 3.2 Overview of photo-assisted chemical vapor deposition

The PACVD technique was initially developed to meet the demands of the semiconductor and microelectronics fabrication industry. Early reports of pyrolytic laser-assisted CVD (LACVD) include the deposition of silicon using a 50 W infrared $CO_2$ laser[316] and the deposition of carbon using a visible $Ar^+$-ion laser.[317] Important studies by Liu et al.[318,319], Ruzin and Nemirovsky[320], Irvine et al.[321], and Santos et al.[322] explored the theoretical and mechanistic aspects of LACVD. Comprehensive discussions of the key principles underlying PACVD can be found in earlier reference works.[312,323,324] Similarly, reviews by Sankur[325], Zhao et al.[22], and Hwang et al.[326] provide valuable insights into the advancements and applications of PACVD. **Table 2** presents selected reports on PACVD, displaying its importance in thin film fabrication for a range of materials.

**Table 2.** Selected examples of photo-assisted CVD used for the deposition of functional coatings of various compositions.

| Material/ Substrate | Photon source/Reaction | Key features | Application | Ref. |
|---|---|---|---|---|
| ***Carbon-based materials*** | | | | |
| Diamond/ Si (100) | Laser (wavelength: 532 nm)/ Photolytic | Coupling of laser with PECVD for increased crystal growth | Coatings; hardness=91 GPa, Young's modulus=721 GPa | 327 |
| Diamond/ WC or cobalt | UV laser (wavelength 193 and 248 nm)/Photolytic | Nondiamond carbon accumulation was minimised | - | 328 |
| Diamond/ SS 316 | $CO_2$ laser | 19 µm-thick diamond coating with a quality factor of 96% | Coatings; Enhanced adherence with metallic substrate due to stress relief and improved mechanical bonding | 329 |
| Diamond/ WC | Wavelength-tunable $CO_2$ laser | Enhanced growth rate by resonant vibrational excitation of $CH_2$-wagging mode in $C_2H_4$ molecules | Synthetic diamond; Grain size without laser (2.6 µm) increased to 10.494-14.3 µm with laser | 330 |
| Carbon-based materials/ Si or Cu | Nd:YAG Laser | Pulsed laser CVD; Cu foil was a more suitable substrate to grow pyrolytic carbon than $SiO_2$ | Pyrolytic carbon with graphene as its fundamental building block | 331 |
| ***Metalloids*** | | | | |
| SiOC-SiC/ Graphite | $CO_2$ laser/ Pyrolytic | Temperature-dependent auxiliary formation of amorphous $SiO_2$, β-SiC nanocrystals, and/or Si cystals | - | 332 |
| 3C–SiC/ Si (001) epitaxial films | YAG diode laser | Density of microtwins was controlled by dilution gas ($H_2$) flow | - | 333 |
| SiC-TaCN/ $Si_3N_4$ | Nd:YAG laser | For 1000 °C deposited film, hardness and Young's modulus ≈30.4 and ≈232 GPa, respectively | Tribological coating; (extreme penetration= 59.0 µm and surface roughness=3.5 µm) | 334 |

Open Access Article. Published on 15 2025. Downloaded on 2025/6/3 7:37:30. This article is licensed under a Creative Commons Attribution 3.0 Unported Licence.

Journal of Materials Chemistry A Accepted Manuscript



Please do not adjust margins

View Article Online
DOI: 10.1039/D5TA01081K

| | | | | |
|---|---|---|---|---|
| Silicon Nitride | InGaAlAs diode laser/ Photolytic | Lowest deposition temperature (1100 °C) so far for crystalline film; max. rate 972 µm/h at 1300 °C | Coatings; Vickers microhardness and nano-hardness 25.1 GPa and 34.8 GPa at 1300 °C respectively | 308 |
| SiN encapsulation film | ArF excimer laser | Two-step fabrication of SiN film using LACVD and LAPECVD | Thin-film encapsulation for organic light emitting diodes (encapsulation increases lifetime by 3.59 times) | 335 |
| Boron carbon oxynitride/ Si | Nd:YAG laser, 1050 °C; TDMAD precursor | Composition $B_wC_xN_yO_z$ was varied by regulating flow rates of the oxidation gas (i.e., air) | Phosphor; PL emission bands at 386–570 nm; intense emission bands at 534 and 570 nm for C- and O-rich films | 336 |
| ***Metals, oxides, chalcogenides, nitrides*** | | | | |
| Ru on thiolated self-assembled monolayers (SAMs) | Hg arc lamp | Ru and $RuO_x$ deposit on —$CH_3$- and —OH-terminated SAMs; no deposition on —COOH-terminations | - | 337 |
| N-doped α-$Fe_2O_3$/ Si | $Ar^+$ laser/ pyrolytic; Pulsed Nd:YAG laser | $Ar^+$ laser for deposition and pulsed Nd:YAG laser for crystallization and minimize the surface irregularities | Magnetic devices and photoelectrodes | 338 |
| Li-doped NiZnO/ c-axis oriented sapphire | Tungsten-halogen lamp (cutoff wavelength ~200 nm) | Compared to CVD, PACVD results in decreased defect density and lattice stress | Optoelectronics; NBE/DLE ratio=15.6 for PACVD compared to that of 3.2 for CVD | 339 |
| $SmBa_2Cu_3O_{7-\delta}$/ $LaAlO_3$ | Semiconductor laser, (wavelength: 808 nm) | $P_{O2}$ dependence of deposition rate, critical temperature ($T_c$) and critical current density ($J_c$) | Superconductive films; highest $T_c$ (89.2 K) and $J_c$ (2.04 MA/cm²) for film deposited with $P_{O2}$=200 Pa | 340 |
| $Eu^{3+}$-, $Dy^{3+}$-, or $Tb^{3+}$ -doped $HfTiO_4$/ quartz | Diode laser (continuous-wave mode; 1470 nm; 75 W) | Fast deposition rate (36 µm $h^{-1}$) | Phosphor; $Eu^{3+}$, $Dy^{3+}$, and $Tb^{3+}$ activated films displayed red, yellow, and green photoluminescence | 341 |
| $HfO_2$/ Si(100) | InGaAlAs diode laser/ Pyrolytic | Max. deposition rate (362 µm $h^{-1}$) was $10^2$-$10^4$ times higher than that obtained using existing methods | high-dielectric constant (k) material; k=16-22 | 342 |
| Arsenic doped p-type ZnO/ (GaAs/$Al_2O_3$) | Tungsten–halogen lamps (~200 nm cutoff; total input power 600 W) | GaAs layer acted as a doping source and its thickness controlled the doping level | Photoelectric device; hole concentration $3.1\times10^{16}$–$2.4\times10^{17}$ $cm^{-3}$ | 343 |
| $Tb^{3+}$-, $Eu^{3+}$-doped YAP/ (100) $SrTiO_3$ | $CO_2$ laser (10.6 µm; 60 W), ZnSe window | Deposition rate (53 µm $h^{-1}$) 50–90 times faster than for thermal CVD at 900-1003 °C | X-ray scintillation screen; Fluorescence decay constants 1.89 ms ($Tb^{3+}$:YAP) and 1.96 ms ($Eu^{3+}$:YAP) | 344 |
| $Ce^{3+}$-, $Eu^{3+}$-doped YAG–$Al_2O_3$ ordered eutectic system | $O_2$ laser (10.6 µm; 60 W), nSe window, 791-1030 °C | First report on formation of α-$Al_2O_3$ rod-like structure in YAG–$Al_2O_3$ composite | X-ray scintillation screen | 345 |
| Al-doped β-$Ga_2O_3$/ c-axis oriented sapphire | $O_2$ laser (10.6 µm; 60 W), 50-900 °C | Fast epitaxial deposition (15 µm $h^{-1}$) | X-ray scintillation screen; scintillation light yield=5400 photons per 5.5 MeV, decay response=5.1 ns | 346 |
| Gallium nitride/ (0001) GaN-on-sapphire | $O_2$ laser (9.219 µm; 50 W)/ Photolytic | ~60% reduction in carbon impurity incorporation ($5.5\times10^{15}$ $cm^{-3}$); (max. growth rate 4.5 µm $h^{-1}$) | Electron mobilities were 600-750 and 750-1275 $cm^2$ $V^{-1}$ $s^{-1}$, respectively, for normal and laser-assisted growth | 311 |
| GaN/ GaN | $O_2$ laser (9.219 µm; 00 W)/ Photolytic | High laser power suppressed the incorporation of carbon impurity | Trap concentrations were higher in laser-assisted GaN (up to $2\times10^{15}$ $cm^{-3}$) | 347 |
| ***Others*** | | | | |
| Poly(HEMA-co-4VP)/Electrospun cPCL | IV lamp, tert-butyl eroxide as initiator | piCVD-assisted crosslinking | Polymer degradation and drug delivery | 348 |
| Oligomeric film on CNTs | hort-wave UV lamp/ hotolytic, $H_2O_2$ initiator | piCVD; vertical chemical gradient formation to control hydrophilicity/hydrophobicity | Surface modification (wettability control) | 349 |
| Janus HEMA-PTFE membrane | IV (254 nm)/ Photolytic | piCVD | Membrane distillation (antifouling effect) | 350 |

*DLE– Deep level emission; HEMA– 2-hydroxyethyl methacrylate; NBE– Near-band-edge emission; PTFE– polytetrafluoroethylene; $P_{O2}$– Oxygen partial pressure; PL– Photoluminescence; TDMAD– Tetrakis(dimethylamino)diboron; YAP– Yttrium Aluminum Perovskite; YAG– Yttrium-Aluminum Garnet*

Photo-assisted CVD has been widely used for the deposition of metals,[351] oxides,[352] carbides,[334] nitrides,[311,347] carbonitrides,[334] and organic polymers,[353] targeting applications such as coatings and functional materials. PACVD has demonstrated significant versatility in tailoring the characteristics of deposited materials by independently or synergistically modulating the characteristics of photo-radiation such as intensity or source type, or integrating it with substrate heating or PECVD processes. Akazawa et al.[354,355] reported increased reactivity of $GeH_4$ precursor in PACVD of germanium on $SiO_2$ substrate using VUV beam as heat source, due to its gas phase photolytic decomposition. Lari et al.[356] reported a continuous aerosol photopolymerization technique for coating nanoparticles, where photosensitive nanoparticles initiated

Open Access Article. Published on 15 2025. Downloaded on 2025/6/3 7:37:30.
This article is licensed under a Creative Commons Attribution 3.0 Unported Licence.

Journal of Materials Chemistry A Accepted Manuscript



This journal is © The Royal Society of Chemistry 20xx

Please do not adjust margins

View Article Online
DOI: 10.1039/D5TA00108K

surface photopolymerization of monomers onto their surfaces. Kasparek et al.[357] studied the influence of different VUV sources on thiol-terminated films deposited from $C_2H_2$+$H_2S$ gas mixtures, indicating that the absorption coefficients of gases significantly affected the photolytic reaction kinetics and resulting film composition.

Photo-assisted MOCVD has resulted in the deposition of oxide films ($TiO_2$, NiO, ZnO, and NiZnO) with improved crystallinity.[339,343,358,359] It also provided a convenient method for depositing metals at a reasonable growth rate on thermally delicate structures, such as self-assembled monolayers.[337] McElwee-White and coworkers extensively investigated the photochemistry of suitable precursors,[337,351,360–362] indicating that the secondary photo-processes often strongly influenced the overall efficacy of precursor decomposition.[337]

In laser-assisted CVD, depending upon the laser fluence and mode of its application (direct or parallel to substrate, scan speed, etc.), the laser-matter interaction can be expressed via laser pyrolysis,[332,363,364] laser photolysis[328,365–367] or laser resonance sensitization.[368–370] LACVD displayed its utility in the fabrication of thin films of metals,[371–373] oxides,[338,344] nitrides,[152,308,311,347,374] carbides,[375] sulphides,[376–378] carbon-based materials,[329,331,379] and composites[334,380,381]. Several general or material-specific reviews highlight the versatility of LACVD.[307,370,379,382–388]

Odusanya et al.[331] investigated the role of deposition parameters (gas flow rate, temperature, laser power, time, substrate) in a pulsed laser-assisted CVD of carbon nanomaterials. Um et al.[379] reported laser-assisted direct writing of >10 nm thick highly-ordered graphite film on Ni substrate. Wu et al.[329,389] utilized femtosecond laser texturing of metal substrates to improve the adhesion of diamond coatings in laser-assisted combustion flame CVD. Moreover, laser-assisted photolysis of hydrocarbon precursors has been shown to effectively suppress nondiamond carbon formation and promote preferential crystallographic orientation in CVD diamond.[327,328,390]

Tu et al.[342] reported LACVD of $HfO_2$ films via a single growth process using InGaAlAs diode laser that created a lateral temperature gradient (100 K $mm^{-1}$) over the Si(100) substrate and resulted in four regions with different deposition temperatures (Fig. 4). The four regions followed different deposition kinetics, resulting in differential phase, microstructure, and morphological developments in these regions. The maximum deposition rate was $10^2$-$10^4$ times higher than that in previously reported deposition methods. On the other hand, Zhang et al.[380] achieved a vertical temperature gradient between the top and bottom of the coating during the growth of graphene/SiC composites over the Si nanowires. The light-trapping structure of nanowires enabled full utilization of the photothermal effect of laser at the top of nanowires, resulting in a larger surface area in the deposited film.

Open Access Article. Published on 15 2025. Downloaded on 2025/6/3 7:37:30.
This article is licensed under a Creative Commons Attribution 3.0 Unported Licence.

Journal of Materials Chemistry A Accepted Manuscript



Please do not adjust margins

View Article Online
DOI: 10.1039/D5TA01081K

ARTICLE

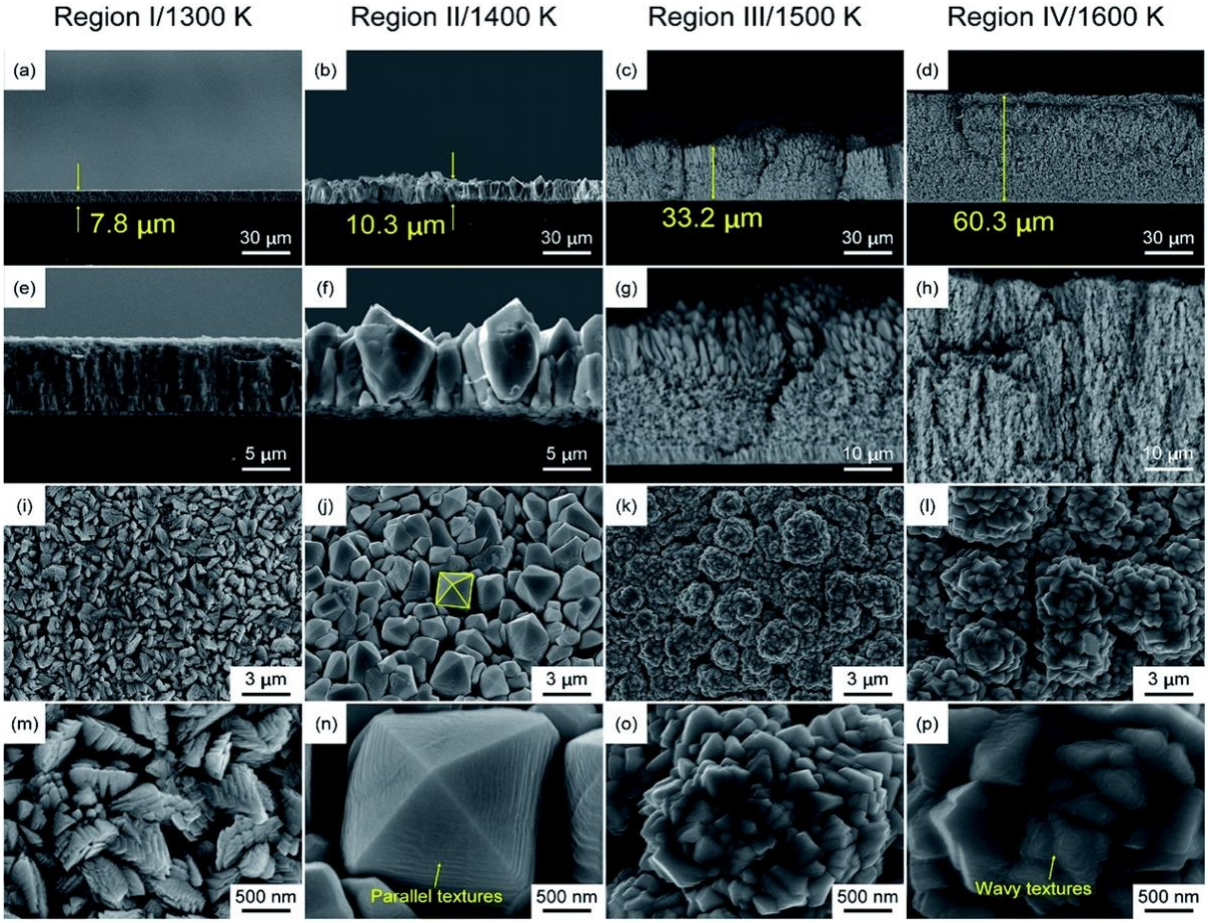


*Fig. 4. SEM images of cross-sections and surfaces of $HfO_2$ films in the four regions, obtained using the high-throughput growth process. (a), (e), (i), (m) Region I at T = 1300 K, (b), (f), (j), (n) Region II at T = 1400 K, (c), (g), (k), (o) Region III at T = 1500 K, (d), (h), (l), (p) Region IV at T = 1600 K, respectively. T represents deposition temperature, Reused with permission from Royal Society of Chemistry.*[342]

Open Access Article. Published on 15 2025. Downloaded on 2025/6/3 7:37:30.
This article is licensed under a Creative Commons Attribution 3.0 Unported Licence.

Journal of Materials Chemistry A Accepted Manuscript

View Article Online
DOI: 10.1039/D5TA01081K

Open Access Article. Published on 15 2025. Downloaded on 2025/6/3 7:37:30.
This article is licensed under a Creative Commons Attribution 3.0 Unported Licence.

Journal of Materials Chemistry A Accepted Manuscript

## ARTICLE

Zhang and coworkers[380,391–393] utilized LACVD to fabricate graphene/cubic silicon carbide (3C–SiC) composite films using hexametyldisilane as a single precursor. In these composites, the formation of graphene relied on the multi-step decomposition of hexametyldisilane, depending on the deposition temperature and pressure:[391]

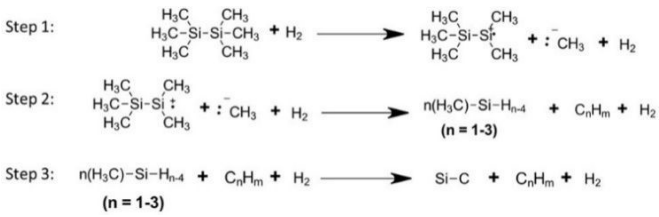


At lower deposition temperature and high pressure (i.e. at lower phonon energy per hexametyldisilane molecule), hexametyldisilane decomposition mostly proceeded to Step (2), resulting in a graphene-rich graphene/3C–SiC composite. Whereas at high deposition temperature and low pressure (i.e. at sufficient phonon energy per hexametyldisilane molecule), complete decomposition of hexametyldisilane ensured sufficient supply of $[(CH_3)_n–Si]$ clusters, resulting in pure epitaxial SiC films. A high distribution of graphene at the bottom of the film in transmission electron microscopy (TEM) analysis further supports this mechanism, as the formation of graphene predominantly occurred in the early stages of the heating ramp.

Laser-assisted CVD has emerged as a preferred method for the maskless fabrication of microdevices.[307,364,379,394] Laser-assisted vapor phase epitaxy, a variation of LACVD, resulted in selective area epitaxial growth of high structural and optical quality layers of III–V compound semiconductor, without masking or surface structuring.[395] LACVD has achieved a growth rate of ~84 μm $h^{-1}$ compared to ~2-3 μm $h^{-1}$ in normal CVD for the deposition of gallium nitride (GaN) transistors and diodes.[347,396] In CVD of GaN using ammonia as a nitrogen source, poor decomposition efficiency of ammonia leads to abundant carbon impurities. Conventional approaches to overcoming carbon impurities, such as increased carrier gas flow and high $NH_3$-to-Ga precursor ratio, have negatively affected the growth rate. LACVD has helped solve this issue without compositing with the growth rate. For example, by using a high-power $CO_2$ laser in LACVD of GaN film from trimethylgallium precursor, Zhao and coworkers[311,397] achieved >60% reduction in carbon

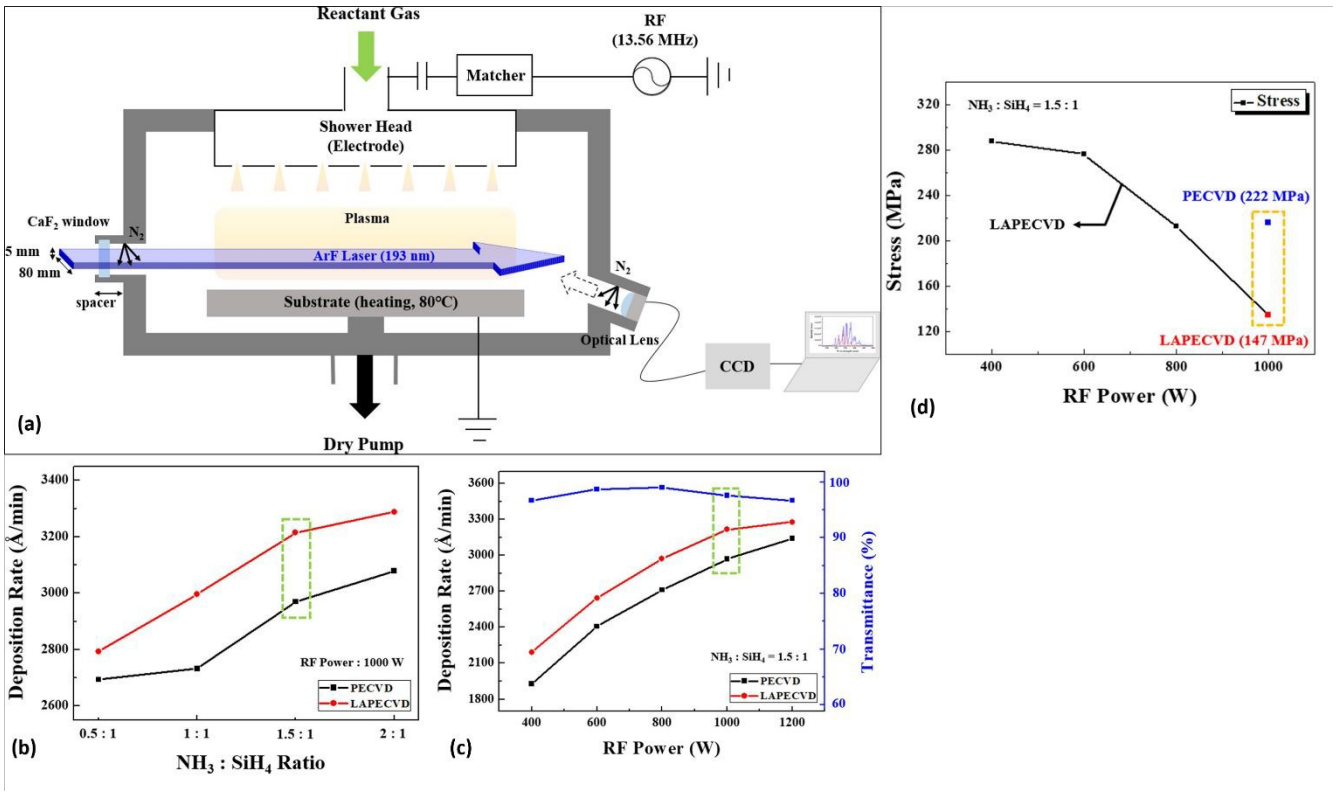


*Fig. 5. (a) Schematic of the LAPECVD system; Deposition rates for PECVD and LAPECVD, measured as functions of $NH_3$:$SiH_4$ ratio (b) and RF plasma power (c); and (d) Residual stress of silicon nitride films with plasma RF power, Reused with permission from Elsevier.*[152]

View Article Online
DOI: 10.1039/D5TA01081K

content with a high growth rate (4.5 μm $h^{-1}$). A strong interaction of $CO_2$ laser with $NH_3$ molecules at a wavelength (9.219 μm) matching with the rotational–vibrational transition of N–H wagging mode (1084.63 $cm^{-1}$) of $NH_3$ facilitated the $NH_3$ decomposition.[311]

Laser-assisted PECVD (LAPECVD) processes are developed for electronic and optoelectronic applications to avoid key drawbacks of PECVD, such as ion bombardment-induced substrate damage, nonstoichiometric composition, and residual stress.[152,335] For example, Kim et al.[152] used an ArF laser along with the $NH_3/SiH_4$ plasma (Fig. 5(a)) for the dissociation of reactive gases during the deposition of silicon nitride films. The LAPECVD-grown film displayed increased deposition rate (Fig. 5(b), (c)) and lower residual stress compared to the normal PECVD-grown film (Fig. 5(d)), due to the shift in composition towards the stoichiometric $Si_3N_4$. The LAPECVD-grown film displayed higher etching resistance due to the high film density resulting from its higher nitridation. Moreover, the organic light-emitting device employing the LAPECVD-grown passivation layer displayed improved performance without any electrical damage.

The initiated chemical vapor deposition (iCVD) is widely used for organic and hybrid polymer films, where thermal activation of a volatile initiator is employed to commence the polymerization of monomers.[353] In iCVD, thermal activation generally needs an active cooling strategy to keep the substrate temperature conducive for adsorption, which can be arduous for complex or poorly thermal-conducting substrates. To address this, initiation-polymerization can be achieved by gas phase or surface photoactivation of initiator/monomer(s) in photo-initiated CVD (piCVD), thus eliminating the requirement of high-temperature sources.[279,315] Typically, piCVD needs a judicious selection of a primary monomer(s) reaction mixture, often without any initiator and sensitizer, based on its capacity to undergo photo-induced polymerization in the gas phase or onto the substrate. In recent years, piCVD has been widely used for the deposition of polymeric films and the surface functionalization of nanomaterials.[22,348,349,353,398] The utilization of photon energy to initiate and propagate the polymerization process in functional films for biochemical/biological applications has eliminated the requirement of potentially toxic initiators and crosslinkers.[348,399,400] The piCVD has been preferred for surface modification.[401,22,315,348,398,349] In this regard, to overcome the constraints of a limited range of photochemically active precursors, initiators and sensitizers, a syngas piCVD is proposed, where syngas ($H_2$+CO) is photoexcited by short-wave UV radiations to produce radicals and reactive species.[315,398,402,403] Tavares and coworkers studied the kinetics of syngas piCVD,[315,402,404] and employed it for the deposition of thin films and surface treatment of polymers and nanoparticles.[398,405–407] The piCVD achieved large-scale (5 g) encapsulation of magnetic iron oxide nanoparticles in a jet-assisted fluidized bed configuration.[406] The piCVD is used to regulate the surface wetting behavior.[349,407,408]

Photo-assisted manipulations employing the ablation and annealing effects of laser are extensively used complementary to the main CVD process, influencing the composition, crystallographic orientation, and morphology of the substrate and 'preparing' it for the deposition of a desired material in the subsequent CVD step.[326,375,409,410]

### 3.3 Perspective on photo-assisted chemical vapor deposition

Photo-assisted manipulations in CVD enable the deposition of films and arrays with impressive substrate adhesion, high quality, and high deposition rate. Using PACVD, low-temperature deposition of selected area (using laser) and relatively large area (using UV lamps) film on thermally labile substrates are easily achieved. Unlike the PECVD where bombardment of aggressive plasma species may cause some damage to the film, PACVD-grown films are free from such artifacts. However, for using a VUV source, window composition has been one of the major factors in reactor design. The range of photolytic PACVD has been limited by the availability of photosensitive reactants. Photosensitizers and photoinitiators are employed to extend this range, however, their high cost is still a major constraint. The paucity of a universal and readily activated photoinitiator, such as the thermally activated peroxides in iCVD, is still a concern.

Syngas piCVD has been a convenient and economical method for organic film deposition and surface functionalization. However, it is limited to carbonaceous materials and requires further understanding of the role of syngas composition and iron species on deposition chemistry and kinetics. Moreover, organic substrates and deposited films can often be susceptible to photo-induced degradations, limiting the quality of the films.

PACVD and its variants provide a convenient method for the deposition over thermally delicate structures, such as self-assembled monolayers. However, to achieve this, the development of new precursors with a greater understanding of their photochemistry is desired. PACVD is not suitable for deposition on transparent substrates. Similarly, the importance of LACVD rests in ensuring selective area deposition, however, the area of deposition is limited by the laser spot size. The Gaussian distribution of irradiance around the focused spot even renders it less suitable for nanoscale direct writing over a large area. In this regard, plasmon-assisted CVD, suggested by Boyd et al.[411] where localized heating induced by surface plasmon of nanostructured metals is used for nanoscale heating and subsequent deposition, can be an alternative in some cases, especially where contamination by nanostructured metal layer is not an issue. However, a potential use of this Gaussian distribution of laser irradiance can be in creating a nanoscale temperature gradient during the molten metal-catalyzed growth of nanostructures. This, under some conditions, can manifest in interesting physicochemical effects on deposition and growth kinetics, e.g., the Marangoni effect in $SiO_2$ during field-assisted CVD growth of CNTs[412] and in differential phase, microstructure, and morphological developments in $HfO_2$[342].

Open Access Article. Published on 15 2025. Downloaded on 2025/6/3 7:37:30.
This article is licensed under a Creative Commons Attribution 3.0 Unported Licence.

Journal of Materials Chemistry A Accepted Manuscript



This journal is © The Royal Society of Chemistry 20xx

Please do not adjust margins

View Article Online DOI: 10.1039/D5TA01098H

Moreover, the idea of using a laser for selective alteration of specific chemical bonds or excitation of vibration modes in reacting species and thus imparting chemical selectivity[413] is less explored in CVD and needs greater attention.

## 4. Electric field-assisted chemical vapor deposition

### 4.1 Electric field-matter interaction during chemical vapor deposition

The interaction of the external electric fields with matter (atoms or molecules) has a range of effects, with the Stark effect displaying the splitting of energy levels being the most prominent manifestation. Theoretical calculations suggest that an EF of 1-10 V $nm^{-1}$ can alter the $E_a$ of gas phase reactions by several kJ $mol^{-1}$. The application of such an intense EF on reaction volume is challenging due to the dielectric breakdown of the medium.[414] However, an externally controlled moderate EF provides efficient ways to alter the reaction chemistry via its direct interaction with the participating species (atoms, molecules, or other complex matter), influencing the electron transfer/charge migration, geometry and/or bond strength, and interfacial behavior.[415–417] When an external EF is coupled with the CVD process, the precursor molecules having a permanent or induced dipole interact with the field and gain kinetic energy, increasing their probability of reaching the substrate surface.[418] The gaseous precursor may assume a preferred orientation towards the substrate and, if EF is sufficiently strong, some of the bonds in precursors get activated along the direction of the dipole, reducing the energy of nucleation and executing a preferred growth orientation.[23]

During the CVD process, externally controlled electrical biasing of the substrate-containing electrode has played an important role in bias-enhanced nucleation (BEN)[90,419,420] and bias-enhanced growth[421]. In processes involving the gas phase formation of charged nanoclusters, the application of electrical bias directs these clusters toward the substrate, where they act as nucleation centers for deposition.[419] For example, during the deposition of diamond and carbon nanotubes, the gas-phase flux contains, respectively, the positively and negatively charged carbon fragments. Therefore, the substrates, which are negatively-biased (in diamond deposition) and positively-biased (in carbon nanotubes deposition), promote nucleation and growth (Fig. 6 (a)).[422–426] Additionally, the nature of external electrical bias (i.e., DC/AC) has been an additional control parameter, with voltage and AC bias frequency significantly affecting the microstructure evolution and growth rate.[23,427–429]

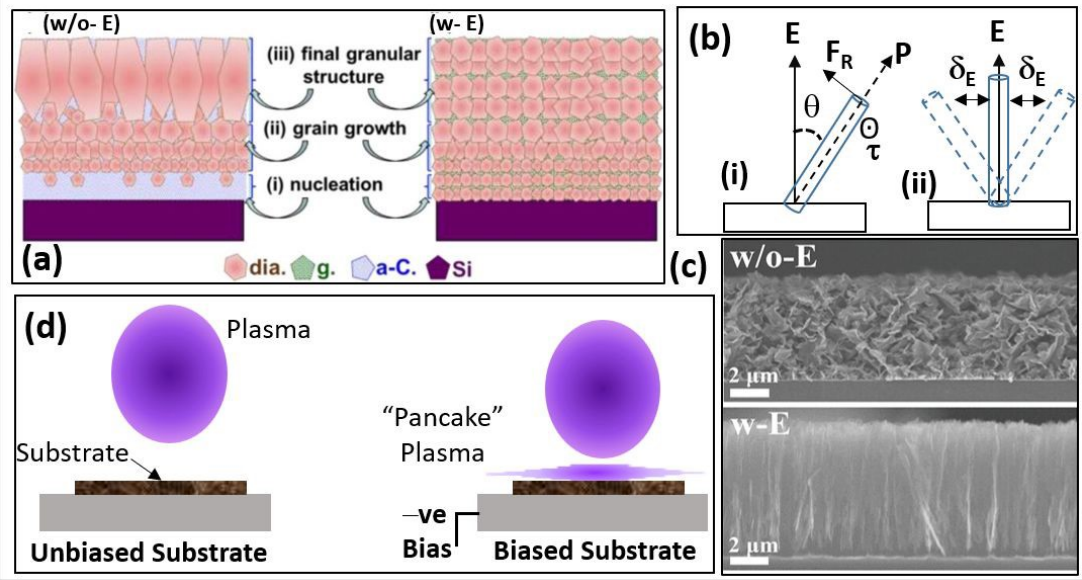


*Fig. 6. (a) Schematics of bias effect on evolution process for the granular structure of diamond films with (w-E) and without (w/o-E) EF. The bias condition displayed an increased and instantaneous nucleation (i), moderate grain-growth (ii), and coexistence of some graphitic phase (iii), Reused with permission from ACS;[421] (b) Schematic showing a single-walled carbon nanotubes in an EF (i) and its vibration in an EF (ii);[428] (c) SEM images showing the effect of EF on growth of vertical graphene arrays and graphene nanowalls, Reused with permission from Wiley;[188] and (d) Effect of electrical bias on plasma appearance in PECVD of diamond films[429].*

From a non-classical nucleation point of view, the charged nanoclusters originating at the initial stages of precursor decomposition in CVD act as building blocks for 1D nanostructures such as nanowires and nanorods. For CVD growth of such nanostructures, applied external electrical bias, apart from influencing their velocity and population at the substrate via a repelling or attracting influence, also provides directional control over the growing nanostructures.[430] For example, during EF-assisted growth of 1D materials such as CNTs, the dipole-induced torque directed the growing 1D

Open Access Article. Published on 15 2025. Downloaded on 2025/6/3 7:37:30. This article is licensed under a Creative Commons Attribution 3.0 Unported Licence.

Journal of Materials Chemistry A Accepted Manuscript



Please do not adjust margins

View Article Online
DOI: 10.1039/D5TA01081K

nanostructure to align along the EF, enabling a sustained oriented 1D growth (Fig. 6(b)).[188,431] Similarly, external EF-induced in situ manipulation helped the formation of doped nanostructures, e.g., by inducing electromigration of dopant species,[432] and homojunctions, e.g., by sequential growth of the Sb-doped p-type ZnO microwires (with EF) along the undoped n-type ZnO microwires (without EF).[433]

In PECVD, external EF has been used to influence the distribution of plasma around the substrate. The negatively charged plasma wall, due to the higher mobility of electrons compared to the ions, is attracted or repelled toward the substrate, depending upon the substrate bias (Fig. 6 (d)). The external EF also led to the decoupling of ion flux and ion energy[251,263,434] and exerted control over the electric field concomitant with the plasma[183,435,436]. Such external bias-controlled ion energy and plasma flow characteristics have influenced various phenomena such as ad-atom migration, desorption, itching, and displacement of lattice atoms in the growing film, affecting its characteristics- growth rate, crystallinity, density, and stoichiometry.[437,438]

### 4.2 Overview of electric field-assisted chemical vapor deposition

The use of externally applied electrical bias in CVD can be traced back to the work of Sawabe and Inuzuka[24] on the hot filament CVD (HFCVD) of diamond film, displaying an increased deposition rate due to a 150V bias-induced enhanced electron bombardment on the substrate surface. Yugo et al.[25,419] used an external EF-induced pre-deposition process to generate diamond nuclei under a minimum bias voltage of -70V during the PECVD of diamond. Yoshimura et al.[439] reported the fabrication of molecular-aligned polymer film by employing a strong (0.78 MV $cm^{-1}$) external EF. The external EF-assisted CVD process gained momentum in the 1990s[418,439–441] and was well-received during the 2010s[23,433,442–454]. It has been employed in CVD of metal[455] and 1D/2D materials (hexagonal boron nitride,[456] carbon microcoils and nanotubes,[28,457] graphene[183]), AACVD of metal oxides,[449,453,454,458–461] and PECVD of microcrystalline silicon[462]. The EF assistance in CVD has been focused on manipulation of deposition and growth,[463] growth direction and crystallographic orientation in nanostructures,[183,433,454,464] defects,[435] selective growth (phase composition and crystallinity)[431,433,465]. **Table 3** presents selected examples of EFCVD used for the deposition of functional coatings.

**Table 3.** Selected examples involving electric field-assisted manipulations in CVD of functional materials.

| Material/ substrate | Bias | Key Effect of EF | Application | Ref. |
|---|---|---|---|---|
| ***Metal oxides, carbides, nitrides, etc.*** | | | | |
| ZnO/ Si | 0-700 V | No deposition in absence of EF; shape and size changes with increasing bias | - | 466 |
| β-$Ga_2O_3$/ Sapphire | 0–80 V | Improved growth rate & crystal quality; a blue shift in absorption with increasing V | Direct wide band gap semiconductors; $E_g$=4.59-4.94 eV | 465 |
| ZnO, CdO and PbO/ fluorine-doped tin oxide (FTO) | ~625 V $cm^{-1}$ | EFCVD films displayed enhanced photocurrent in 0.1 M $Na_2SO_4$ compared to those deposited without EF | Photoelectrochemical; j values for ZnO, CdO and PbO in light and dark were 207, 263, 237 and 1.55, 215, 1.67, respectively | 463 |
| $VO_2$/ FTO | 1-10 V $cm^{-1}$ | Reduction in crystallite size and thermochromic transition temperature | Glazing material | 452 |
| $TiO_2$/ glass | 0-30 V | EF induced changes in particle size and shapes, agglomeration, and composition | Photocatalytic dye degradation | 453 |
| | | | | |
| $TiO_2$/ FTO | 0-30 V | EF induced changes in particle size and shapes, and preferential crystal orientations | Antimicrobial and photocatalytic application | 454 |
| Silicon | ±1000 V | -ve bias is more favorable than the +ve bias | - | 467 |
| SiC | ±50 V | -ve bias promotes epitaxial growth | - | 468 |
| ***Carbon-based materials*** | | | | |
| Vertical graphene (VG)/ Si | 0-60 V | EF assistance in PECVD; Height of VG arrays increased with the bias (18.7 µm with an EF of 30 V $cm^{-1}$) | Thermal interface material; high vertical thermal conductivity (53.5 W $m^{-1}$ $K^{-1}$) and a low TRC (11.8 K $mm^2$ $W^{-1}$) | 188 |
| Vertical graphene (VG)/ Si | –60-250 V | EF assistance in PECVD; High growth rate (11.5 µm $h^{-1}$) | Thermal interface material; vertical thermal conductivity (34.2 W $m^{-1}$ $K^{-1}$) and a low TRC (18.2 K $mm^2$ $W^{-1}$) | 190 |
| Vertical graphene/ Cu | –400-400 V | Deposition rate decreased with increasing –ve bias but opposite effect with +ve bias | - | 431 |
| Vertical graphene | 30 V $cm^{-1}$ | Straight pore structure & enhanced electrochemically active surface area for efficient ion/electron transport pathways | Electrochemical capacitors; $C_a$=1.72 mF $cm^{-2}$ at $\Phi_{120}$=80.6° after 500k cycles, energy density= 0.33 µWh $cm^{-2}$ | 191 |
| Quenched-produced diamond/ Ti | –40 V | Spontaneously formed TiC interfacial layer caused a 3-fold increase in adhesion strength | Coatings for biomedical devices; Hardness=96 GPa | 424 |
| Diamond/ Si(100) | 150-250 V | Bias voltage plays a key role in the formation of azimuthally (70%) textured diamond film | Quantum devices; diamond films with N vacancy defect centres | 90 |
| Vertical graphene | 100 V | EF-assisted PECVD; Max. growth rate=15.9 µm $h^{-1}$; VG height ~144 µm | Light shielding; ultra-low reflectance of 0.25% | 189 |
| Carbon nanotubes | 0-30 V | Growth rate increased and diameter decreased with higher +ve voltage | EF-assisted mass production of CNTs | 469 |

Open Access Article. Published on 15 2025. Downloaded on 2025/6/3 7:37:30.
This article is licensed under a Creative Commons Attribution 3.0 Unported Licence.

Journal of Materials Chemistry A Accepted Manuscript



This journal is © The Royal Society of Chemistry 20xx

Please do not adjust margins

View Article Online
DOI: 10.1039/D5TA01081K

| | | | | |
|---|---|---|---|---|
| Carbon nanotubes | 0-700 V | "herringbone structure" (diameter 25 nm) in no field, uniform parallel to the tube axis (diameter 12 nm) in EF | Supercapacitor; C= 237 F $g^{-1}$ (3-fold increase compared to no field) | 470 |
| "Cow-nipple-like" submicro-nano carbon | 0-300 V | A vertically grown carbon nanotube (dia. 10-40 nm) upon a carbon ball (dia. 30-120 nm) | - | 471 |
| ***Others*** | | | | |
| Perfluoropolyether on diamond-like carbon | 0-300 V | An EF-modulated photoelectron-assisted CVD | Ultrathin perfluoropolyether/DLC hybrid coatings for magnetic disks | 472 |

$C_a$- Specific areal capacitance; C- Specific capacitance; j- Photocurrent density (in μA $cm^{-2}$); TRC- Thermal contact resistance

External EF assistance has shown a remarkable impact in aerosol-assisted CVD (AACVD) of metal oxides,.[449,453,454,458–461] Beyond the magnitude and polarity of the applied bias, factors such as the type of current (AC vs. DC), frequency,[458] aerosol delivery setup and substrate orientation[461] significantly influenceparticle size and shapes, agglomeration, and phase composition and preferential crystal orientations.[453,454] The trajectory and flight time of aerosol droplets, charged either due to polarized molecules or static surface charges are influenced by the EF parameters. For example, in the deposition of $WO_3$ using $[W(OPh)_6]$ aerosol in toluene, applying AC voltage rather than DC voltage resulted in aligned and evenly distributed fibrous growth. This is attributed to the higher impedance of AC fields, which prevents the rapid dissipation of induced dipoles in the growing material, thus maintaining the alignment of the fibers with the field.[458] In the CVD of β-$Ga_2O_3$ on patterned sapphire substrate, external EF (0-80 V) was found to significantly affect the growth rate, morphology, and crystallinity.[450,465] The growth rate increased with increasing EF, forming uniform and regularly arranged microstructures. X-ray diffraction (XRD) analysis indicated increased preferential growth along (-201) plane of the monoclinic crystalline phase of β-$Ga_2O_3$ with increasing external voltage.[465]

The EF-assisted CVD processes have played an important role in understanding the non-classical charged nanocluster-based nucleation and growth. Hwang and coworkers[427,466–468,473–475] have studied the formation of charged nanoclusters and their deposition behavior under different bias conditions (substrate bias, filament bias in HFCVD, AC vs. DC bias) in CVD. In HFCVD of SiC, a negative bias of hot filament led to the formation of smaller charged nanoclusters compared to that in positive or zero bias, which displayed liquid-like properties and promoted epitaxial growth through epitaxial recrystallization.[468] In CVD of diamonds, the electrical bias accelerated the charged nanoclusters formed in the gas phase towards the substrate to act as nucleation centers and execute a bias-enhanced growth.[476,477] In CVD process, diamond deposition is also accompanied by an undesirable graphitic phase and EF-assisted +ve substrate biasing suppresses this graphitic phase.[476] Wang et al.[425] studied the evolution of nucleation and growth of heteroepitaxial single-crystal diamond film with substrate bias on Ir substrate, displaying a close relation between bias voltage and bias time. The bias-enhanced nucleation experienced incubation and domain-nucleation periods where domains can enlarge and diminish with bias time, resulting in the nucleation pathways changing from "isolated-crystal nucleation" to "typical domain nucleation" and again back to "isolated-crystal nucleation".

In HFCVD of anisotropic carbon-based nanomaterials, external electrical bias influences the deposition rate, composition, and orientation of growing nanostructures.[478,479] For example, during catalytic deposition, the axis polarizability of 1D-carbon nanostructures in EF has caused them to be lifted upward from the horizontal direction, enabling them to grow more readily from the catalyst surface.[443,470,480] Zhang and Pan[481] demonstrated a bias-dependent diameter variation of carbon nanofibers using Ni nanocatalysts. An external bias of 0, 25 and 50 kV $m^{-1}$, respectively, influenced the size of nanocatalysts, which become liquid at the deposition temperature, resulting in nanofibers with 19.2±8.6, 13.8±4.7, and 8.0±2.4 nm diameter. Similarly, Peng et al.[443] exploited the greater polarizability of metallic-CNTs compared to the semiconducting-CNTs to raise the percentage of metallic-CNTs to 80% with EF-bias of 200 V $cm^{-1}$ compared to that of 47% with zero field bias. Luo et al.[470] observed that the CNTs grown under EF displayed a smaller and uniform diameter, improved crystallinity and graphitic nature, and fewer graphite layers parallel to the tube axis. Issman et al.[464] used external EF for continuous alignment of CNT bundles (Fig. 7). The theoretical model simulating the alignment process indicated that a CNT stiffening effect (introduced by a z-pinch mechanism induced by Lorentz force of the AC field, rather than DC fields) enabled a means to control CNT bundle diameters. The EF-assisted samples displayed 75-90% increase in specific electrical conductivity and 260-320% increase in specific tensile stress to failure, compared to the zero-field sample.

Open Access Article. Published on 15 2025. Downloaded on 2025/6/3 7:37:30.
This article is licensed under a Creative Commons Attribution 3.0 Unported Licence.

Journal of Materials Chemistry A Accepted Manuscript



Please do not adjust margins

View Article Online
DOI: 10.1039/D5TA01081K

Open Access Article. Published on 15 2025. Downloaded on 2025/6/3 7:37:30.
This article is licensed under a Creative Commons Attribution 3.0 Unported Licence.

Journal of Materials Chemistry A Accepted Manuscript

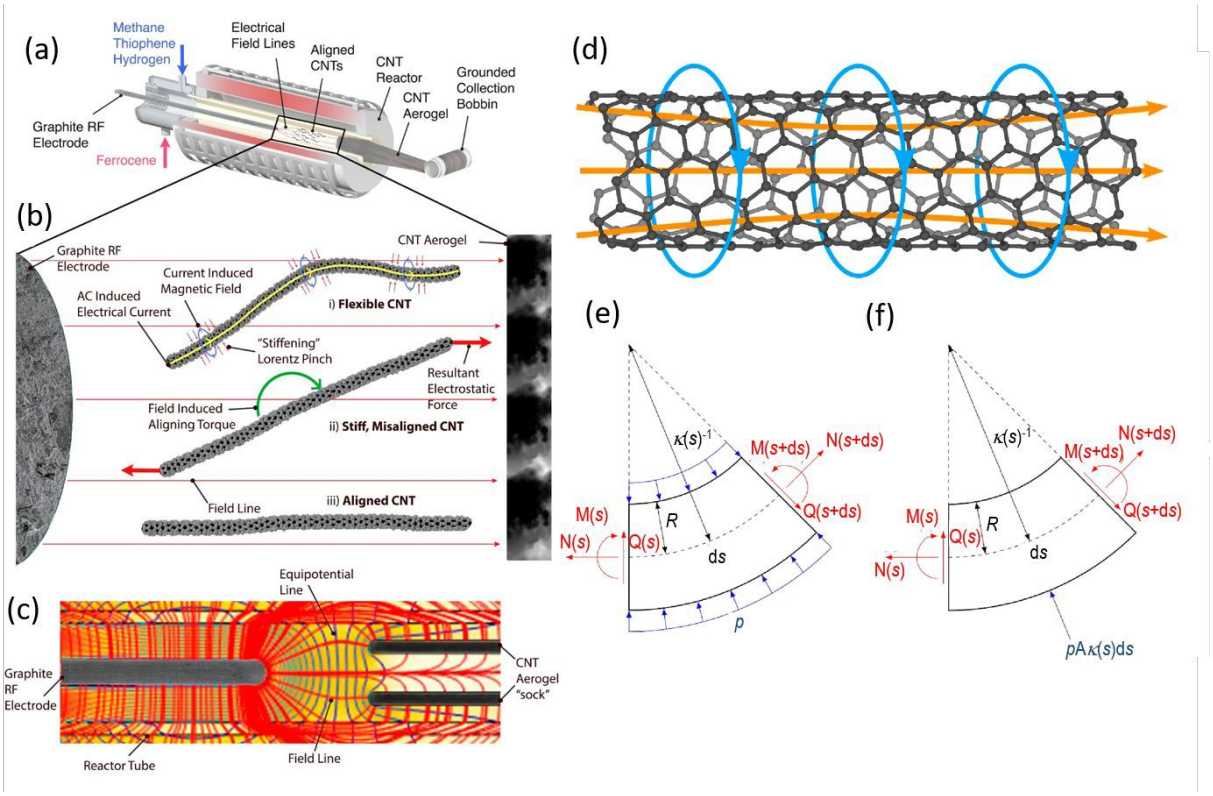


*Fig. 7. (a) An illustration of EFCVD reactor with an RF electrode inserted at its front, while the forming CNT aerogel acts as a counter electrode. (b) A magnified schematic shows the occurrence in the interelectrode gap: (i) AC field induced "Lorentz pinch" stiffens the ultralong CNT, (ii) Stiff, ultralong CNT is under the influence of a field-induced aligning torque, (iii) CNT is aligned according to the field lines. (c) Finite element method numerical results of field distribution inside the reactor tube portraying equipotential lines (blue) and orthogonal field lines (red). The packing density of the equipotential lines indicates the local field intensity. The model shows the presence of alignment-inducing field lines bridging the two electrodes within the interelectrode gap (50 mm wide). (d) SEM micrographs of the fracture surface of materials produced by the internal RF electrode setup. (1-4, low-magnification images; 5-8, high-magnification images). Image Ref represents zero-field sample, whereas aligning EF was created by varying the RF power (shown in watts), Adopted with permission from ACS.*[464]

Linnik et al.[482] reported RF (13.56 MHz) bias-enhanced nucleation of diamond on dielectric substrates where the nucleation density obtained on sapphire and Si substrates were $10^{10}$ and $10^{11}$ $cm^{-2}$, respectively. In PECVD of carbon-based nanomaterials, internal EF associated with the plasma plays an important role in oriented growth.[183,186,483] However, additional electrical biasing has also been enforced, ensuring vertical growth and/or enhancing desired materials attributes.[188] For large-area deposition of high electrical conducting graphite-like carbon film in PECVD, high and uniform plasma density and effective ion bombardment (i.e., high plasma energy) are needed to increase graphitic character. To this, Bae et al.[434] used high negative substrate bias (up to 2 kV) to decouple the ion flux with ion energy, enhancing the ion bombardment energy (≥1.3 keV) of $Ar/C_6H_6$ surface-wave plasma (plasma density $\geq 10^{17}$ $m^{-3}$) for the deposition of $sp^2$ carbon-rich films. With increasing bias, the deposition rate decreased, but the graphitic character increased, resulting in a highly conducting large area (16 cm) film. In PECVD, diffused/remote plasma configurations overcome the issues of defect creation and etching, which are observed in direct plasma configuration. However, in vertical growth of carbon nanomaterials, diffused/remote plasma configurations may also lead to horizontal growth.[484–487] The application of an additional external substrate bias with respect to the electrically grounded chamber wall minimized the horizontal growth.[58,184,186] Butcher et al.[488] used a biased grid placed between the plasma and the substrate, shielding the substrate from the strong EFs generated by the RF plasma during PECVD of GaN. PECVD with grounded grid resulted in highly smooth films, whereas +ve grid biasing led to columnar growth. Interestingly, -ve grid biasing significantly reduced the carbon and hydrocarbon content of GaN films. Similarly, by placing metal-covered Si half-rings around an Ir/YSZ/Si(001) substrate, Yoshikawa et al.[489] demonstrated wafer-scale bias-enhanced nucleation and heteroepitaxial growth of single-crystalline diamond by PECVD, with the half-rings and their

 This journal is © The Royal Society of Chemistry 20xx

Please do not adjust margins

View Article Online
DOI: 10.1039/D5TA01681H

Open Access Article. Published on 15 2025. Downloaded on 2025/6/3 7:37:30.
This article is licensed under a Creative Commons Attribution 3.0 Unported Licence.

Journal of Materials Chemistry A Accepted Manuscript

thickness influencing the bias-enhanced nucleation density and the plasma density distribution. Some studies have reported innovative ways to execute the EF-mater interaction in CVD. For example, Reiprich et al.[490] reported an EF-guided localized and programmable CVD method to deposit 3D materials. The electrically charged precursor molecules were guided by the arrays of electrodynamic funnels to nanosized (≥250 nm) deposition locations, where nearest neighbor coupling led to the deposition of 3D nanostructures. Shi et al.[491] reported double bias induced post-deposition nanostructuring of boron-doped diamond film via a reactive ion etching process, introduced by negative substrate bias (250-300 V) and positive bias (0-60 V) of a strategically placed grid in HFCVD system. The double biasing greatly improved the etching efficiency, forming nanocone structures with enhanced electrochemically active surface area.

Some studies simulated the physical processes on the scale of the apparatus in EF-assisted PECVD to present mathematical models relating the electrical bias with the deposition rate.[492,493] For example, to explain the diamond growth from $CH_4/H_2$ gas mixture in EFCVD, Lifang et al.[494,495] performed Monte Carlo simulation correlating the energy carried by electron and precursor fragments as a function of experimental parameters. For metal-catalyzed CVD of CNTs, Saeidi and coworkers[496,497] presented a theoretical model relating the external EF with the phonon oscillations of metal catalysts. They demonstrated that a catalyst-specific optimum electric field was required, depending upon the metal-carbon van der Waals interactions, atomic mass, and free charge carrier density of metal atoms.[497] Wang et al.[438] proposed a two-dimensional axisymmetric model to understand the influence of positive bias and deposition pressure on the plasma flow properties in the deposition chamber during bias-enhanced PECVD process, predicting a bias voltage threshold phenomenon with a narrow range of suitable voltage.

### 4.3 Perspective on electric field-assisted chemical vapor deposition

The imposition of external EF around the assembly of precursors, carrier gas, and substrate has provided a non-contaminating way to manipulate the CVD process. However, except for bias-enhanced nucleation in diamond growth and aligned growth of nanostructures, the potentials of EF-assisted modulations seem to be underutilized in CVD. Previous studies have focused mainly on the realization of EF-assist on isolated, lab-scale deposition processes, which should be tested at industrial scale, given the importance of CVD in modern manufacturing. In this regard, recent reports of employing EF-assisted modulations in tuning the ion energies in plasma-assisted atomic layer deposition,[498,499] an offshoot technique of PECVD, warrant renewed attention in EFCVD.

Electric field-driven, potentially non-thermal mechanisms have proven their significance in materials synthesis and processing,[500] manifesting far-from-equilibrium effects at a range of length scales–from atomic level to microstructural level–and therefore should not remain ignored in CVD. The reports of using an external electric field to influence defect creation and defect migration during materials processing[432,433,435,501,502] should be extended to the EFCVD of diverse functional materials.

Most reports on EFCVD remain confined to lab-scale demonstrations, primarily due economic constraints and challenges of process integration. In addition, limited understanding of EF-matter interaction in CVD parametric space also poses a significant barrier to broader adoption of EFCVD. As nucleation and film growth are mediated by charged nanoclusters generated in the gas phase during CVD,[466,473,503–505] there is a growing need for studies investigating the influence of external EF effects on electrostatic energy and drag force acting on these nanoparticles, particularly in relation to floating, grounded, or biased substrates. Such investigations accompanied by appropriate modeling efforts, specifically focusing on the influence of external EF on the reactivity, mass and heat transfer, and reaction kinetics would provide valuable insights to optimize EFCVD processes and scale them for practical applications.

## 5. Magnetic field-assisted chemical vapor process

### 5.1 Magnetic field-matter interaction in chemical vapor deposition

Depending upon the time-space properties of the field, an MF-matter interaction has manifested into any or a combination of phenomena- Zeeman effect, magneto-thermodynamic effect, magnetic torque, Lorentz force, Faraday force, eddy current, and energy injection.[506] Quantitatively, an external magnetic field of 1 T induces ~0.05 $J \cdot mol^{-1}$ change in Gibbs free energy of a chemical reaction at room temperature, influencing the rate constant by a seemingly insignificant factor of ~$10^{-5}$.[507] However, these low-energy magnetic interactions have displayed a noticeable influence on chemical kinetics and the outcome of the chemical reactions.[508] For example, when a magnetic field is applied in the course of precursor flow in CVD, polar molecules and charged particles move in a cyclical way under the influence of the MF-induced Lorenz force, making their movement trajectories overlap more frequently. This increased the probability of collision between reacting species and carrier gas molecules.[26] An external MF influenced the nucleation process and, depending upon the difference in magnetization between the vapor phase and the substrate, provided an extra driving force in the form of Zeeman energy, thus lowering the energy barrier for nucleation on the substrate surface.[509] A sufficiently strong and favorably oriented MF influenced the mobility and diffusion of precursor molecules onto the substrate surface, altering the crystallization temperature, phase separation, and morphology in the resulting film.[510] The coupling of MF with other field effects-electric field,[27,28,31] plasma,[29,30,511] or both[26,27,31,512,513] has resulted in a synergistic effect, leading to the deposition of films with unique nanostructures.

### 5.2 Overview of magnetic field-assisted chemical vapor deposition



Please do not adjust margins

View Article Online
DOI: 10.1039/D5TA01084K

The initial reports on externally controlled MF assistance in CVD process can be traced back to the 1980s when it was used to influence the plasma properties during PECVD, displaying variable effects of MF on plasma and resulting deposition, depending upon the MF strength, precursor characteristics, and plasma and thermodynamic parameters.[514–516] For example, MF was used to confine the plasma density over the substrate, enhancing the deposition rate and film quality of DLC films.[517–519] The confinement of a low RF power plasma by an MF parallel to the substrate surface effectively enhanced the plasma density without increasing the ion energy, resulting in a high deposition rate at low DC self-bias (sheath voltage). In the absence of MF, only a high RF power input could ensure a high growth rate. However, a high RF power resulted in a high sheath voltage and ion energy, causing a potential deterioration in film quality. The external MF influenced the plasma sheath parameters by affecting the ion flux and ion energy.[516] A streamlined magnetic field has been used to stabilize the RF plasma over long-range propagation, enabling high plasma density with a decay-free, uniformly distributed ion energy over an extended space, thus offering an energy-efficient means for scalable fabrication of films of 1D/2D materials.[511,520–522] **Table 4** presents selected examples of MF assistance employed in CVD of functional coatings.

**Table 4.** Selected reports on external MF assistance in CVD of functional materials.

| Material/substrate | Process Parameters (Precursor, MF, Substrate temperature) | Key Features | Application | Ref. |
|---|---|---|---|---|
| Diamond/Si (111) | ($H_2$+$CH_4$; 98/2 sccm); dynamic magnetic field (DMF, ω = 83-600 π rad/s) | Enhanced nucleation density due to an induced EF excited by the DMF and electron-stimulated H desorption | - | 523 |
| Diamond/ rod-shaped tungsten carbide | ($H_2$+$CH_4$; 2000/10 sccm); ring magnet 400 mT; 800 °C | Simulation studies on MF distribution, ion movement, and deposition | - | 524 |
| Diamond/Si (100) | ($H_2$+$CH_4$; 99/1 vol.); Periodic MF (ω = 0-1 kHz); ~700 °C | (110) or (100) orientation favored with lower or higher ω | - | 525 |
| Nanostructured carbon films /Si | ($H_2$+$CH_4$) ~8 mT; ~700 °C | MF assistance in PECVD resulted in finer nanostructures with higher crystallinity | Electron field emission; MFCVD sample gave turn-on field 6.5 V·μm$^{-1}$ (vs. ~15.5 for zero-field) | 442 |
| Diamond film/ Si (100) | ($H_2$+$CH_4$); ~8 mT; -ve substrtae bias (0-40 mA current); ~700 °C | Combined EF- and MF-assisted control; film thickness varied with field | Electron field emission; MFCVD sample gave turn-on field 6.1 V·μm$^{-1}$ (vs. 11.2 for zero-field) | 31 |
| Diamond film/ Si | ($H_2$+$CH_4$); ~4 mT; ~808-872 °C | Use of a rotating MF; film thickness 7.41 μm (without MF 6.88 μm) | - | 526 |
| Branched or Fe-encapsulated carbon nanotubes/ Si | Iron(II) phthalocyanine+$H_2$; ~0.2 T (gradient 50 mT·cm$^{-1}$); 550°C | MF promoted the coalescence or division of catalyst particles, forming branched or encapsulated CNTs | - | 527 |
| DLC on YG8 carbide substrate | Cathode arc discharge (120 A DC), ($N_2$, Ar, $C_2H_2$), 0.9 Pa, 450 °C | Role of MF and bias controlled on structure and properties | Cutting tool protection film; coefficient of friction=0.112 | 91 |
| Carbon nanofibers (CNFs)/ Ni-deposited Cu | $C_2H_2$; 0-0.5 T; 700°C | CNFs changed to homogenized, narrower, bamboo-like CNTs with increasing MF | - | 528 |
| single-walled carbon nanotubes | 10 T | MF-assisted preferential growth of metallic single-walled CNTs (1-nm diameter) | - | 529 |
| a-C:H:$SiO_x$ film/ stainless steel | (polyphenylmethylsiloxane+ Ar); (0-1.7 mT) | Use of MF for enhancing plasma confinement in PECVD; elastic modulus increased from 90 to 117– 125 GPa | Tribological application; hardness increased from 8.7 to 11.7–12.5 GPa | 29 |
| Vertically standing graphene | (5-50 mT) | Use of MF for plasma confinement and vertical growth | $Na^+$ battery anode; capacity retention of 86% after 2000 cycles at 1 A g$^{-1}$ | 511 |
| Carbon nanotubes on LDH-catalyst | ($N_2$/$H_2$/$C_3H_6$ 70/40/40 ml min$^{-1}$); (~0.02 T); ~700 °C | MF affects catalyst arrangement, inducing higher yield, increased length and graphitic nature | - | 521 |
| Iron oxide/Si (100) | [Fe(O$^t$Bu)$_3$]$_2$; 0-0.5T perpendicular to substrate; 500 °C | Magnetite with increased particulate size in MFCVD, whereas (hematite + amorphous iron (III)oxide) in CVD | - | 530 |
| Iron on FTO or Si (100) | $Fe(CO)_5$; 0-1 T; 300 °C | Anisotropic columnar growth in MFCVD, isotropic grain growth in CVD | Water-splitting; J value was 0.027 and 0.050 mA cm$^{-2}$ for no field and MF film | 531 |
| α-$Fe_2O_3$/ FTO | $Fe(CO)_5$+20 sccm O2; 0-120 mT; | MF assistance in PECVD | Water-splitting; J value was 0.484 and 0.659 mA cm$^{-2}$ for no field and MF film | 532 |
| $UO_2$/ Si | U(O$^t$Bu)$_6$; 0-1 T; 400–1000 °C | Preferred ⟨111⟩ growth in CVD, polycrystalline growth in MFCVD | - | 533 |

Open Access Article. Published on 15 2025. Downloaded on 2025/6/3 7:37:30.
This article is licensed under a Creative Commons Attribution 3.0 Unported Licence.

Journal of Materials Chemistry A Accepted Manuscript



This journal is © The Royal Society of Chemistry 20xx

Please do not adjust margins

View Article Online
DOI: 10.1039/D5TA01081K

| | | | | |
|---|---|---|---|---|
| $TiO_2$/ Si | $TiCl_2(O^iPr)(pyridine)_3$; 0-0.5 T with (perpendicular/ parallel) field orientation; 300 °C | Well-defined anatase-type $TiO_6$ subunits in MFCVD, whereas rutile-type distorted $TiO_6$ units in CVD | - | 534 |
| $MgFe_2O_4$ films | $MgFe_2(O^tBu)_8$; 0-1 T; 300 °C | MF induces higher grain growth and densification, influencing the magnetic domains and inversion of crystal lattice | - | 535 |
| ReN films/Si | [*fac*-Re(I)$(CO)_3$(L)]; 0-1 T; 600 °C | Preferred growth along ⟨100⟩ direction in MFCVD | - | 536 |

a-C:H:$SiO_x$- $SiO_x$ doped amorphous hydrogenated carbon ; J= photocurrent density; L=(*N*,*N*-(4,4,4-trifluorobut-1-en-3-on)-dimethyl propylene diamine; LDHs- FeMgAl layered double hydroxides;

Researchers also employed external MF to influence the normal CVD processes for the deposition of numerous functional materials. For example, metal catalysts used for the growth of CNTs, are influenced by the application of magnetic field, thus altering the growth mechanism. During MFCVD of Fe-encapsulated CNT, Wei et al.[527] observed that an MF (0.2 T with a gradient of ~50 mT $cm^{-1}$) transverse to the growth direction resulted in the growth of branched CNTs having Fe particles at its base, whereas an MF parallel to the growth direction led to less-branched Fe-encapsulated CNTs. Similarly, the CVD of carbon nanofibers over Ni catalyst led to random nanofibers with entangled orientation, but an external MF assistance led to an aligned growth perpendicular to the substrate.[528] Interestingly, with increasing field strength (up to 0.5 T) the morphology changed from disordered solid-cored nanofibers to bamboo-like CNTs. A growth mechanism based on the particle size of the catalyst, which decreased with increasing magnetic field and the diamagnetic nature of carbon atoms, was proposed to explain the morphological variations in CNFs with the field strength. A similar growth mechanism, induced by an ordered arrangement of magnetic FeMgAl layered double hydroxides catalyst flakes in an MF-assisted fluidized bed CVD, resulted in a higher yield of bundles of longer, narrower, and highly graphitic CNTs.[521]

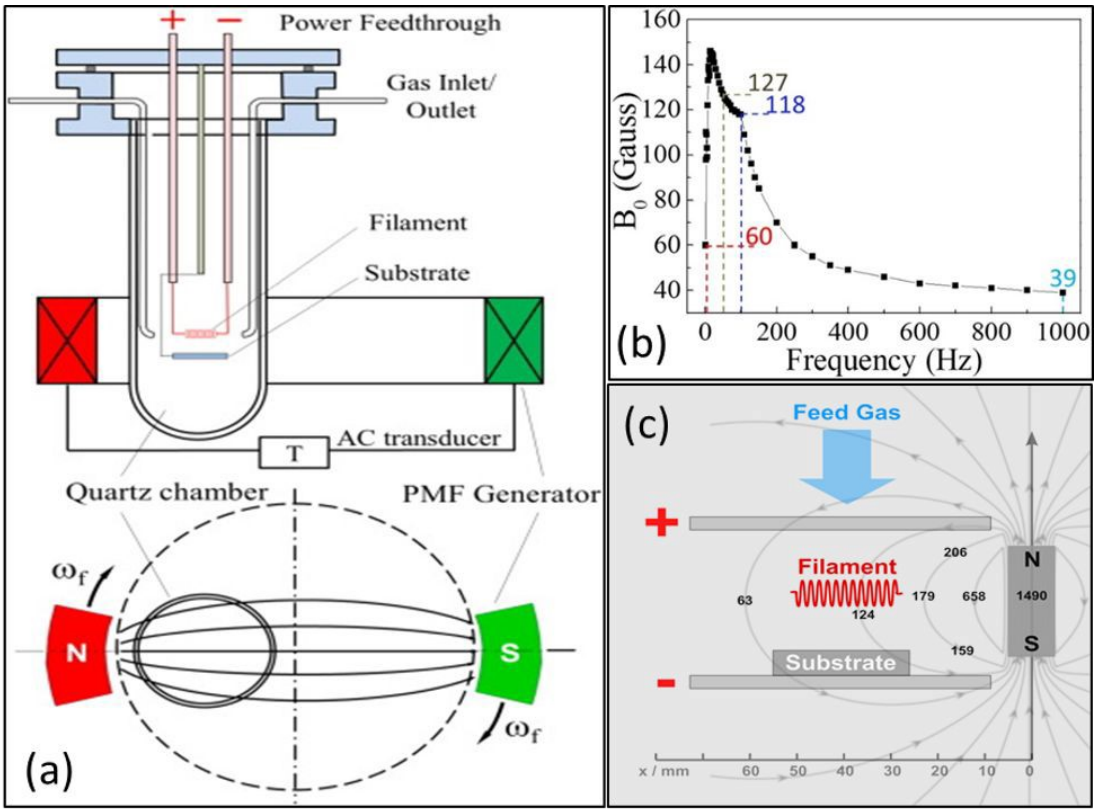


*Fig. 8 (a) Schematic diagram of a periodic MF-assisted HFCVD system and (b) The measured relationship between $B_0$ and angular frequencies, Reused with permission from Elsevier[525]. (c) A schematic displaying the distribution of MF strength in magnetic and electric fields coupled HFCVD. The numerical values in figures are taken from the work of Wang et al.[31] and represent the Gaussian value of the MF strength.*

Magnetic field assistance has played a key role in enabling the growth of diamond at relatively low temperatures and low pressures in catalytic HFCVD.[537–539] Based on the atomic scale dynamics and electronic spin effects for carbon rehybridization and fixation, Little and Goddard[537] demonstrated the influence of a static MF over the nucleation and growth mechanism of diamond. A strong MF (~19.3 T) was capable of initiating the nucleation, thus eliminating the requirement of chemical or

Open Access Article. Published on 15 2025. Downloaded on 2025/6/3 7:37:30. This article is licensed under a Creative Commons Attribution 3.0 Unported Licence.

Journal of Materials Chemistry A Accepted Manuscript



Please do not adjust margins

View Article Online
DOI: 10.1039/D5TA01081K

Open Access Article. Published on 15 2025. Downloaded on 2025/6/3 7:37:30.
This article is licensed under a Creative Commons Attribution 3.0 Unported Licence.

Journal of Materials Chemistry A Accepted Manuscript

abraded nucleation centers.[537] The constriction effect induced by Lorentz force of the static MF increased the effective concentration of electrons and polarized hydrocarbon species in reactive gas mixture by minimizing their collisions with the reactor walls.[539] In a periodic MF (with magnetic field strength $B = B_0 \sin \omega_f t$, where $B_0$ is maximum field strength and $\omega_f$ is angular frequency, Fig. 8 (a)), the concentration of active carbon particles increased with increasing $\omega_f$, resulting in enhanced nucleation density and diminished crystal size. Due to the rotation of magnetic lines in a periodic field, the electrons and polarized hydrocarbon species prolong their moving path, leading to a higher probability of collision with reaction gas molecules to produce more carbon precursors.[539]. However, based on the intricate relationship between $B_0$ and vibrational frequency of spiral movement, it is proposed that the positive effect of increasing $\omega_f$ on prolonging the moving path of particles becomes negative beyond a $\omega_f$ value (Fig. 8 (b)).[525,539]

As diamond films are known for their orientation-dependent functional properties, Wang et al.[525] demonstrated that depending upon lower or higher $\omega_f$ values the MF-assisted HFCVD grown diamond film preferred (110) or (100) orientation, respectively. Using methane and hydrogen (1/99 vol%) gas mixture, the molar ratio of $C_2H_2$ and $CH_3$ fragments ($C_{[C_2H_2]}/C_{[CH_3]}$) in reactive gas mixture influenced the orientation of diamond film. The C–H bond dissociation energy in $CH_3$ (462 kJ mol$^{-1}$) is lower than that in $C_2H_2$ (556 kJ mol$^{-1}$), indicating an easier dehydrogenation of $CH_3$ than $C_2H_2$. The rising collision possibility with increasing $\omega_f$ raised the $C_{[C_2H_2]}$ more rapidly compared to the $C_{[CH_3]}$, resulting in a higher $C_{[C_2H_2]}/C_{[CH_3]}$ ratio that favored the (100) orientation over (110) orientation. Also, higher $\omega_f$ values resulted in continuous nano-diamond films with fine grains, displaying an improved field emission performance.[539]

In a related study, Wang et al. [31] investigated the effect of the coupled magnetic and electric field on the growth of diamond film, presenting a qualitative simulation of the moving paths of particles in the coupled fields with different electric field intensities, direction of initial velocity, and charge-to-mass ratio (Fig. 8 (c)). The experimental results indicated that the coupled fields enhanced the graphitization and refinement of diamond crystals. The simulation study pointed out that MF suppressed the (100) orientation by changing the precursor distribution, influencing the ratio of two precursor fragments- $C_2H_2$ and $CH_3$, a key factor deciding the preferred orientation of the as-prepared film.

Liu et al.[540] investigated the effect of a dynamic MF (where the induced EF points alternately in the ±z directions, orthogonal to the substrate surface[523]) with different angular frequencies on the growth rate, diamond quality, growth orientation, and deposition uniformity. At higher angular frequencies, the electrons move with a higher velocity and a larger radius, leading to an increased range of electron motion. With this, the electron-molecule collisional excitations are intensified, enabling more activated molecules to participate in growth and enhance the growth rate.[540] Additionally, similar to the EF-assisted bias-enhanced nucleation[90,419,420], a dynamic MF drives electrons and ions to enhance the diamond nucleation. However, it does not cause a persistent bombardment of charged particles to the diamond growth front, which otherwise causes graphitization. Thus, a dynamic MF suppressed the $sp^2$ carbon generation and improved the diamond quality.[540] Presenting a detailed investigation of the effect of dynamic MF on diamond growth, Liu et al.[523] demonstrated that the dynamic MF-induced EF alternately pointed in the ±z directions, driving the electrons to continuously oscillate during motion and leading to non-persistent bombarding at the substrate surface.[523] As a result, the dynamic MF-induced diamond nucleation has an entirely different surface chemistry compared to the EF bias-assisted nucleation. As the thermal energy of hot filament was well below the energy required to generate atomic H and $CH_3$ components via gas phase electron–molecule collisions, the gas phase electron–molecule collision excitation could not support the enhancement of diamond nucleation in CVD. The nucleation density (calculated from SEM images) displayed a dependence on ω (Fig. 9 (a)) and the Fourier-transformed infrared spectroscopy (FTIR) of the MF-assisted HFCVD film displayed strong peaks at 1750 and 2240–2400 cm$^{-1}$ (Fig. 9 (b)), indicating a highly activated film surface. Therefore, the authors proposed that dynamic MF mainly influenced the surface chemistry rather than the gas chemistry. The enhancement was attributed to a dynamic MF-induced EF, leading to the electron-stimulated desorption of hydrogen and formation of carbon dangling bonds on the growth front, which subsequently morphed into mono-radical and bi-radical sites for enhanced diamond nucleation (Fig. 9 (c)).

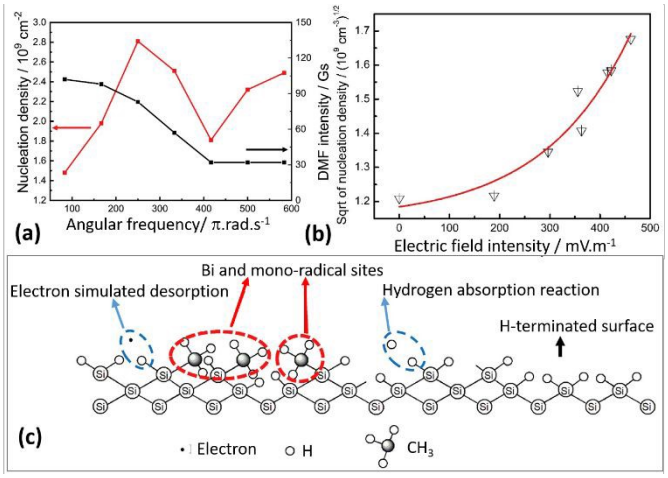


*Fig. 9. (a) Dynamic MF intensity and diamond nucleation density as a function of angular frequencies; (b) Square root of diamond nucleation density fitted (red curve) as a function of the induced electric field; and (c) Schematic diagram of diamond growth front and hydrogen desorption, Adopted with permission from Elsevier.*[523]

Magnetic field-assisted CVD has been also employed for the deposition of numerous non-carbonaceous materials, such as metalloids and metal oxides. For example, in PECVD of hydrogenated microcrystalline silicon (μc-Si:H) thin films, Kim et al.[541] observed that an MF assist using a geometrically aligned magnetic mirror resulted in a 7-fold increase in deposition rate and enhanced crystallinity. This was attributed to the increased

 This journal is © The Royal Society of Chemistry 20xx

Please do not adjust margins

formation of Si and SiH radicals from $SiH_4$ precursor under MF-induced enhanced plasma confinement, as observed in the analysis of plasma properties using optical emission spectroscopy.

For magnetically active materials, the application of MF during CVD influences not only the deposition and growth process but also the orientation of grains and other field effects.[542] Mathur and coworkers have extensively used MF-assisted manipulation in the CVD of magnetically active materials.[530–536,543] For example, PECVD of hematite film using iron pentacarbonyl precursor displayed excellent MF-assisted control on phase and surface properties in static MF generated by different arrangements (parallel/perpendicular; par/perp) of rod-type or disk-type magnets (RTMs or DTMs) along the substrate (Fig. 10 (a)-(f)).[532] In crystallographic analysis, the zero field and RTM-perp samples experienced preferred growth along (110) crystallographic plane, whereas the RTM-par sample, along with the DTM-par and DTM-perp samples, experienced preferred growth along (104) plane (Fig. 10 (g)-(h)). Compared to zero field deposition, field-assisted depositions resulted in a more homogeneous particle shape and size, forming a denser microstructure (Fig. 10 (i)-(n)). The films deposited under DTM-perp arrangement creating an overall attractive field interaction exhibited larger aggregates with fewer grain boundaries (Fig. 10 (j)). The films deposited under DTM-par arrangement creating an overall repulsive interaction exhibited more aggregates of densified crystallites (Fig. 10 (k)). However, the films deposited under DTM-perp and DTM-par arrangements displayed no difference in crystallite sizes. More importantly, the hematite film prepared under MF-assistance displayed significant enhancement in photoelectrochemical properties in water splitting, which was attributed to the presence of smooth particle surfaces and fewer grain boundaries in field-assisted growth, favoring charge transportation and reduced charge recombination.

Open Access Article. Published on 15 2025. Downloaded on 2025/6/3 7:37:30.
This article is licensed under a Creative Commons Attribution 3.0 Unported Licence.

Journal of Materials Chemistry A Accepted Manuscript

View Article Online
DOI: 10.1039/D5TA01081K

ARTICLE

Open Access Article. Published on 15 2025. Downloaded on 2025/6/3 7:37:30.
This article is licensed under a Creative Commons Attribution 3.0 Unported Licence.

Journal of Materials Chemistry A Accepted Manuscript

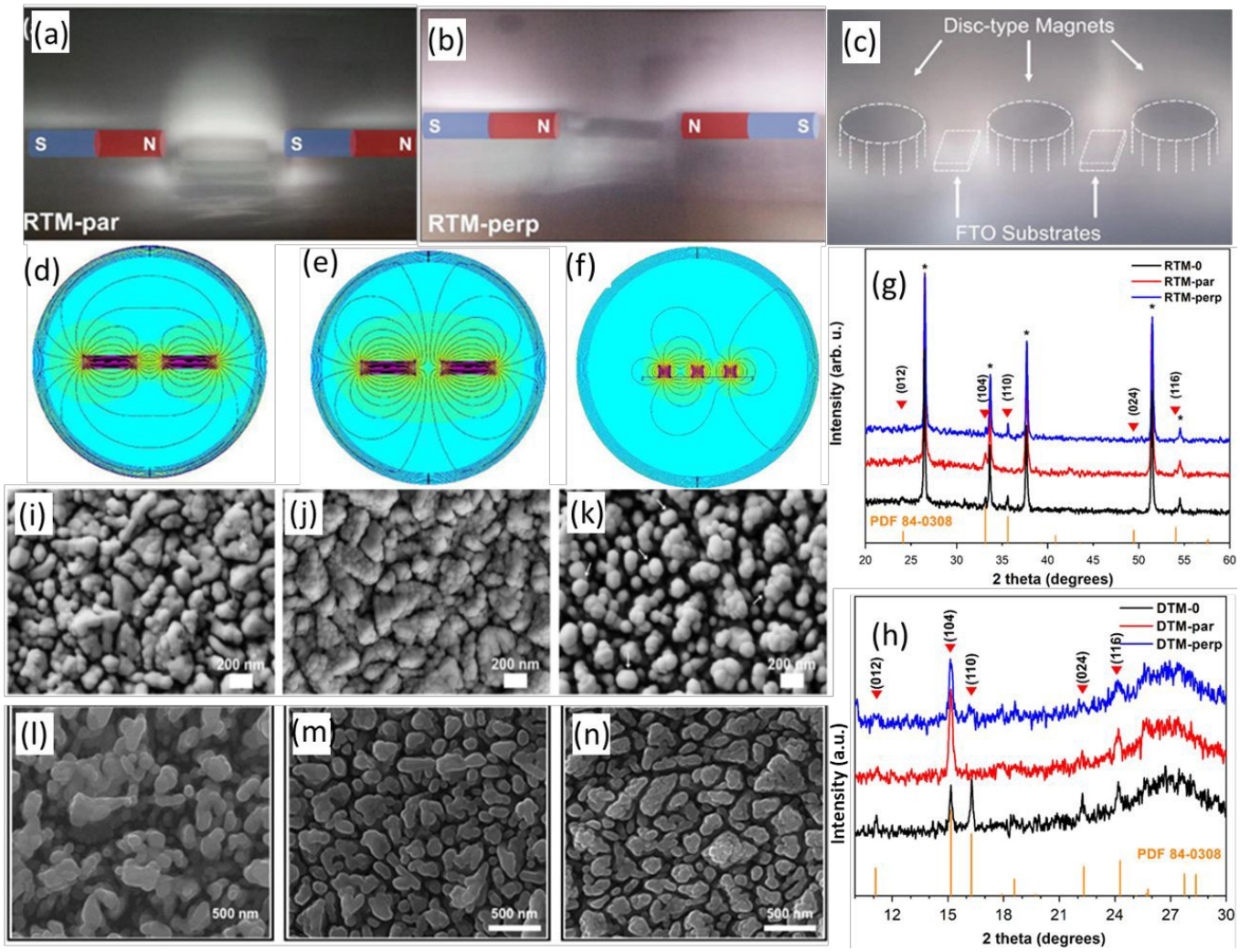


*Fig. 10. Photographs of plasma under (a) parallel and (b) perpendicular field geometry and corresponding qualitative magnetic field profiles (d) and (e) for RTMs; Photographs of plasma (c) and corresponding qualitative magnetic field profile (f) for arrangement of DTMs; XRD patterns of the hematite films deposited under different MFs. Asterisks (*) represent $SnO_2$ from FTO substrates (g)-(h); Surface morphologies of deposition using RTM under (i) zero field, (j) parallel field, and (k) perpendicular field; Surface morphologies of deposition using DTM under (l) zero field, (m) parallel field, and (n) perpendicular field, Adopted with permission from Wiley.*[532]

The MFCVD of hematite on F-doped $SnO_2$ and Si(100) substrates displayed substrate-independent anisotropic growth of α-$Fe_2O_3$ columns, as against an isotropic grain growth in zero field deposition.[533] Moreover, a parallel field resulted in larger crystallites with cuboidal morphology, whereas a 45° inclination led to a tilted orientation of anisotropic grains. The TEM analysis displayed a gradual increase in average crystallite size with increasing field strength, supporting the observation that even under low MF strength, the interactions between the crystalline nuclei and MF can greatly influence the nucleation and grain growth on the substrate.[31,530,536]

Mathur and coworkers further broadened the horizon of MFCVD by using a paramagnetic metalorganic Ti(III) precursor [$TiCl_2(O^iPr)(pyridine)_3$] for the deposition of $TiO_2$ films,

View Article Online
DOI: 10.1039/D5TA01081K

demonstrating a remarkable shape anisotropy in deposited films.[534] The MF-assisted (B=0.5 T) deposition resulted in the growth of well-defined anatase-type $TiO_6$ subunits, whereas zero-field deposition led to distorted rutile-type $TiO_6$ subunits. The zero-field deposition displayed preferential growth along (200) plane, whereas the MFCVD resulted in preferential growth along (101) and (200) planes in perpendicular-field and parallel-field orientations, respectively. Elaborating on the MF-matter interaction, similar experiments performed using a diamagnetic precursor $Ti(O^iPr)_4$ indicated no such field-dependent microstructural variations, highlighting the importance of $d^1$ electronic configuration in triggering the MF-matter interaction. However, noticeably, irrespective of the field strength and orientation, the MFCVD with paramagnetic precursors resulted in diamagnetic $TiO_2$ films.[534]

MFCVD has displayed similar variations in shape, morphology, and crystallographic orientation during <1.0 T MF-assisted CVD of rhenium nitride,[536] $UO_2$,[531] and $MgFe_2O_4$[535]. Interestingly, although MF-assist has invariably increased the nucleation and growth and has a homogenization effect on shape, particle size distribution, and composition, it has exerted a varying influence on particle size evolution, depending upon the MF orientations and magnetic behavior of participating and resulting species. More precisely, except for $UO_2$[531] and $YBa_2Cu_3O_7$ films[509], the MF assistance led to increased particle size in CVD of magnetite,[530] hematite,[532] $TiO_2$,[534] rhenium nitride,[536] and $MgFe_2O_4$[535]. This was explained based on the induced internal magnetic field inside the growing diamagnetic $UO_2$ and $YBa_2Cu_3O_7$ being antiparallel to the applied external MF, creating an energetically unfavorable situation for grain growth.[509] Notwithstanding, in case of $YBa_2Cu_3O_7$ a low MF (≤2.0 T) caused a decrease in grain size compared to the zero field, but at higher MF (≥4.0 T) the grain size increased, due to the change in growth mode—from being 2D at low MF to 3D at higher MF,[509] and most likely due to, in our opinion, a high MF field overcoming the internal diamagnetic field effect.

### 5.3 Perspective on magnetic field-assisted CVD

Over the years, numerous results have strengthened the utility of external MF in inducing a profound influence on the nucleation, grain growth, phase composition, and crystallographic orientation during CVD, thus altering the morphology, chemical topography, and functional properties of the resulting films. Therefore, it is expected to increasingly become a preferred pathway, compared to conventional experimental controls- temperature, and pressure or precursor chemistry, for *in situ* manipulation of the material properties of the CVD-grown films. Magnetic fields with spatial and temporal variations such as periodic, dynamic, or rotating configurations have shown significant potential in influencing nucleation and growth mechanisms during CVD. However, such approaches have mostly been limited to the deposition of diamond materials and their application to other material systems remains underexplored. Most reports on magnetic field-assisted CVD are limited to lab-scale set-ups with small-area deposition. A key challenge lies in generating strong and uniform magnetic fields over larger deposition areas. This limitation is reflected in the fact that most MFCVD studies have employed magnetic field strengths of ≤1 T. New CVD setup designs capable of accommodating even stronger magnetic fields (≥5 T) carry the potential to broaden the scope of MFCVD enabling field-assisted control over growth kinetics and materials properties. Nevertheless, the integration of strong magnets brings added instrumentation complexity, cost, and technical expertise requirements, which must be carefully considered for practical scalability.

Most MF-matter interaction studies in CVD so far have focused mainly on the precursor-MF interactions, and the interaction of MF with carrier gas and substrate[533,544,545] is less explored. Moreover, the interaction of MF with temperature, an important process control parameter, has been less precisely monitored and understood, especially in the case of magnetically active precursor and deposited materials. The influence of external MF in those CVD processes where paramagnetic oxygen is used as a reactant/carrier gas [546] is less exploited. Most importantly, the field of MFCVD lacks sufficient mathematical models and simulation studies relating the effects of external magnetic fields with the CVD growth parameters.

## 6. Concluding remarks

Field-assisted chemical vapor deposition (CVD) represents a promising future direction for controlling thin-film growth, with precise control over film properties and microstructure. This technique involves applying external fields, such as magnetic or electric fields, during the CVD process to influence the deposition dynamics, leading to novel material characteristics and improved process efficiency. The various field-assisted modulations in CVD have emerged as a powerful additional control method, often operating independently of precursor chemistry influence and thermodynamic parameters. These modulations have enabled significant advancements in growth control, microstructure tuning, and material properties for targeted applications.

This review underscores the importance of non-conventional process parameters in CVD and highlights their impact on material synthesis. Additionally, it addresses key limitations, particularly the lack of theoretical studies that could provide deeper insights into the role of these modulators in CVD nucleation and growth. Understanding their effects on microstructure, composition, and functional properties remains a crucial challenge. In particular, the emerging field of magnetic-field-assisted CVD would benefit from further research, enabling reliable control over the process and material characteristics.

According to current estimates, the global CVD market has reached approximately 24 billion USD and is projected to grow to nearly 48 billion USD by 2032.[547] Field-assisted manipulations are expected to play a key role in capitalizing on this trend, however, the existing challenges, as schematically highlighted in Fig. 11, need to be effectively addressed to unfold the potential of field-enhanced CVD techniques. Key advancements will likely involve optimizing field modulations in terms of

Open Access Article. Published on 15 2025. Downloaded on 2025/6/3 7:37:30.
This article is licensed under a Creative Commons Attribution 3.0 Unported Licence.

Journal of Materials Chemistry A Accepted Manuscript



Please do not adjust margins

View Article Online
DOI: 10.1039/D5TA01084K

intensity and configuration and innovations in reactor design to accommodate such modulations in high-throughput systems. Additionally, advancing our understanding of field-matter interactions, coupled with extensive computational analysis using 3D reactor-scale models, will be crucial for overcoming current limitations. Finally, the integration of operando and in situ techniques into conventional CVD systems and processes to develop a robust framework for depositing materials with enhanced functional properties can bring a paradigm shift in thin film engineering.

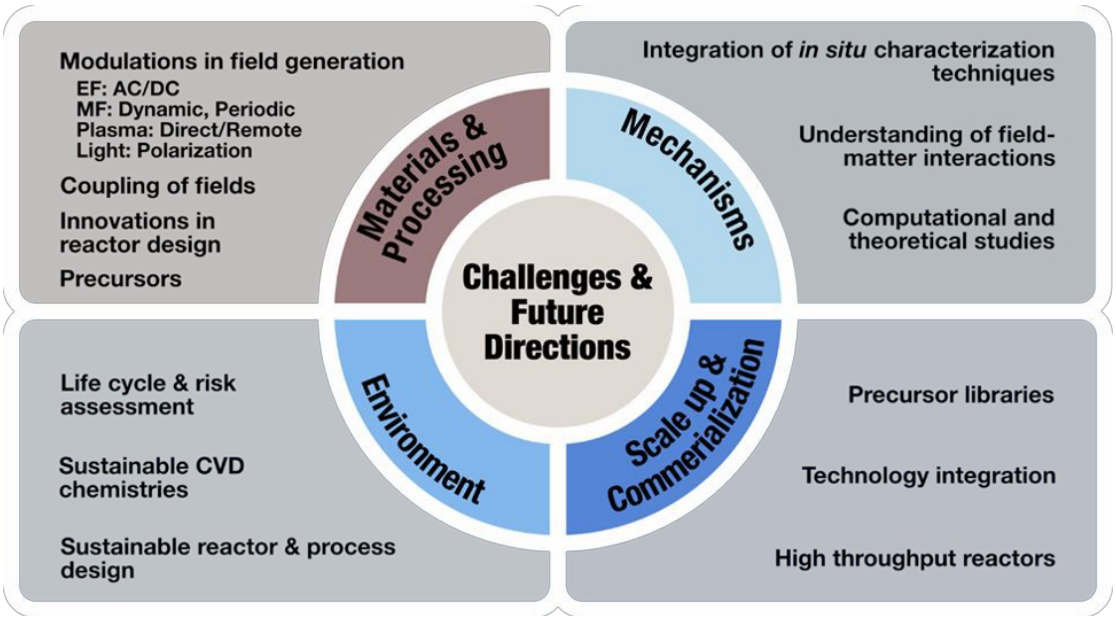


*Fig. 11. Schematic of existing challenges in field-assisted CVD and the future directions to overcome them.*

## Author contributions

All authors contributed equally.

## Conflicts of interest

There are no conflicts of interest to declare.

## Data availability

No primary research results, software or code have been included and no new data were generated or analysed as part of this review.

## Acknowledgements

Authors gratefully thank the University of Cologne for the infrastructural and financial support. SM acknowledges the financial support by the German Science Foundation (DFG) in the frame of the priority program SPP 1959 "Manipulation of matter controlled by electric and magnetic field: Towards novel synthesis and processing routes of inorganic materials".

## Notes and references

1 B. Sun, J. Pang, Q. Cheng, S. Zhang, Y. Li, C. Zhang, D. Sun, B. Ibarlucea, Y. Li, D. Chen, H. Fan, Q. Han, M. Chao, H. Liu, J. Wang, G. Cuniberti, L. Han and W. Zhou, *Advanced Materials Technologies*, 2021, **6**, 2000744.
2 L. Sun, G. Yuan, L. Gao, J. Yang, M. Chhowalla, M. H. Gharahcheshmeh, K. K. Gleason, Y. S. Choi, B. H. Hong and Z. Liu, *Nat Rev Methods Primers*, 2021, **1**, 1–20.
3 M. Nakaya, A. Uedono and A. Hotta, *Coatings*, 2015, **5**, 987–1001.
4 M. Bahri, S. H. Gebre, M. A. Elaguech, F. T. Dajan, M. G. Sendeku, C. Tlili and D. Wang, *Coordination Chemistry Reviews*, 2023, **475**, 214910.
5 L. Wang, G. Sun and S. Yuan, *Advanced Materials Technologies*, 2024, **9**, 2301973.
6 J. Zhang, J. Wang, G. Zhang, Z. Huo, Z. Huang and L. Wu, *Materials & Design*, 2024, **237**, 112577.
7 M. Yaseen, M. A. K. Khattak, A. Khan, S. Bibi, M. Bououdina, M. Usman, N. A. Khan, A. A. A. Pirzado, R. A. Abumousa and M. Humayun, *Nanocomposites*, 2024, **10**, 1–40.
8 L. Tang, J. Tan, H. Nong, B. Liu and H.-M. Cheng, *Acc. Mater. Res.*, 2021, **2**, 36–47.

Open Access Article. Published on 15 2025. Downloaded on 2025/6/3 7:37:30.
This article is licensed under a Creative Commons Attribution 3.0 Unported Licence.

Journal of Materials Chemistry A Accepted Manuscript



This journal is © The Royal Society of Chemistry 20xx

Please do not adjust margins

9 M. D. Straub, J. Leduc, M. Frank, A. Raauf, T. D. Lohrey, S. G. Minasian, S. Mathur and J. Arnold, *Angewandte Chemie International Edition*, 2019, **58**, 5749–5753.
10 U. Atamtürk, E. Jung, T. Fischer and S. Mathur, *Chem. Mater.*, 2022, **34**, 7344–7356.
11 C. K. Amadi, T. Karimpour, M. Jafari, Z. Peng, D. V. Gerven, V. Brune, F. Hartl, M. Siaj and S. Mathur, *Dalton Trans.*, 2024, **53**, 9874–9886.
12 A. Sutorius, R. Weißing, C. R. Pèrez, T. Fischer, F. Hartl, N. Basu, H. Suk Shin and S. Mathur, *Nanoscale*, 2024, **16**, 15782–15792.
13 V. Brune, C. Hegemann and S. Mathur, *Inorg. Chem.*, 2019, **58**, 9922–9934.
14 B. Qin, H. Ma, M. Hossain, M. Zhong, Q. Xia, B. Li and X. Duan, *Chem. Mater.*, 2020, **32**, 10321–10347.
15 Y. Hamedani, P. Macha, T. J. Bunning, R. R. Naik, M. C. Vasudev, Y. Hamedani, P. Macha, T. J. Bunning, R. R. Naik and M. C. Vasudev, in *Chemical Vapor Deposition - Recent Advances and Applications in Optical, Solar Cells and Solid State Devices*, IntechOpen, 2016.
16 F. Loyer, S. Bulou, P. Choquet and N. D. Boscher, *Plasma Processes and Polymers*, 2018, **15**, 1800121.
17 G. Franz, *Processes*, 2021, **9**, 980.
18 H. Kun, J. Li, K. Li, N. Yan, C. bian, Y. Guan, Y. Yang and H. Li, *Polymer Degradation and Stability*, 2022, **196**, 109816.
19 R. Panickar, C. B. Sobhan and S. Chakravorti, *Vacuum*, 2020, **172**, 109108.
20 M. Bi, J. Zhu, Y. Luo, H. Cai, X. Li, X. Wang, Y. Wei, X. Wang, C. Hu, J. Hu, G. Zhang, X. Wang and X. Zhang, *Coatings*, 2022, **12**, 1731.
21 K. Alberi and M. A. Scarpulla, *J. Phys. D: Appl. Phys.*, 2017, **51**, 023001.
22 X. Zhao, C. Wei, Z. Gai, S. Yu and X. Ren, *Chem. Pap.*, 2020, **74**, 767–778.
23 M. E. A. Warwick, A. J. Roberts, R. C. T. Slade and R. Binions, *J. Mater. Chem. A*, 2014, **2**, 6115–6120.
24 A. Sawabe and T. Inuzuka, *Applied Physics Letters*, 1985, **46**, 146–147.
25 S. Yugo, T. Kimura and T. Muto, *Vacuum*, 1990, **41**, 1364–1367.
26 J. Li, Y. Wang, Q. Wei, Y. Xie, H. Long, Z. Deng, L. Ma, Z. Yu, Y. Jiang, N. Hu and K. Zhou, *Surface and Coatings Technology*, 2017, **324**, 413–418.
27 Y. Wang, Q. Wei, Z. Yu, H. Long, Z. Deng, Y. Xie, J. Li, C.-T. Lin, L. Ma and K. Zhou, *Applied Surface Science*, 2017, **423**, 788–792.
28 W. In-Hwang, X. Chen, T. Kuzuya, K. Kawabe and S. Motojima, *Carbon*, 2000, **38**, 565–571.
29 A. S. Grenadyorov, A. A. Solovyev, K. V. Oskomov and V. O. Oskirko, *Journal of Vacuum Science & Technology A*, 2019, **37**, 061512.
30 T. Tabuchi, M. Takashiri and K. Ishida, *Surface and Coatings Technology*, 2007, **202**, 114–120.
31 Y. Wang, J. Li, N. Hu, Y. Jiang, Q. Wei, Z. Yu, H. Long, H. Zhu, Y. Xie, L. Ma, C.-T. Lin and W. Su, *Mater. Res. Express*, 2018, **5**, 035009.
32 X. Lu, P. J. Bruggeman, S. Reuter, G. Naidis, A. Bogaerts, M. Laroussi, M. Keidar, E. Robert, J.-M. Pouvesle, D. Liu and K. (Ken) Ostrikov, *Front. Phys.*, DOI:10.3389/fphy.2022.1040658.
33 A. Fridman, Ed., in *Plasma Chemistry*, Cambridge University Press, Cambridge, 2008, pp. 12–91.
34 I. B. Denysenko, S. V. Ivko and N. A. Azarenkov, in *2018 IEEE 8th International Conference Nanomaterials: Application & Properties (NAP)*, 2018, pp. 1–5.
35 L. Martinu, O. Zabeida and J. E. Klemberg-Sapieha, in *Handbook of Deposition Technologies for Films and Coatings (Third Edition)*, ed. P. M. Martin, William Andrew Publishing, Boston, 2010, pp. 392–465.
36 S. Sovizi, S. Angizi, S. A. Ahmad Alem, R. Goodarzi, M. R. R. Taji Boyuk, H. Ghanbari, R. Szoszkiewicz, A. Simchi and P. Kruse, *Chem. Rev.*, 2023, **123**, 13869–13951.
37 C. Vallée, M. Bonvalot, S. Belahcen, T. Yeghoyan, M. Jaffal, R. Vallat, A. Chaker, G. Lefèvre, S. David, A. Bsiesy, N. Possémé, R. Gassilloud and A. Granier, *Journal of Vacuum Science & Technology A*, 2020, **38**, 033007.
38 J. Chen, Z. Bo and G. Lu, in *Vertically-Oriented Graphene: PECVD Synthesis and Applications*, eds. J. Chen, Z. Bo and G. Lu, Springer International Publishing, Cham, 2015, pp. 19–34.
39 J. Zhou, J. Liao, J. Huang, T. Chen, B. Lv and Y. Peng, *Vacuum*, 2022, **195**, 110678.
40 M. Yamamoto, H. Murata, N. Miyata, H. Takashima, M. Nagao, H. Mimura, Y. Neo and K. Murakami, *ACS Omega*, 2023, **8**, 5497–5505.
41 J. Chen, P. Ji, Y. Yang, C. Jin, L. Zhuge and X. Wu, *Diamond and Related Materials*, 2021, **112**, 108243.
42 J. Chen, P. Ji, Y. Yang, C. Jin, L. Zhuge and X. Wu, *Thin Solid Films*, 2020, **709**, 138167.
43 J. Wang, P. Bulkin, I. Florea, J.-L. Maurice and E. Johnson, *J. Phys. D: Appl. Phys.*, 2016, **49**, 285203.


Open Access Article. Published on 15 2025. Downloaded on 2025/6/3 7:37:30.
This article is licensed under a Creative Commons Attribution 3.0 Unported Licence.

Journal of Materials Chemistry A Accepted Manuscript

44 S. Lin, D. Xie, Y. Tang, Y. Wang, F. Jing, N. Huang and Y. Leng, *Vacuum*, 2021, **189**, 110223.
45 P. Mandracci and P. Rivolo, *Coatings*, 2023, **13**, 1075.
46 N. M. Santhosh, G. Filipič, E. Tatarova, O. Baranov, H. Kondo, M. Sekine, M. Hori, K. (Ken) Ostrikov and U. Cvelbar, *Micromachines*, 2018, **9**, 565.
47 R. Snyders, D. Hegemann, D. Thiry, O. Zabeida, J. Klemberg-Sapieha and L. Martinu, *Plasma Sources Sci. Technol.*, 2023, **32**, 074001.
48 Y. Hua, J. Song, Z. Hao, G. Zhang and C. Ren, *Plasma Res. Express*, 2018, **1**, 015008.
49 K. Yi, D. Liu, X. Chen, J. Yang, D. Wei, Y. Liu and D. Wei, *Acc. Chem. Res.*, 2021, **54**, 1011–1022.
50 V. Cech and M. Branecky, *Plasma Processes and Polymers*, 2023, **20**, 2300019.
51 G. S. Oehrlein and S. Hamaguchi, *Plasma Sources Sci. Technol.*, 2018, **27**, 023001.
52 D. W. Hess, *Annu. Rev. Mater. Sci.*, 1986, **16**, 163–183.
53 S. Mathur and T. Ruegamer, *International Journal of Applied Ceramic Technology*, 2011, **8**, 1050–1058.
54 L. Czympiel, M. Frank, A. Mettenbörger, S.-M. Hühne and S. Mathur, *Comptes Rendus Chimie*, 2018, **21**, 943–951.
55 A. S. M. de Freitas, C. C. Maciel, J. S. Rodrigues, R. P. Ribeiro, A. O. Delgado-Silva and E. C. Rangel, *Vacuum*, 2021, **194**, 110556.
56 M. Li, D. Liu, D. Wei, X. Song, D. Wei and A. T. S. Wee, *Advanced Science*, 2016, **3**, 1600003.
57 N.-C. Yeh, C.-C. Hsu, J. Bagley and W.-S. Tseng, *Nanotechnology*, 2019, **30**, 162001.
58 E. Bertran-Serra, S. Rodriguez-Miguel, Z. Li, Y. Ma, G. Farid, S. Chaitoglou, R. Amade, R. Ospina and J.-L. Andújar, *Nanomaterials*, 2023, **13**, 2533.
59 G. L. Kabongo, B. M. Mothudi and M. S. Dhlamini, *Front. Mater.*, DOI:10.3389/fmats.2021.762030.
60 K. Ollegott, P. Wirth, C. Oberste-Beulmann, P. Awakowicz and M. Muhler, *Chemie Ingenieur Technik*, 2020, **92**, 1542–1558.
61 H. Nagasawa and T. Tsuru, in *Advanced Materials for Membrane Fabrication and Modification*, CRC Press, 2018.
62 D. Patrun, S. Zhao, Z. Aytuna, T. Fischer, M. Miess, Z. Hong and S. Mathur, *Nano Energy*, 2024, **128**, 109836.
63 M. Pyeon, T.-P. Ruoko, J. Leduc, Y. Gönüllü, M. Deo, N. V. Tkachenko and S. Mathur, *Journal of Materials Research*, 2018, **33**, 455–466.
64 L. Jürgensen, M. Frank, M. Pyeon, L. Czympiel and S. Mathur, *Organometallics*, 2017, **36**, 2331–2337.
65 R. Garg, N. Rajagopalan, M. Pyeon, Y. Gönüllü, T. Fischer, A. S. Khanna and S. Mathur, *Surface and Coatings Technology*, 2018, **356**, 49–55.
66 L. Jürgensen, D. Höll, M. Frank, T. Ludwig, D. Graf, A. Katrin Schmidt-Verma, A. Raauf, I. Gessner and S. Mathur, *Dalton Transactions*, 2020, **49**, 13317–13325.
67 F. Zhou, J. Shan, L. Cui, Y. Qi, J. Hu, Y. Zhang and Z. Liu, *Advanced Functional Materials*, 2022, **32**, 2202026.
68 F. Sanchette, M. El Garah, S. Achache, F. Schuster, C. Chouquet, C. Ducros and A. Billard, *Coatings*, 2021, **11**, 1225.
69 J. Li and H. Chae, *Korean J. Chem. Eng.*, 2023, **40**, 1268–1276.
70 Y. Liu, J. He, N. Zhang, W. Zhang, Y. Zhou and K. Huang, *J Mater Sci*, 2021, **56**, 12559–12583.
71 S. V. Baryshev and M. Muehle, *IEEE Transactions on Plasma Science*, 2024, **52**, 1082–1103.
72 N. Chen, D. H. Kim, P. Kovacik, H. Sojoudi, M. Wang and K. K. Gleason, *Annual Review of Chemical and Biomolecular Engineering*, 2016, **7**, 373–393.
73 Z. Yang, Y. Liu, Z. Guo, J. Wei, J. Liu, L. Chen and C. Li, *Diamond and Related Materials*, 2024, **142**, 110767.
74 C.-W. Chuang and F. C.-N. Hong, *Crystal Growth & Design*, 2023, **23**, 37–48.
75 F. Movassagh-Alanagh, A. Abdollah-Zadeh, M. A. Zolbin, N. Nemati and R. Aghababaei, *Tribology International*, 2023, **179**, 108137.
76 O.-G. Simionescu, O. Brîncoveanu, C. Romaniţan, S. Vulpe and A. Avram, *Coatings*, 2022, **12**, 943.
77 G. Moradkhani, J. Profili, M. Robert, G. Laroche, S. Elkoun and F. Mighri, *Polymers*, 2024, **16**, 360.
78 A. D. Nguyen, T. K. Nguyen, C. T. Le, S. Kim, F. Ullah, Y. Lee, S. Lee, K. Kim, D. Lee, S. Park, J.-S. Bae, J. I. Jang and Y. S. Kim, *ACS Omega*, 2019, **4**, 21509–21515.
79 J. Zheng, A. Xu, A. Wu and X. Li, *ACS Appl. Mater. Interfaces*, 2021, **13**, 21231–21240.
80 S. P. Flynn, M. McKenna, R. Monaghan, S. M. Kelleher, S. Daniels and A. MacCormac, *J. Chem. Educ.*, 2017, **94**, 221–225.
81 Y. Huang, L. Cao and P. Zeng, *Russ. J. Phys. Chem.*, 2023, **97**, 3399–3404.
82 M. Zhao, D. Chen, Y. Guo, Q. Wang, T. Zhao, J. Lu and Y. Zhou, *Thin Solid Films*, 2023, **784**, 140064.


Open Access Article. Published on 15 2025. Downloaded on 2025/6/3 7:37:30.
This article is licensed under a Creative Commons Attribution 3.0 Unported Licence.

Journal of Materials Chemistry A Accepted Manuscript



This journal is © The Royal Society of Chemistry 20xx

Please do not adjust margins

Open Access Article. Published on 15 2025. Downloaded on 2025/6/3 7:37:30.
This article is licensed under a Creative Commons Attribution 3.0 Unported Licence.

Journal of Materials Chemistry A Accepted Manuscript


83 J.-H. Oh, T. K. Lee, R. Y. Kim, J.-H. An, S.-I. Mo, J.-E. Hong, S.-W. Kim, M. J. Keum, H. Song and K.-H. Kim, *Small Structures*, 2024, **5**, 2300218.

84 J. Cho, H. Seok, I. Lee, J. Lee, E. Kim, D. Sung, I.-K. Baek, C.-H. Lee and T. Kim, *Sci Rep*, 2022, **12**, 10335.

85 L. Himics, D. Gál, P. Csíkvári, R. Holomb, M. Koós, A. Sulyok, B. Pécz and M. Veres, *Vacuum*, 2023, **216**, 112493.

86 V. A. Terekhov, E. I. Terukov, Y. K. Undalov, K. A. Barkov, N. A. Kurilo, S. A. Ivkov, D. N. Nesterov, P. V. Seredin, D. L. Goloshchapov, D. A. Minakov, E. V. Popova, A. N. Lukin and I. N. Trapeznikova, *Symmetry*, 2023, **15**, 1800.

87 C. Wu, D. Y. Guo, L. Y. Zhang, P. G. Li, F. B. Zhang, C. K. Tan, S. L. Wang, A. P. Liu, F. M. Wu and W. H. Tang, *Applied Physics Letters*, 2020, **116**, 072102.

88 V. K. Shukla, L. J., B. S. Yadav, M. Kumari, S. Dalal, A. Goyal and P. Rai, *International Journal of Refractory Metals and Hard Materials*, 2024, **119**, 106559.

89 H.-U. Kim, H. Seok, W. S. Kang and T. Kim, *Nanoscale Adv.*, 2022, **4**, 2962–2972.

90 V. S. Jayaseelan and R. N. Singh, *Journal of Materials Research*, 2024, **39**, 825–835.

91 H. Tian, S. Jie, P. Zhang, J. Li and S. An, *Diamond and Related Materials*, 2024, **141**, 110671.

92 A. M. Mumlyakov, E. A. Pershina, Ju. V. Bondareva, P. A. Nekludova, A. A. Shibalova, M. V. Shibalov, Yu. V. Anufriev, A. M. Tagachenkov and M. A. Tarkhov, *Carbon*, 2023, **214**, 118332.

93 Y. Ma, J. Han, D. Yue, Z. Tong, M. Wang, L. Xiao, S. Jia and X. Chen, *Inorg. Chem.*, 2023, **62**, 13505–13511.

94 R. Muñoz, E. López-Elvira, C. Munuera, F. Carrascoso, Y. Xie, O. Çakıroğlu, T. Pucher, S. Puebla, A. Castellanos-Gomez and M. García-Hernández, *npj 2D Mater Appl*, 2023, **7**, 1–11.

95 T.-T. Zhang, B.-H. Lv, C.-C. Fan, B.-Y. Shi, Q.-J. Cao, W. Wang, F.-F. Tao and W.-D. Dou, *ACS Omega*, 2023, **8**, 36245–36252.

96 W. J. Lee, T.-Y. Cho, J.-H. Eom, J.-S. Park, J. Ryu and S.-K. Cho, *Plasma Processes and Polymers*, 2022, **19**, 2200001.

97 A. M. Wrobel and P. Uznanski, *Plasma Processes and Polymers*, 2023, **20**, 2200190.

98 G. Akiki, D. Suchet, D. Daineka, S. Filonovich, P. Bulkin and E. V. Johnson, *Applied Surface Science*, 2020, **531**, 147305.

99 B. Jugdersuren, X. Liu, J. C. Culbertson, N. Mahadik, O. Thomas and Y. Shu, *Journal of Applied Physics*, 2023, **134**, 214303.

100 C. Yu, K. Gao, C.-W. Peng, C. He, S. Wang, W. Shi, V. Allen, J. Zhang, D. Wang, G. Tian, Y. Zhang, W. Jia, Y. Song, Y. Hu, J. Colwell, C. Xing, Q. Ma, H. Wu, L. Guo, G. Dong, H. Jiang, H. Wu, X. Wang, D. Xu, K. Li, J. Peng, W. Liu, D. Chen, A. Lennon, X. Cao, S. De Wolf, J. Zhou, X. Yang and X. Zhang, *Nat Energy*, 2023, **8**, 1375–1385.

101 D. Liu, X. Chen, Y. Yan, Z. Zhang, Z. Jin, K. Yi, C. Zhang, Y. Zheng, Y. Wang, J. Yang, X. Xu, J. Chen, Y. Lu, D. Wei, A. T. S. Wee and D. Wei, *Nat Commun*, 2019, **10**, 1188.

102 K. Chakrabarty, I. Arnold and S. A. Catledge, *Journal of Vacuum Science & Technology A*, 2019, **37**, 061507.

103 K. Yi, Z. Jin, S. Bu, D. Wang, D. Liu, Y. Huang, Y. Dong, Q. Yuan, Y. Liu, A. T. S. Wee and D. Wei, *ACS Appl. Mater. Interfaces*, 2020, **12**, 33113–33120.

104 B. Schurink, W. T. E. van den Beld, R. M. Tiggelaar, R. W. E. van de Kruijs and F. Bijkerk, *Coatings*, 2022, **12**, 685.

105 H. Nadhom, D. Lundin, P. Rouf and H. Pedersen, *Journal of Vacuum Science & Technology A*, 2020, **38**, 033402.

106 D. E. Gomersall and A. J. Flewitt, *Journal of Applied Physics*, 2022, **131**, 215301.

107 P. M. Campbell, C. J. Perini, J. Chiu, A. Gupta, H. S. Ray, H. Chen, K. Wenzel, E. Snyder, B. K. Wagner, J. Ready and E. M. Vogel, *2D Mater.*, 2017, **5**, 015005.

108 H. He, C. Wu, H. Hu, S. Wang, F. Zhang, D. Guo and F. Wu, *J. Phys. Chem. Lett.*, 2023, **14**, 6444–6450.

109 C. A. Beaudette, J. T. Held, K. A. Mkhoyan and U. R. Kortshagen, *ACS Omega*, 2020, **5**, 21853–21861.

110 K. M. M. D. K. Kimbulapitiya, B. Rehman, S. S. Wani, C.-T. Chen, R.-H. Cyu, A. Manikandan, M. K. Date, Y.-R. Peng, R. J. G. L. R. Kumara, F.-C. Chuang and Y.-L. Chueh, *Nano Energy*, 2024, **122**, 109235.

111 E. Z. Frątczak, J. Balcerzak and M. Rogala, *Materials*, 2024, **17**, 314.

112 Y. Xia, Z. Xu, J. Peng, Q. Shen and C. Wang, *Surface and Coatings Technology*, 2022, **441**, 128522.

113 M. A. Kudryashov, L. A. Mochalov, I. O. Prokhorov, M. A. Vshivtsev, Yu. P. Kudryashova, V. M. Malyshev and E. A. Slapovskaya, *High Energy Chem*, 2023, **57**, 532–536.

114 T.-H. Yang, Z.-Z. Lin, S.-C. Tsai, J.-Z. Dai, S.-M. Chen, M.-W. Lin and S. Chen, *Materials Science in Semiconductor Processing*, 2023, **162**, 107515.




Please do not adjust margins

View Article Online
DOI: 10.1039/D5TA01081K

Open Access Article. Published on 15 2025. Downloaded on 2025/6/3 7:37:30.
This article is licensed under a Creative Commons Attribution 3.0 Unported Licence.

Journal of Materials Chemistry A Accepted Manuscript


115 C. Yadav, M. Kumar, K. Lodhi and S. Kumar, *Materials Today Communications*, 2023, **36**, 106736.

116 M. Gürsoy, *Coatings*, 2024, **14**, 347.

117 O. Richard, H. Mziouek, R. Arès, V. Aimez and A. Jaouad, *Surfaces and Interfaces*, 2023, **40**, 103104.

118 K. D. Lee, K.-S. Ji, S. Bae, S. Kim, H. Kim, J. E. Kim, Y. C. Nam, S. Choi, M. S. Jeong, M. G. Kang, H.-E. Song, Y. Kang, H.-S. Lee and D. Kim, *Journal of Nanoscience and Nanotechnology*, 2017, **17**, 4687–4693.

119 S. Ahn, S. J. Hong, H. S. Yang and S. M. Cho, *Materials Science in Semiconductor Processing*, 2022, **143**, 106538.

120 H.-L. Chen, Y.-C. Tu, C.-C. Hsieh, D.-L. Lin and K.-C. Leou, *Journal of Applied Physics*, 2014, **116**, 103307.

121 B. B. Sahu and J. G. Han, *Physics of Plasmas*, 2016, **23**, 123504.

122 G. Das, S. Mandal, S. Dhar, S. Bose, J. R. Sharma, S. Mukhopadhyay, C. Banerjee and A. K. Barua, *J Mater Sci: Mater Electron*, 2017, **28**, 10382–10390.

123 X. Li, R. Jin, L. Li, J. Lu, Y. Gu, F. Ren and J. Huang, *Optik*, 2019, **180**, 104–112.

124 M. A. Yusuf, A. Rosikhin, J. D. Malago, F. A. Noor and T. Winata, *Materials Science Forum*, 2019, **966**, 100–106.

125 S. Juneja and S. Kumar, *Silicon*, 2021, **13**, 3927–3940.

126 X. Zhou, X. Tan, Y. Lv, Y. Wang, J. Li, S. Liang, Z.-H. Zhang, Z. Feng and S. Cai, *Opt. Express, OE*, 2020, **28**, 29245–29252.

127 P. R. Y. Gangavarapu, A. M. R. Sharma and A. K. Naik, *Semicond. Sci. Technol.*, 2019, **34**, 065018.

128 B. B. Sahu, Y. Yin and J. G. Han, *Physics of Plasmas*, 2016, **23**, 033512.

129 C. Chen, W. Fu, C. Zhang, D. Lu, M. Han and Y. Yan, *Applied Sciences*, 2021, **11**, 9873.

130 M. Cantoro, S. Hofmann, C. Mattevi, S. Pisana, A. Parvez, A. Fasoli, C. Ducati, V. Scardaci, A. C. Ferrari and J. Robertson, *Journal of Applied Physics*, 2009, **105**, 064304.

131 T. Labbaye, E. Kovacevic, T. Lecas, M.-R. Ammar, A. Canizarès, N. Raimboux, T. Strunskus, C. Jaeger, P. Simon and C. Boulmer-Leborgne, *Applied Surface Science*, 2018, **453**, 436–441.

132 U. Sharma and S. C. Sharma, *IEEE Transactions on Plasma Science*, 2022, **50**, 888–898.

133 U. Khalilov, A. Bogaerts, S. Hussain, E. Kovacevic, P. Brault, C. Boulmer-Leborgne and E. C. Neyts, *J. Phys. D: Appl. Phys.*, 2017, **50**, 184001.

134 Z. Jiang, B. Zhang, Q. Shen and Z.-J. Jiang, *Journal of Alloys and Compounds*, 2019, **806**, 864–873.

135 W. Wang, É. Ngo, P. Bulkin, Z. Zhang, M. Foldyna, P. Roca i Cabarrocas, E. V. Johnson and J.-L. Maurice, *Nanomaterials*, 2023, **13**, 2061.

136 S. Djoumi, F. Kail, P. R. i Cabarrocas and L. Chahed, *Thin Solid Films*, 2022, **758**, 139447.

137 J. Tang, J.-L. Maurice, W. Chen, S. Misra, M. Foldyna, E. V. Johnson and P. Roca i Cabarrocas, *Nanoscale Res Lett*, 2016, **11**, 455.

138 M. Hývl, M. Müller, T.-H. Stuchlíková, J. Stuchlík, M. Šilhavík, J. Kočka, A. Fejfar and J. Červenka, *Nanotechnology*, 2020, **31**, 225601.

139 A. O. Zamchiy, E. A. Baranov, S. Ya. Khmel, E. A. Maximovskiy, D. V. Gulyaev and K. S. Zhuravlev, *Thin Solid Films*, 2018, **654**, 61–68.

140 E. Azrak, W. Chen, S. Moldovan, S. Gao, S. Duguay, P. Pareige and P. Roca i Cabarrocas, *J. Phys. Chem. C*, 2018, **122**, 26236–26242.

141 L. Zheng, E. Azrak, R. Gong, C. Castro, S. Duguay, P. Pareige, P. Roca i Cabarrocas and W. Chen, *Journal of Alloys and Compounds*, 2022, **899**, 163273.

142 L. Dai, I. Maurin, M. Foldyna, J. Alvarez, W. Wang, H. Mohsin, W. Chen, J.-P. Kleider, J.-L. Maurice, T. Gacoin and P. R. i Cabarrocas, *Nanotechnology*, 2018, **29**, 435301.

143 W. Yang, X. Zhang, F. Huang, Z. Zhang, J. Muhammad, X. Li, Z. Rong, X. Guo, Y. Jung and X. Dong, *Applied Surface Science*, 2021, **557**, 149848.

144 E. Azrak, Z. Xue, S. Liu, W. Chen, C. Castro, S. Duguay, P. Pareige, L. Yu and P. Roca i Cabarrocas, *Applied Surface Science*, 2023, **618**, 156637.

145 J. W. Miller, Z. Khatami, J. Wojcik, J. D. B. Bradley and P. Mascher, *Surface and Coatings Technology*, 2018, **336**, 99–105.

146 F. Azmi, Y. Gao, Z. Khatami and P. Mascher, *Journal of Vacuum Science & Technology A*, 2022, **40**, 043402.

147 Z. Khatami, L. Wolz, J. Wojcik and P. Mascher, *Journal of Materials Research*, 2024, **39**, 150–164.

148 F. Azmi, Y. Gao, Z. Khatami and P. Mascher, *Meet. Abstr.*, 2020, **MA2020-01**, 2934.

149 R. B. Namin, P. Mascher, F. Chibante and Z. Khatami, *ECS J. Solid State Sci. Technol.*, 2023, **12**, 106002.

150 J. Kulczyk-Malecka, D. Donaghy, B. Delfour-Peyrethon, M. Werner, P. R. Chalker, J. W. Bradley and P. J. Kelly, *Journal of Vacuum Science & Technology A*, 2020, **38**, 033410.

151 N. R. Lee, Y. S. Jun, K. I. Moon and C. S. Lee, *Jpn. J. Appl. Phys.*, 2017, **56**, 035506.




This journal is © The Royal Society of Chemistry 20xx

Please do not adjust margins

View Article Online
DOI: 10.1039/D5TA01081K

Open Access Article. Published on 15 2025. Downloaded on 2025/6/3 7:37:30.
This article is licensed under a Creative Commons Attribution 3.0 Unported Licence.

Journal of Materials Chemistry A Accepted Manuscript

152 K. H. Kim, K. S. Kim, Y. J. Ji, J. E. Kang and G. Y. Yeom, *Applied Surface Science*, 2021, **541**, 148313.
153 Z. Huang, Z. Chen, W. Lang and X. Wang, *Materials*, 2021, **14**, 2954.
154 R. Song, S. Chen, Z. Liu, C. Huo and Q. Chen, *Diamond and Related Materials*, 2023, **132**, 109687.
155 S.-C. Lin, C.-C. Wang, C.-L. Tien, F.-C. Tung, H.-F. Wang and S.-H. Lai, *Micromachines*, 2023, **14**, 279.
156 N. Q. Minh, N. Van Nong, M. S. D. C. Dela Vega, O. Oda and M. Hori, *Vacuum*, 2023, **213**, 112118.
157 A. Dias, N. Bundaleska, E. Felizardo, D. Tsyganov, A. Almeida, A. M. Ferraria, A. M. Botelho do Rego, M. Abrashev, Th. Strunskus, N. M. Santhosh, U. Cvelbar, J. Zavašnik, M. F. Montemor, M. M. Almeida, P. A. Carvalho, J. Kissovski, L. L. Alves and E. Tatarova, *Chemical Engineering Journal*, 2022, **430**, 133153.
158 M. Su, H. Yang, Z. Liu, E. Wu, X. Chen, Z. Bo, L. Dai and K. (Ken) Ostrikov, *Carbon*, 2022, **197**, 301–310.
159 B. Dey, S. Bulou, W. Ravisy, N. Gautier, M. Richard-Plouet, A. Granier and P. Choquet, *Surface and Coatings Technology*, 2022, **436**, 128256.
160 C. T. Tran, M. Raco, L. M. Casey and D. R. McKenzie, *Plasma Processes and Polymers*, 2022, **19**, 2200019.
161 A. Capote, G. Capote, E. J. Corat and V. J. Trava-Airoldi, *Surface and Coatings Technology*, 2022, **445**, 128716.
162 K. Yamasaki, T. Matsutani, N. Imaeda and T. Kawasaki, *Vacuum*, 2015, **122**, 332–336.
163 M. Murano, T. Matsutani and T. Kawasaki, *Vacuum*, 2018, **158**, 60–64.
164 D. Batryshev, A. Utegenov, R. Zhumadilov, N. Akhanova, S. Orazbayev, S. Ussenkhan, J. Lin, K. Takahashi, N. Bastykova, S. Kodanova, M. Gabdullin and T. Ramazanov, *Contributions to Plasma Physics*, 2022, **62**, e202100238.
165 Z. Guo, L. Sang, Z. Wang, Q. Chen, L. Yang and Z. Liu, *Surface and Coatings Technology*, 2016, **307**, 1059–1064.
166 Y. HU, X. TIAN, Q. FAN, Z. WANG, B. LIU, L. YANG and Z. LIU, *Plasma Sci. Technol.*, 2019, **21**, 105502.
167 S. Bulou, E. Lecoq, F. Loyer, G. Frache, T. Fouquet, M. Gueye, T. Belmonte and P. Choquet, *Plasma Processes and Polymers*, 2019, **16**, 1800177.
168 C. Ruhmlieb, Y. J. Lee, C. Strelow, T. Kipp and A. Mews, *J. Mater. Chem. C*, 2019, **7**, 10098–10110.
169 M. Taplick, C. Ruhmlieb, T. Kipp and A. Mews, *Nano Lett.*, 2023, **23**, 1313–1319.
170 M. A. A. Mamun, H. Furuta and A. Hatta, *Jpn. J. Appl. Phys.*, 2018, **57**, 06JF02.
171 R. Hatada, S. Flege, M. N. Ashraf, A. Timmermann, C. Schmid and W. Ensinger, *Coatings*, 2020, **10**, 360.
172 R. Hatada, K. Baba, S. Flege and W. Ensinger, *Surface and Coatings Technology*, 2016, **305**, 93–98.
173 S. de F. M. Mariano, M. Ueda, R. M. Oliveira, E. J. de D. M. Pillaca and N. M. dos Santos, *Surface and Coatings Technology*, 2017, **312**, 47–54.
174 S. F. M. Mariano and M. Ueda, *Applied Surface Science*, 2019, **465**, 824–832.
175 Z. Wu, E. Wang, G. Zhang, Y. Shen and G. Shao, *Small*, **n/a**, 2307923.
176 H. Wang, Y. Han, P. Luo, Y. Zhou, Q. Chen, H. Zhu, Y. Yang, B. Zhang and K. Huang, *ChemistrySelect*, 2022, **7**, e202200103.
177 S. Sahoo, G. Sahoo, S. M. Jeong and C. S. Rout, *Journal of Energy Storage*, 2022, **53**, 105212.
178 M. A. Zafar and M. V. Jacob, *Rev. Mod. Plasma Phys.*, 2022, **6**, 37.
179 S. Zheng, Q. Wang, K. Guo, J. Bai, Z. Yang, H. Yu, H. Liu, H. Wei, J. Zhu and Q. Hu, *Journal of Crystal Growth*, 2024, **627**, 127538.
180 O. Baranov, I. Levchenko, S. Xu, J. W. M. Lim, U. Cvelbar and K. Bazaka, *2D Mater.*, 2018, **5**, 044002.
181 W. Zheng, X. Zhao and W. Fu, *ACS Appl. Mater. Interfaces*, 2021, **13**, 9561–9579.
182 A. Khan, J. Cong, R. R. Kumar, S. Ahmed, D. Yang and X. Yu, *ACS Appl. Nano Mater.*, 2022, **5**, 17544–17555.
183 S. Ghosh, S. R. Polaki, M. Kamruddin, S. M. Jeong and K. (Ken) Ostrikov, *J. Phys. D: Appl. Phys.*, 2018, **51**, 145303.
184 M. R. Maschmann, P. B. Amama, A. Goyal, Z. Iqbal and T. S. Fisher, *Carbon*, 2006, **44**, 2758–2763.
185 A. Thapa, S. Neupane, R. Guo, K. L. Jungjohann, D. Pete and W. Li, *Diamond and Related Materials*, 2018, **90**, 144–153.
186 J. Sun, T. Rattanasawatesun, P. Tang, Z. Bi, S. Pandit, L. Lam, C. Wasén, M. Erlandsson, M. Bokarewa, J. Dong, F. Ding, F. Xiong and I. Mijakovic, *ACS Appl. Mater. Interfaces*, 2022, **14**, 7152–7160.
187 A. Tewari, S. Ghosh and P. Srivastava, *Plasma Res. Express*, 2021, **3**, 035003.
188 S. Xu, S. Wang, Z. Chen, Y. Sun, Z. Gao, H. Zhang and J. Zhang, *Advanced Functional Materials*, 2020, **30**, 2003302.



Please do not adjust margins

189 C. Shen, S. Xu, Z. Chen, N. Ji, J. Yang and J. Zhang, *Small*, 2023, **19**, 2207745.
190 S. Xu, T. Cheng, Q. Yan, C. Shen, Y. Yu, C.-T. Lin, F. Ding and J. Zhang, *Advanced Science*, 2022, **9**, 2200737.
191 S. Xu, Y. Wen, Z. Chen, N. Ji, Z. Zou, M. Wu, L. Qu and J. Zhang, *Angewandte Chemie International Edition*, 2021, **60**, 24505–24509.
192 S.-F. Wang, D. Xue, J. Liang, L.-Y. Chen, Y. Xie and J.-M. Zhang, *Diamond and Related Materials*, 2023, **140**, 110426.
193 D. H. Seo, S. Yick, Z. J. Han, J. H. Fang and K. (Ken) Ostrikov, *ChemSusChem*, 2014, **7**, 2317–2324.
194 L.-A. Gautier, V. Le Borgne and M. A. El Khakani, *Carbon*, 2016, **98**, 259–266.
195 W.-H. Chiang, T.-C. Lin, Y.-S. Li, Y.-J. Yang and Z. Pei, *RSC Advances*, 2016, **6**, 2270–2278.
196 X. Peng, Z. Wang, Z. Wang, J. Gong and H. Hao, *Catalysis Today*, 2019, **337**, 63–68.
197 E. P. Neustroev, A. R. Prokopyev, S. O. Semenov, V. I. Popov, F. F. Protopopov, A. S. Andreev, N. A. Savvinova and E. S. Lukin, *IOP Conf. Ser.: Mater. Sci. Eng.*, 2021, **1079**, 042086.
198 A. Dias, E. Felizardo, N. Bundaleska, M. Abrashev, J. Kissovski, A. M. Ferraria, A. M. Rego, T. Strunskus, P. A. Carvalho, A. Almeida, J. Zavašnik, E. Kovacevic, J. Berndt, N. Bundaleski, M.-R. Ammar, O. M. N. D. Teodoro, U. Cvelbar, L. L. Alves, B. Gonçalves and E. Tatarova, *Applied Materials Today*, 2024, **36**, 102056.
199 J. Zheng, R. Yang, Y. Lou, W. Li and X. Li, *Thin Solid Films*, 2012, **521**, 137–140.
200 H. Seok, Y. T. Megra, C. K. Kanade, J. Cho, V. K. Kanade, M. Kim, I. Lee, P. J. Yoo, H.-U. Kim, J. W. Suk and T. Kim, *ACS Nano*, 2021, **15**, 707–718.
201 Y. Kim, S. Kwon, E.-J. Seo, J. H. Nam, H. Y. Jang, S.-H. Kwon, J.-D. Kwon, D.-W. Kim and B. Cho, *ACS Appl. Mater. Interfaces*, 2018, **10**, 36136–36143.
202 R. K. Joshi, M. Yoshimura, K. Tanaka, K. Ueda, A. Kumar and N. Ramgir, *J. Phys. Chem. C*, 2008, **112**, 13901–13904.
203 S. A. Ahmad Kamal, R. Ritikos and S. Abdul Rahman, *Applied Surface Science*, 2015, **328**, 146–153.
204 H. Hamidinezhad, A. Akbar Ashkarran and Z. Abdul-Malek, *Materials Science in Semiconductor Processing*, 2014, **27**, 26–32.
205 M. Macias-Montero, A. Borras, Z. Saghi, J. P. Espinos, A. Barranco, J. Cotrino and A. R. Gonzalez-Elipe, *Nanotechnology*, 2012, **23**, 255303.
206 N. Filippin, J. Castillo-Seoane, M. C. López-Santos, C. T. Rojas, K. Ostrikov, A. Barranco, J. R. Sánchez-Valencia and A. Borrás, *ACS Appl. Mater. Interfaces*, 2020, **12**, 50721–50733.
207 M. C. Vasudev, H. Koerner, K. M. Singh, B. P. Partlow, D. L. Kaplan, E. Gazit, T. J. Bunning and R. R. Naik, *Biomacromolecules*, 2014, **15**, 533–540.
208 Z. He, C. S. Lee, J.-L. Maurice, D. Pribat, P. Haghi-Ashtiani and C. S. Cojocaru, *Carbon*, 2011, **49**, 4710–4718.
209 J. Jiang, N. M. Chetuya, E. I. Meletis, J. H. Ngai, G. J. Grzybowski and B. Claflin, *Journal of Vacuum Science & Technology B*, 2024, **42**, 034001.
210 H.-U. Kim, M. Kim, H. Seok, K.-Y. Park, J.-Y. Moon, J. Park, B.-S. An, H. J. Jung, V. P. Dravid, D. Whang, J.-H. Lee and T. Kim, *ChemSusChem*, 2021, **14**, 1344–1350.
211 Y. Xing, S. Dong, X. Zhang, Y. Zhang, J. Han, X. Zhang, L. Zhang, B. Zhang and Z. Zeng, *Crystal Growth & Design*, 2023, **23**, 2257–2263.
212 V. Brune, M. Grosch, R. Weißing, F. Hartl, M. Frank, S. Mishra and S. Mathur, *Dalton Trans.*, 2021, **50**, 12365–12385.
213 P. Albert L. Sino, T.-C. Lin, S. Wani, L. Lee, C.-T. Chen, M.-J. Liu, Y.-Z. Kuo, B. Rehman, K. Tuyen Le, J.-M. Wu, F.-C. Chuang and Y.-L. Chueh, *Materials Today*, 2023, **69**, 97–106.
214 M. Chaudhary, T.-Y. Yang, C.-T. Chen, P.-C. Lai, Y.-C. Hsu, Y.-R. Peng, A. Kumar, C.-H. Lee and Y.-L. Chueh, *Advanced Functional Materials*, 2023, **33**, 2303697.
215 J. Park, I. Cho, H. Jeon, Y. Lee, J. Zhang, D. Lee, M. K. Cho, D. J. Preston, B. Shong, I. S. Kim and W.-K. Lee, *Advanced Materials*, **36**, 2314031.
216 H.-U. Kim, V. Kanade, M. Kim, K. S. Kim, B.-S. An, H. Seok, H. Yoo, L. E. Chaney, S.-I. Kim, C.-W. Yang, G. Y. Yeom, D. Whang, J.-H. Lee and T. Kim, *Small*, 2020, **16**, 1905000.
217 R. Zhang, Q. Zhang, X. Jia, S. Wen, H. Wu, Y. Gong, Y. Yin, C. Lan and C. Li, *Nanotechnology*, 2023, **34**, 345704.
218 K. Aydin, C. Kanade, V. Kaluram Kanade, G. Bahit, C. Ahn and T. Kim, *Nanoscale*, 2023, **15**, 17326–17334.
219 C. Ahn, J. Lee, H.-U. Kim, H. Bark, M. Jeon, G. H. Ryu, Z. Lee, G. Y. Yeom, K. Kim, J. Jung, Y. Kim, C. Lee and T. Kim, *Advanced Materials*, 2015, **27**, 5223–5229.
220 H. Seok, M. Kim, J. Cho, E. Kim, S. Son, K.-W. Kim, J. K. Kim, P. J. Yoo, M. Kim, H.-U. Kim and T. Kim, *ACS Sustainable Chem. Eng.*, 2023, **11**, 568–577.

Open Access Article. Published on 15 2025. Downloaded on 2025/6/3 7:37:30.
This article is licensed under a Creative Commons Attribution 3.0 Unported Licence.

Journal of Materials Chemistry A Accepted Manuscript



This journal is © The Royal Society of Chemistry 20xx

Please do not adjust margins

DOI: 10.1039/D5TA01081K

221 J. H. Kim, S. J. Yun, H. S. Lee, J. Zhao, H. Bouzid and Y. H. Lee, *Sci Rep*, 2018, **8**, 10284.
222 Y. Li, J. Duan, Y. Berencén, R. Hübner, H.-S. Tsai, C.-N. Kuo, C. Shan Lue, M. Helm, S. Zhou and S. Prucnal, *Nanoscale Advances*, 2023, **5**, 443–449.
223 J. Cho, H. Seok and T. Kim, *Meet. Abstr.*, 2023, **MA2023-02**, 1157.
224 M. Chaudhary, Y.-C. Shih, S.-Y. Tang, T.-Y. Yang, T.-W. Kuo, C.-C. Chung, Y.-C. Shen, A. kumar Anbalagan, C.-H. Lee, T.-H. Hou, J.-H. He and Y.-L. Chueh, *ACS Appl. Mater. Interfaces*, 2023, **15**, 33858–33867.
225 W. Fan, H. Shen, B. Liu, L. Zhao, X. Zhang and H. Pan, *Energies*, 2023, **16**, 6963.
226 B. Grübel, H. Nagel, B. Steinhauser, F. Feldmann, S. Kluska and M. Hermle, *physica status solidi (a)*, 2021, **218**, 2100156.
227 J.-S. Song, Y. S. Park and N.-H. Kim, *Applied Sciences*, 2021, **11**, 358.
228 Z. Zhong, X. Luo, L. Zhou, S. Hu, L. Dai, S. Wang and S. Yang, *Opt Quant Electron*, 2023, **55**, 264.
229 Y.-R. Zhang, Y.-T. Hu and Y.-N. Wang, *Plasma Sources Sci. Technol.*, 2020, **29**, 084003.
230 H. J. Kim, K. Lee and H. Park, *Plasma Sources Sci. Technol.*, 2024, **33**, 015008.
231 H. J. Kim, K. Lee and H. Park, *Plasma Sources Sci. Technol.*, 2023, **32**, 115008.
232 D. Li, X. Feng, Z. Wen, Z. Shang and Y. She, *Optoelectron. Lett.*, 2016, **12**, 285–289.
233 H. Lim, Y. Park, N. Baek, S.-Y. Jun, S. Lee, J. Yang, D. Jung and S. Yu, *Journal of Nanoscience and Nanotechnology*, 2021, **21**, 4477–4483.
234 E. Bertran-Serra, A. Musheghyan-Avetisyan, S. Chaitoglou, R. Amade-Rovira, I. Alshaikh, F. Pantoja-Suárez, J.-L. Andújar-Bella, T. Jawhari, A. Perez-del-Pino and E. Gyorgy, *Applied Surface Science*, 2023, **610**, 155530.
235 G. Sato, T. Kato, W. Oohara and R. Hatakeyama, *Thin Solid Films*, 2006, **506–507**, 550–554.
236 C. R. Yang, C. H. Yeh, L. C. Hu, T. C. Wei, C. C. Lee, J. Y. Chang and T. T. Li, *Plasma Chem Plasma Process*, 2018, **38**, 247–259.
237 J. Miller, A. Ceballos, L. B. Bayu Aji, A. Moore, C. Wasz, S. O. Kucheyev, S. Elhadj and S. Falabella, *Thin Solid Films*, 2020, **714**, 138394.
238 L. C. Hu, G. M. Ruan, T. C. Wei, C. J. Wang, Y. W. Lin, C. C. Lee, Y. Kawai and T. T. Li, *Thin Solid Films*, 2014, **570**, 574–579.
239 P. Ji, J. Chen, T. Huang, L. Zhuge and X. Wu, *Diamond and Related Materials*, 2020, **109**, 108067.
240 Y. Xia, X. Yang, L. Chang, H. Zhou, J.-H. Zhang, D. Jing, Q. Xu, G.-J. Niu, H.-S. Zhou and G.-N. Luo, *Review of Scientific Instruments*, 2023, **94**, 125110.
241 Y. Yang, T. Huang, M. Li, Y. Yu, J. Huang, B. Yu, X. Wu and P. Ji, *Plasma Sci. Technol.*, 2022, **24**, 105502.
242 J. Chen, P. Ji, M. Li, T. Huang, L. Zhuge and X. Wu, *Plasma Sci. Technol.*, 2022, **24**, 054001.
243 P. Ji, J. Chen, T. Huang, C. Jin, L. Zhuge and X. Wu, *Diamond and Related Materials*, 2020, **108**, 107958.
244 P. Ji, J. Chen, T. Huang, C. Jin, L. Zhuge and X. Wu, *Appl. Phys. A*, 2020, **126**, 247.
245 X. Ma, D. Xu, P. Ji, C. Jin, J. Lin, Y. Ding and C. Xu, *Vacuum*, 2019, **164**, 355–360.
246 D. Li, S. Dai, A. Goullet and A. Granier, *NANO*, 2018, **13**, 1850124.
247 P. Ji, J. Yu, T. Huang, C. Jin, Y. Yang, L. Zhuge and X. Wu, *Plasma Sci. Technol.*, 2018, **20**, 025505.
248 J. Chen, P. Ji, C. JIN, L. Zhuge and X. Wu, *Plasma Sci. Technol.*, 2018, **21**, 025502.
249 J. Qian, P. Ji, C. Jin, L. Zhuge and X. Wu, *IEEE Transactions on Plasma Science*, 2020, **48**, 2431–2436.
250 T. Goto, K.-I. Sato, Y. Yabuta, S. Sugawa and S. Hara, *IEEE Journal of the Electron Devices Society*, 2018, **6**, 512–517.
251 H. Bae, I. Hamaguchi, K. Sasai, H. Suzuki and H. Toyoda, *Jpn. J. Appl. Phys.*, 2021, **60**, 126002.
252 S. Patil, S. Sharma, S. Sengupta, A. Sen and I. Kaganovich, *Phys. Rev. Res.*, 2022, **4**, 013059.
253 M. Magarotto, D. Melazzi and D. Pavarin, *Journal of Plasma Physics*, 2019, **85**, 905850404.
254 Q.-Z. Zhang, J.-Y. Sun, W.-Q. Lu, J. Schulze, Y.-Q. Guo and Y.-N. Wang, *Phys. Rev. E*, 2021, **104**, 045209.
255 S. Sharma, I. D. Kaganovich, A. V. Khrabrov, P. Kaw and A. Sen, *Physics of Plasmas*, 2018, **25**, 080704.
256 T. Zhang, R. Cui, R. Han, F. He, W. Zhu, Z. Xia, Y. Cui and J. Ouyang, *Plasma Sources Sci. Technol.*, 2022, **31**, 105008.
257 A. O. Zamchiy, E. A. Baranov and S. Y. Khmel, *Vacuum*, 2018, **147**, 99–106.
258 A. O. Zamchiy, E. A. Baranov, I. E. Merkulova, V. A. Volodin, M. R. Sharafutdinov and S. Ya. Khmel, *Vacuum*, 2018, **152**, 319–326.
259 E. A. Baranov, A. O. Zamchiy, N. A. Lunev, I. E. Merkulova, V. A. Volodin, M. R. Sharafutdinov and A. A. Shapovalova, *J Appl Mech Tech Phy*, 2022, **63**, 757–764.

Open Access Article. Published on 15 2025. Downloaded on 2025/6/3 7:37:30.
This article is licensed under a Creative Commons Attribution 3.0 Unported Licence.

Journal of Materials Chemistry A Accepted Manuscript



Please do not adjust margins

View Article Online
DOI: 10.1039/D5TA01081K

Open Access Article. Published on 15 2025. Downloaded on 2025/6/3 7:37:30.
This article is licensed under a Creative Commons Attribution 3.0 Unported Licence.

Journal of Materials Chemistry A Accepted Manuscript


260 I. E. Merkulova, *J. Phys.: Conf. Ser.*, 2019, **1382**, 012160.
261 T. Tabuchi, Y. Toyoshima, S. Fujimoto and M. Takashiri, *Thin Solid Films*, 2020, **694**, 137714.
262 T. Tabuchi, Y. Toyoshima, S. Fujimoto and M. Takashiri, *AIP Advances*, 2019, **9**, 055125.
263 H. Sugiura, H. Kondo, T. Tsutsumi, K. Ishikawa and M. Hori, *C*, 2019, **5**, 8.
264 L. Jia, H. Sugiura, H. Kondo, K. Takeda, K. Ishikawa, O. Oda, M. Sekine, M. Hiramatsu and M. Hori, *Plasma Processes and Polymers*, 2016, **13**, 730–736.
265 H. Sugiura, L. Jia, Y. Ohashi, H. Kondo, K. Ishikawa, T. Tsutsumi, T. Hayashi, K. Takeda, M. Sekine and M. Hori, *Jpn. J. Appl. Phys.*, 2019, **58**, 030912.
266 T. Ichikawa, N. Shimizu, K. Ishikawa, M. Hiramatsu and M. Hori, *Carbon*, 2020, **161**, 403–412.
267 X.-F. Wang, W.-Z. Jia, Y.-H. Song, Y.-Y. Zhang, Z.-L. Dai and Y.-N. Wang, *Physics of Plasmas*, 2017, **24**, 113503.
268 D. Lundin, J. Jensen and H. Pedersen, *Journal of Vacuum Science & Technology A*, 2014, **32**, 030602.
269 M. A. A. Mamun, H. Furuta and A. Hatta, *IEEE Transactions on Plasma Science*, 2019, **47**, 22–31.
270 H. Kakiuchi, H. Ohmi and K. Yasutake, *J. Phys. D: Appl. Phys.*, 2020, **53**, 415201.
271 Z. Gong, J. Shi, W. Ma, B. Zhang and J. Zhang, *RSC Advances*, 2016, **6**, 115092–115100.
272 Ö. Çelikel and H. Kavak, *Diamond and Related Materials*, 2021, **120**, 108610.
273 M. Y. Yoon, J.-R. Jeong, H.-C. Lee and J.-H. Kim, *Applied Surface Science*, 2023, **636**, 157814.
274 G. Kalita and M. Umeno, *AppliedChem*, 2022, **2**, 160–184.
275 A. M. Coclite and K. K. Gleason, *Plasma Processes and Polymers*, 2012, **9**, 425–434.
276 M. Gürsoy, *Plasma Chem Plasma Process*, 2020, **40**, 1063–1079.
277 M. Gürsoy, *Journal of Applied Polymer Science*, 2021, **138**, 49722.
278 F. Loyer, G. Bengasi, G. Frache, P. Choquet and N. D. Boscher, *Plasma Processes and Polymers*, 2018, **15**, 1800027.
279 D. D. Burkey, in *CVD Polymers*, John Wiley & Sons, Ltd, 2015, pp. 65–85.
280 M. Wang, N. D. Boscher, K. Heinze and K. K. Gleason, *Advanced Functional Materials*, 2017, **27**, 1606652.
281 A. Kumar, D. S. Grant, K. Bazaka and M. V. Jacob, *Journal of Applied Polymer Science*, 2018, **135**, 45771.
282 H. Akther, M. M. Rahman, A. H. Bhuiyan, H. Kabir, S. A.-A. Zumahi, J. A. Syed and R. Nasrin, *Materials Today Communications*, 2022, **31**, 103377.
283 A. Loesch-Zhang, A. Geissler and M. Biesalski, *Plasma Processes and Polymers*, 2023, **20**, e2300016.
284 T. Dufour, *Polymers*, 2023, **15**, 3607.
285 S. Matsui, in *Encyclopedia of Nanotechnology*, ed. B. Bhushan, Springer Netherlands, Dordrecht, 2012, pp. 866–876.
286 W. J. MoberlyChan, D. P. Adams, M. J. Aziz, G. Hobler and T. Schenkel, *MRS Bulletin*, 2007, **32**, 424–432.
287 M. Manoccio, M. Esposito, A. Passaseo, M. Cuscunà and V. Tasco, *Micromachines*, 2021, **12**, 6.
288 R. Winkler, J. D. Fowlkes, P. D. Rack and H. Plank, *Journal of Applied Physics*, 2019, **125**, 210901.
289 K. Höflich, G. Hobler, F. I. Allen, T. Wirtz, G. Rius, L. McElwee-White, A. V. Krasheninnikov, M. Schmidt, I. Utke, N. Klingner, M. Osenberg, R. Córdoba, F. Djurabekova, I. Manke, P. Moll, M. Manoccio, J. M. De Teresa, L. Bischoff, J. Michler, O. De Castro, A. Delobbe, P. Dunne, O. V. Dobrovolskiy, N. Frese, A. Gölzhäuser, P. Mazarov, D. Koelle, W. Möller, F. Pérez-Murano, P. Philipp, F. Vollnhals and G. Hlawacek, *Applied Physics Reviews*, 2023, **10**, 041311.
290 R. Winkler, B. B. Lewis, J. D. Fowlkes, P. D. Rack and H. Plank, *ACS Appl. Nano Mater.*, 2018, **1**, 1014–1027.
291 P. Niiranen, H. Nadhom, M. Zanáška, R. Boyd, M. Sortica, D. Primetzhofer, D. Lundin and H. Pedersen, *Review of Scientific Instruments*, 2023, **94**, 023902.
292 P. Niiranen, A. Kapran, H. Nadhom, M. Čada, Z. Hubička, H. Pedersen and D. Lundin, *Journal of Vacuum Science & Technology A*, 2024, **42**, 023006.
293 H. Nadhom, Y. Yuan, P. Rouf, N. Solin and H. Pedersen, *Journal of Vacuum Science & Technology A*, 2021, **39**, 043411.
294 G. Pozina, C.-W. Hsu, N. Abrikossova and C. Hemmingsson, *Crystals*, 2023, **13**, 373.
295 M. Xu, T. Bearda, M. Hasan, H. S. Radhakrishnan, I. Gordon, J. Szlufcik and J. Poortmans, in *2018 IEEE 7th World Conference on Photovoltaic Energy Conversion (WCPEC) (A Joint Conference of 45th IEEE PVSC, 28th PVSEC & 34th EU PVSEC)*, 2018, pp. 3148–3151.
296 H. Nadhom, R. Boyd, P. Rouf, D. Lundin and H. Pedersen, *J. Phys. Chem. Lett.*, 2021, **12**, 4130–4133.




This journal is © The Royal Society of Chemistry 20xx

Please do not adjust margins

View Article Online
DOI: 10.1039/D5TA01081K

297 G. Akiki, M. Frégnaux, I. Florea, P. Bulkin, D. Daineka, S. Filonovich, M. Bouttemy and E. V. Johnson, *Journal of Vacuum Science & Technology A*, 2020, **39**, 013201.
298 I. V. Otto IV, C. Vallée, S. Kal and P. Biolsi, *Journal of Vacuum Science & Technology B*, 2023, **41**, 032202.
299 D. N. Polyakov, V. V. Shumova and L. M. Vasilyak, *Plasma Sources Sci. Technol.*, 2021, **30**, 07LT01.
300 T. Faraz, K. Arts, S. Karwal, H. C. M. Knoops and W. M. M. Kessels, *Plasma Sources Sci. Technol.*, 2019, **28**, 024002.
301 S. J. C. Irvine and D. Lamb, in *Chemical Vapour Deposition: Precursors, Processes and Applications*, 2008, pp. 477–493.
302 C. P. Grigoropoulos, *International Journal of Extreme Manufacturing*, 2019, **1**, 012002.
303 J. Niu, S. Meng, J. Li, H. Jin, F. Yi and Y. Qin, *Ceramics International*, 2020, **46**, 2086–2092.
304 S. Miyata, K. Matsuse, A. Ibi, T. Izumi, Y. Shiohara and T. Goto, *Supercond. Sci. Technol.*, 2013, **26**, 045020.
305 W. Arpavate, K. Roongraung and S. Chuangchote, in *Green Sustainable Process for Chemical and Environmental Engineering and Science*, eds. Inamuddin, R. Boddula, A. M. Asiri and M. M. Rahman, Elsevier, 2021, pp. 189–203.
306 D. J. Hwang, S.-G. Ryu and C. P. Grigoropoulos, *Nanotechnology*, 2011, **22**, 385303.
307 Y. van de Burgt, *Journal of Laser Applications*, 2014, **26**, 032001.
308 R. Tu, Z. Liu, Q. Xu, S. Zhang, Q. Li, X. Zhang, M. L. Kosinova and T. Goto, *Journal of the European Ceramic Society*, 2023, **43**, 5214–5222.
309 K.-H. Dahmen, in *Encyclopedia of Physical Science and Technology (Third Edition)*, ed. R. A. Meyers, Academic Press, New York, 2003, pp. 787–808.
310 M. R. Baklanov, V. Jousseaume, T. V. Rakhimova, D. V. Lopaev, Yu. A. Mankelevich, V. V. Afanas'ev, J. L. Shohet, S. W. King and E. T. Ryan, *Applied Physics Reviews*, 2019, **6**, 011301.
311 Y. Zhang, Z. Chen, K. Zhang, Z. Feng and H. Zhao, *physica status solidi (RRL) – Rapid Research Letters*, 2021, **15**, 2100202.
312 S. J. C. Irvine, in *Chemical Physics of Thin Film Deposition Processes for Micro- and Nano-Technologies*, ed. Y. Pauleau, Springer Netherlands, Dordrecht, 2002, pp. 199–222.
313 H. Cheng, R. Tu, S. Zhang, M. Han, T. Goto and L. Zhang, *Journal of the European Ceramic Society*, 2017, **37**, 509–515.
314 Y. Fujita, *Journal of Crystal Growth*, 2000, **221**, 382–387.
315 D. Farhanian, G. De Crescenzo and J. R. Tavares, *Langmuir*, 2017, **33**, 1780–1791.
316 C. P. Christensen and K. M. Lakin, *Applied Physics Letters*, 2008, **32**, 254–256.
317 G. Leyendecker, D. Bäuerle, P. Geittner and H. Lydtin, *Applied Physics Letters*, 1981, **39**, 921–923.
318 B. Liu, R. F. Hicks and J. J. Zinck, *Journal of Crystal Growth*, 1993, **129**, 111–118.
319 B. Liu, R. F. Hicks and J. J. Zinck, *Journal of Crystal Growth*, 1992, **123**, 500–518.
320 A. Ruzin and Y. Nemirovsky, *J. Electron. Mater.*, 1993, **22**, 281–288.
321 S. J. C. Irvine, A. Stafford, M. U. Ahmed, A. Brown and H. Kheyrandish, *J. Electron. Mater.*, 1997, **26**, 723–727.
322 M. J. Santos, A. J. Silvestre and O. Conde, *Surface and Coatings Technology*, 2002, **151–152**, 160–164.
323 J. Mazumder and A. Kar, *Theory and Application of Laser Chemical Vapor Deposition*, Springer US, Boston, MA, 1995.
324 C. Duty, D. Jean and W. J. Lackey, *International Materials Reviews*, 2001, **46**, 271–287.
325 H. Sankur, *Thin Solid Films*, 1992, **218**, 161–169.
326 E. Hwang, J. Choi and S. Hong, *Nanoscale*, 2022, **14**, 16065–16076.
327 M. Yang, S. Bai, Q. Xu, J. Li, T. Shimada, Q. Li, T. Goto, R. Tu and S. Zhang, *Diamond and Related Materials*, 2020, **109**, 108094.
328 L. Constantin, L. Fan, C. Azina, K. Keramatnejad, J.-F. Silvain and Y. F. Lu, *Crystal Growth & Design*, 2018, **18**, 2458–2466.
329 Z. Wu, W. Sun, A. Mao, Q. Zhu, X. Chen, X. Zhang, L. Trinh, N. Li, X. Huang, N. Kraiem, J.-F. Silvain, B. Cui and Y. Lu, *Diamond and Related Materials*, 2024, **142**, 110744.
330 L. S. Fan, Y. S. Zhou, M. X. Wang, Y. Gao, L. Liu, J. F. Silvain and Y. F. Lu, *Laser Phys. Lett.*, 2014, **11**, 076002.
331 A. Odusanya, I. Rahaman, P. K. Sarkar, A. Zkria, K. Ghosh and A. Haque, *C*, 2022, **8**, 24.
332 S. Yu, R. Tu and T. Goto, *Journal of the European Ceramic Society*, 2016, **36**, 403–409.
333 Z. Liu, Q. Xu, Q. Sun, J. Li, R. Tu, S. Zhang, M. Yang, Q. Li, Z. Deng, L. Zhang, T. Goto, H. Ohmori and M. Kosinova, *Thin Solid Films*, 2019, **678**, 8–15.
334 H. Katsui, K. Shimoda and M. Hotta, *Ceramics International*, 2023, **49**, 38813–38823.

Open Access Article. Published on 15 2025. Downloaded on 2025/6/3 7:37:30.
This article is licensed under a Creative Commons Attribution 3.0 Unported Licence.

Journal of Materials Chemistry A Accepted Manuscript



Please do not adjust margins

View Article Online
DOI: 10.1039/D5TA01081K

Open Access Article. Published on 15 2025. Downloaded on 2025/6/3 7:37:30.
This article is licensed under a Creative Commons Attribution 3.0 Unported Licence.

Journal of Materials Chemistry A Accepted Manuscript

335 K. An, H.-N. Lee, K.-H. Cho, Y. J. Han and K.-T. Kang, *Organic Electronics*, 2021, **91**, 106078.
336 H. Katsui, K. Harada, Z. Liu, N. Kondo and M. Hotta, *Ceramics International*, 2022, **48**, 31016–31022.
337 B. G. Salazar, C. R. Brewer, L. McElwee-White and A. V. Walker, *Journal of Vacuum Science & Technology A*, 2022, **40**, 023404.
338 B. Sharma and A. Sharma, *Applied Surface Science*, 2021, **567**, 150724.
339 Y. D. Zhao, X. Dong, Z. Z. Ma, Y. T. Zhang, B. Wu, S. W. Zhuang, B. L. Zhang, W. C. Li and G. T. Du, *Journal of Crystal Growth*, 2016, **454**, 30–34.
340 T. Wang, R. Tu, C. Zhang, S. Zhang, K. Wang, T. Goto and L. Zhang, *Journal of Asian Ceramic Societies*, 2021, **9**, 197–207.
341 Y. Hashimoto and A. Ito, *Materials Letters*, 2024, **366**, 136558.
342 R. Tu, Z. Liu, C. Wang, P. Lu, B. Guo, Q. Xu, B.-W. Li and S. Zhang, *RSC Advances*, 2022, **12**, 15555–15563.
343 T.-H. Feng and X.-C. Xia, *Opt. Mater. Express, OME*, 2017, **7**, 1281–1288.
344 Y. Mitsuhashi, S. Matsumoto and A. Ito, *Materials Transactions*, 2023, **64**, 1107–1111.
345 Y. Mitsuhashi, S. Matsumoto and A. Ito, *Journal of the American Ceramic Society*, 2023, **106**, 5140–5146.
346 N. Yamaguchi and A. Ito, *Materials Letters*, 2024, **369**, 136721.
347 W. Li, Y. Zhang, Z. Chen, H. Zhao, S. A. Ringel and A. R. Arehart, *Applied Physics Letters*, 2023, **123**, 112101.
348 E. Güney, J. Karimzadeh Khoei, B. S. Sengul, F. Can and G. Ozaydin Ince, *Journal of Applied Polymer Science*, 2024, **141**, e55210.
349 A. Aufoujal, U. Legrand, J.-L. Meunier and J. R. Tavares, *Catalysts*, 2020, **10**, 534.
350 D. Kim, A. Park, Y. Choi, H. Seong, S. J. Shin, Y. H. Cho and Y. Yoo, *ACS Appl. Polym. Mater.*, 2023, **5**, 8474–8482.
351 K. R. Johnson, P. Arevalo Rodriguez, C. R. Brewer, J. A. Brannaka, Z. Shi, J. Yang, B. Salazar, L. McElwee-White and A. V. Walker, *The Journal of Chemical Physics*, 2016, **146**, 052816.
352 T. Tsuchiya, *Journal of the Ceramic Society of Japan*, 2018, **126**, 889–899.
353 K. K. Gleason, *Advanced Materials*, 2024, **36**, 2306665.
354 H. Akazawa, *Journal of Vacuum Science & Technology A*, 2018, **36**, 041505.
355 H. Akazawa, *Journal of Vacuum Science & Technology B*, 2022, **40**, 062204.
356 H. Nasri Lari, J. Chaouki and J. R. Tavares, *Chemical Engineering Journal*, 2020, **390**, 124526.
357 E. Kasparek, J. R. Tavares, M. R. Wertheimer and P.-L. Girard-Lauriault, *Langmuir*, 2018, **34**, 12234–12243.
358 H. Wang, Y. Zhao, J. Li, Y. Zhou, Z. Shi, C. Yin, S. Zhuang and F. Yang, *Mater. Res. Express*, 2019, **6**, 095914.
359 Xu, Chao-Sheng and Lv, Pei-Wen, *Chinese Journal of Structural Chemistry*, 2021, **40**, 1223–1230.
360 H. Liu, C. R. Brewer, A. V. Walker and L. McElwee-White, *Organometallics*, 2020, **39**, 4565–4574.
361 C. R. Brewer, N. C. Sheehan, J. Herrera, A. V. Walker and L. McElwee-White, *Organometallics*, 2022, **41**, 761–775.
362 C. R. Brewer, O. M. Hawkins, N. C. Sheehan, J. D. Bullock, V. D. Kleiman, A. V. Walker and L. McElwee-White, *Organometallics*, 2019, **38**, 4363–4370.
363 S. P. Murzin, *Applied Sciences*, 2022, **12**, 12133.
364 K. Jeong, J. Lee, I. Byun, M. Seong, J. Park, H. Nam and J. Lee, *Thin Solid Films*, 2017, **626**, 145–153.
365 L.-S. Fan, L. Constantin, D. Li, L. Liu, K. Keramatnejad, C. Azina, X. Huang, H. R. Golgir, Y. Lu, Z. Ahmadi, F. Wang, J. Shield, B. Cui, J.-F. Silvain and Y.-F. Lu, *Light Sci Appl*, 2018, **7**, 17177–17177.
366 S. Kuk, H. K. Nam, Z. Wang and D. J. Hwang, *Journal of Nanoscience and Nanotechnology*, 2018, **18**, 7085–7089.
367 Q. Xu, P. Zhu, Q. Sun, R. Tu, S. Zhang, M. Yang, Q. Li, J. Shi, H. Li, L. Zhang, T. Goto, M. Han, J. Yan, S. Li and H. Ohmori, *Journal of the American Ceramic Society*, 2018, **101**, 1471–1478.
368 H. R. Golgir, Y. S. Zhou, D. Li, K. Keramatnejad, W. Xiong, M. Wang, L. J. Jiang, X. Huang, L. Jiang, J. F. Silvain and Y. F. Lu, *Journal of Applied Physics*, 2016, **120**, 105303.
369 L. Fan, L. Constantin, Z. P. Wu, K. A. McElveen, X. G. Chen, T. He, F. Wang, C. Debiemme-Chouvy, B. Cui, R. Y. Lai, X. Li, J. F. Silvain and Y. F. Lu, *Sci Adv*, 2021, **7**, eabc7547.
370 Y. S. Zhou, L. S. Fan, Z. Q. Xie, L. Jiang, J.-F. Silvain and Y. F. Lu, *Current Opinion in Solid State and Materials Science*, 2015, **19**, 107–114.
371 J. Lasseter, P. D. Rack and S. J. Randolph, *Nanomaterials*, 2023, **13**, 757.
372 Wei Zhang, Xiao-ying Chen, Yong-sheng Ma, Wan-xia Fu, Lei Wang, He Zhou, Zhi-jun Xu, Bo Wang,



This journal is © The Royal Society of Chemistry 20xx

Please do not adjust margins

View Article Online
DOI: 10.1039/D5TA01081K

Open Access Article. Published on 15 2025. Downloaded on 2025/6/3 7:37:30.
This article is licensed under a Creative Commons Attribution 3.0 Unported Licence.

Journal of Materials Chemistry A Accepted Manuscript

and Yi-song Ruan, *Chinese Journal of Liquid Crystals and Displays*, 2019, **34**, 755–763.
373 K. Jeong, J. Lee, I. Byun, M. Seong, J. Park, H. W. Kim, M. J. Kim, J.-H. Kim and J. Lee, *Materials Science in Semiconductor Processing*, 2017, **68**, 245–251.
374 K. An, H.-N. Lee, K. H. Cho, S.-W. Lee, D. J. Hwang and K.-T. Kang, *Micromachines*, 2020, **11**, 88.
375 N. Khosla, J. Narayan and R. Narayan, *Journal of Materials Research*, 2024, **39**, 716–725.
376 S. J. Panchu, S. Dhani, A. Chuturgoon and M. K. Moodley, *Journal of Photochemistry and Photobiology B: Biology*, 2018, **187**, 10–17.
377 S. J. Panchu, M. A. Adebisi, E. Manikandan and M. K. Moodley, *J. Electron. Mater.*, 2020, **49**, 1957–1968.
378 S. J. Panchu, K. Raju, H. C. Swart, B. Chokkalingam, M. Maaza, M. Henini and M. K. Moodley, *ACS Omega*, 2021, **6**, 4542–4550.
379 J. W. Um, S.-Y. Kim, B. H. Lee, J. B. Park and S. Jeong, *Carbon*, 2020, **169**, 163–171.
380 Z. Liu, Y. Cai, R. Tu, Q. Xu, M. Hu, C. Wang, Q. Sun, B.-W. Li, S. Zhang, C. Wang, T. Goto and L. Zhang, *Carbon*, 2021, **175**, 377–386.
381 J. Lasseter, P. D. Rack and S. J. Randolph, *ACS Appl. Nano Mater.*, 2022, **5**, 10890–10899.
382 Lisha F., Fan L., Guolong W., Kovalenko V. S. and Jianhua Y., *OEE*, 2022, **49**, 210333–29.
383 C. Zhang, J. Zhang, K. Lin and Y. Huang, *Review of Scientific Instruments*, 2017, **88**, 053907.
384 B. Fotovvati, A. Dehghanghadikolaei and N. Namdari, *Particulate Science and Technology*, 2021, **39**, 738–747.
385 T. Goto, *J. Wuhan Univ. Technol.-Mat. Sci. Edit.*, 2016, **31**, 1–5.
386 Y. Zhang, Y. Jiao, C. Li, C. Chen, J. Li, Y. Hu, D. Wu and J. Chu, *Int. J. Extrem. Manuf.*, 2020, **2**, 032002.
387 A. Ito, *Journal of the Ceramic Society of Japan*, 2021, **129**, 646–653.
388 S. Bai, L. Ruan, H. Chen, Y. Du, H. Deng, N. Dai and Y. Tang, *Chemical Engineering Journal*, 2024, **493**, 152805.
389 Z. Wu, A. Mao, L. Wadle, X. Huang, N. Kraiem, J.-F. Silvain, B. Cui and Y. Lu, *Diamond and Related Materials*, 2024, **149**, 111549.
390 Z. Q. Xie, J. Bai, Y. S. Zhou, Y. Gao, J. Park, T. Guillemet, L. Jiang, X. C. Zeng and Y. F. Lu, *Sci Rep*, 2014, **4**, 4581.
391 Q. Xu, Z. Deng, Q. Sun, R. Tu, S. Zhang, M. Yang, Q. Li, L. Zhang, T. Goto and H. Ohmori, *Carbon*, 2018, **139**, 76–84.
392 Q. Sun, R. Tu, Q. Xu, C. Zhang, J. Li, H. Ohmori, M. Kosinova, B. Basu, J. Yan, S. Li, T. Goto, L. Zhang and S. Zhang, *Journal of Power Sources*, 2019, **444**, 227308.
393 R. Tu, Z. Hu, Q. Xu, L. Li, M. Yang, Q. Li, J. Shi, H. Li, S. Zhang, L. Zhang, T. Goto, H. Ohmori, M. Kosinova and B. Basu, *Journal of Asian Ceramic Societies*, 2019, **7**, 312–320.
394 J. S. Ten, M. Sparkes and W. O'Neill, in *Laser Applications in Microelectronic and Optoelectronic Manufacturing (LAMOM) XXII*, SPIE, 2017, vol. 10091, pp. 52–58.
395 M. Trippel, J. Bläsing, M. Wieneke, A. Dadgar, G. Schmidt, F. Bertram, J. Christen and A. Strittmatter, *Review of Scientific Instruments*, 2022, **93**, 113904.
396 H. Rabiee Golgir, D. W. Li, K. Keramatnejad, Q. M. Zou, J. Xiao, F. Wang, L. Jiang, J.-F. Silvain and Y. F. Lu, *ACS Appl. Mater. Interfaces*, 2017, **9**, 21539–21547.
397 Y. Zhang, V. G. Thirupakuzi Vangipuram, K. Zhang and H. Zhao, *Applied Physics Letters*, 2023, **122**, 162101.
398 C. S. Torres-Castillo and J. R. Tavares, *The Canadian Journal of Chemical Engineering*, 2023, **101**, 1410–1420.
399 A. Khlyustova, Y. Cheng and R. Yang, *Journal of Materials Chemistry B*, 2020, **8**, 6588–6609.
400 R. Fan and T. L. Andrew, *J. Electrochem. Soc.*, 2021, **168**, 077518.
401 C. A. Dorval Dion and J. R. Tavares, *Powder Technology*, 2013, **239**, 484–491.
402 S. Hosseininasab, N. Faucheux, G. Soucy and J. R. Tavares, *J Nanopart Res*, 2019, **21**, 114.
403 S. Yousefi, M. A. Makarem, E. Rahimpour and M. R. Rahimpour, in *Advances in Synthesis Gas : Methods, Technologies and Applications*, eds. M. R. Rahimpour, M. A. Makarem and M. Meshksar, Elsevier, 2023, vol. 3, pp. 395–410.
404 H. Nasri Lari, D. Farhanian, D. C. Boffito, G. S. Patience, G. De Crescenzo, J. Chaouki and J. R. Tavares, *Catalysis Communications*, 2017, **100**, 19–23.
405 V. Labonté, A. Marion, N. Virgilio and J. R. Tavares, *Ind. Eng. Chem. Res.*, 2016, **55**, 7362–7372.
406 D. Farhanian, G. De Crescenzo and J. R. Tavares, *Sci Rep*, 2018, **8**, 12223.
407 S. Hosseininasab, N. Faucheux, G. Soucy and J. R. Tavares, *Chemical Engineering Journal*, 2017, **325**, 101–113.
408 A. Bérard, G. S. Patience, G. Chouinard and J. R. Tavares, *Sci Rep*, 2016, **6**, 31574.



Please do not adjust margins

Open Access Article. Published on 15 2025. Downloaded on 2025/6/3 7:37:30.
This article is licensed under a Creative Commons Attribution 3.0 Unported Licence.

Journal of Materials Chemistry A Accepted Manuscript


409 P. R. Riley, P. Joshi, N. Khosla, R. J. Narayan and J. Narayan, *Carbon*, 2022, **196**, 972–978.

410 M. J. Jeon, S.-K. Hyeong, H. Y. Jang, J. Mun, T.-W. Kim, S. Bae and S.-K. Lee, *Nanomaterials*, 2023, **13**, 2937.

411 D. A. Boyd, L. Greengard, M. Brongersma, M. Y. El-Naggar and D. G. Goodwin, *Nano Lett.*, 2006, **6**, 2592–2597.

412 J. Svensson, N. M. Bulgakova, O. A. Nerushev and E. E. B. Campbell, *Phys. Rev. B*, 2006, **73**, 205413.

413 D. Dey and A. K. Tiwari, *ACS Omega*, 2020, **5**, 17857–17867.

414 I. Angelov, L. Zaharieva and L. Antonov, *Molecules*, 2023, **28**, 695.

415 N. Wang and L. Weatherley, *Current Opinion in Chemical Engineering*, 2023, **39**, 100895.

416 S. Xu, R. Eisenberg, Z. Song and H. Huang, *Phys. Rev. E*, 2023, **108**, 064413.

417 F. Che, J. T. Gray, S. Ha, N. Kruse, S. L. Scott and J.-S. McEwen, *ACS Catal.*, 2018, **8**, 5153–5174.

418 I. Lyubinetsky, S. Mezhenny, W. J. Choyke and J. T. Yates Jr., *Journal of Vacuum Science & Technology A*, 1999, **17**, 1445–1450.

419 S. Yugo, T. Kanai, T. Kimura and T. Muto, *Applied Physics Letters*, 1991, **58**, 1036–1038.

420 V. S. Jayaseelan and R. N. Singh, *Journal of Applied Physics*, 2023, **133**, 155302.

421 A. Saravanan, B.-R. Huang, K. J. Sankaran, S. Kunuku, C.-L. Dong, K.-C. Leou, N.-H. Tai and I.-N. Lin, *ACS Appl. Mater. Interfaces*, 2014, **6**, 10566–10575.

422 N. M. Hwang, *Non-Classical Crystallization of Thin Films and Nanostructures in CVD and PVD Processes*, Springer Netherlands, Dordrecht, 2016, vol. 60.

423 J. J. Alcantar-Peña, E. de Obaldia, J. Montes-Gutierrez, K. Kang, M. J. Arellano-Jimenez, J. E. Ortega Aguilar, G. P. Suchy, D. Berman-Mendoza, R. Garcia, M. J. Yacaman and O. Auciello, *Diamond and Related Materials*, 2017, **78**, 1–11.

424 L. Osman, A. Zkria, A. M. Ali, S. Nagano, H. Naragino and T. Yoshitake, *Appl. Phys. Express*, 2023, **16**, 075501.

425 W. Wang, S. Yang, B. Liu, X. Hao, J. Han, B. Dai and J. Zhu, *Carbon Lett.*, 2023, **33**, 517–530.

426 A. Saravanan, B. R. Huang, K. J. Sankaran, G. Keiser, J. Kurian, N. H. Tai and I. N. Lin, *Journal of Applied Physics*, 2015, **117**, 215307.

427 W.-K. Youn, C.-S. Kim, J.-Y. Lee, S.-S. Lee and N.-M. Hwang, *J. Phys. Chem. C*, 2012, **116**, 25157–25163.

428 Y. Zhang, A. Chang, J. Cao, Q. Wang, W. Kim, Y. Li, N. Morris, E. Yenilmez, J. Kong and H. Dai, *Applied Physics Letters*, 2001, **79**, 3155–3157.

429 Appendix B - Bias Enhanced Nucleation, https://www.chm.bris.ac.uk/pt/diamond/stuthesis/appendb.htm#_ednref15, (accessed February 12, 2024).

430 D.-S. Kim and N.-M. Hwang, *J. Phys. D: Appl. Phys.*, 2018, **51**, 463002.

431 J. Wang, J.-H. Park, A.-Y. Lu and J. Kong, *J. Am. Chem. Soc.*, 2022, **144**, 22925–22932.

432 M.-S. Chae, T. H. Lee, K. R. Son, Y. W. Kim, K. S. Hwang and T. G. Kim, *Nanoscale Horiz.*, 2019, **4**, 610–618.

433 Q.-J. Feng, H.-W. Liang, Y.-Y. Mei, J.-Y. Liu, C. C. Ling, P.-C. Tao, D.-Z. Pan and Y.-Q. Yang, *J. Mater. Chem. C*, 2015, **3**, 4678–4682.

434 H. Bae, K. Sasai, H. Suzuki and H. Toyoda, *Vacuum*, 2021, **192**, 110429.

435 J. Langer, V. Cimalla, V. Lebedev, L. Kirste, M. Prescher, T. Luo, J. Jeske and O. Ambacher, *physica status solidi (a)*, 2022, **219**, 2100756.

436 K. An, S. Zhang, S. Shao, J. Liu, J. Wei, L. Chen, Y. Zheng, Q. Liu and C. Li, *Plasma Sci. Technol.*, 2022, **24**, 045502.

437 V. Beladiya, M. Becker, T. Faraz, W. M. M. (Erwin) Kessels, P. Schenk, F. Otto, T. Fritz, M. Gruenewald, C. Helbing, K. D. Jandt, A. Tünnermann, M. Sierka and A. Szeghalmi, *Nanoscale*, 2020, **12**, 2089–2102.

438 B. Wang, D. Yang, X. Zhu, Y. Zhao, S. Wang, J. Zhu and M. Zhai, *Processes*, 2022, **10**, 2665.

439 T. Yoshimura, S. Tatsuura and W. Sotoyama, *Thin Solid Films*, 1992, **207**, 9–11.

440 S. Tatsuura, W. Sotoyama and T. Yoshimura, *Applied Physics Letters*, 1992, **60**, 1661–1663.

441 S. Tatsuura, W. Sotoyama, K. Motoyoshi, A. Matsuura, T. Hayano and T. Yoshimura, *Applied Physics Letters*, 1993, **62**, 2182–2184.

442 N. Hu, Y. Wang, J. Li, Q. Wei, Y. Jiang, L. Ma, Z. Yu, K. Zhou and H. Long, *Surface and Coatings Technology*, 2019, **359**, 459–467.

443 B. Peng, S. Jiang, Y. Zhang and J. Zhang, *Carbon*, 2011, **49**, 2555–2560.

444 N. Panjawi, A. Naik, M. E. A. Warwick, G. Hyett and R. Binions, *Chemical Vapor Deposition*, 2012, **18**, 102–106.

445 A. J. T. Naik, M. E. A. Warwick, S. J. A. Moniz, C. S. Blackman, I. P. Parkin and R. Binions, *J. Mater. Chem. A*, 2013, **1**, 1827–1833.




This journal is © The Royal Society of Chemistry 20xx

Please do not adjust margins

View Article Online
DOI: 10.1039/D5TA01081K

Open Access Article. Published on 15 2025. Downloaded on 2025/6/3 7:37:30.
This article is licensed under a Creative Commons Attribution 3.0 Unported Licence.

Journal of Materials Chemistry A Accepted Manuscript


446 M. E. A. Warwick, I. Ridley and R. Binions, *Surface and Coatings Technology*, 2013, **230**, 163–167.
447 L. Romero and R. Binions, *Surface and Coatings Technology*, 2013, **230**, 196–201.
448 A. J. T. Naik, C. Bowman, N. Panjwani, M. E. A. Warwick and R. Binions, *Thin Solid Films*, 2013, **544**, 452–456.
449 L. Romero, A. B. Jorge, P. F. McMillan and R. Binions, *ECS J. Solid State Sci. Technol.*, 2014, **3**, N107.
450 Qiu-Ju F., Fang L., Tong-Tong L., Yun-Zheng L., Bo S., Meng-Ke L. and Hong-Wei L., *Acta Phys. Sin.*, 2018, **67**, 218101–218101.
451 I. Top, R. Binions, M. E. A. Warwick, C. W. Dunnill, M. Holdynski and I. Abrahams, *J. Mater. Chem. C*, 2018, **6**, 4485–4493.
452 M. E. A. Warwick, I. Ridley and R. Binions, *Solar Energy Materials and Solar Cells*, 2016, **157**, 686–694.
453 L. Romero, A.-B. Jorge-Sobrido, P. F. McMillan and R. Binions, *Thin Solid Films*, 2015, **584**, 320–325.
454 L. Romero, C. Piccirillo, P. M. L. Castro, C. Bowman, M. E. A. Warwick and R. Binions, *Chemical Vapor Deposition*, 2015, **21**, 63–70.
455 W.-J. Lee, S.-K. Rha, S.-Y. Lee and C.-O. Park, *J. Electrochem. Soc.*, 1997, **144**, 683.
456 E. Pawlas-Foryst, W. Przybyło, M. Kopyto and K. Fitzner, *Materials Research Bulletin*, 2001, **36**, 915–923.
457 Y.-T. Jang, J.-H. Ahn, B.-K. Ju and Y.-H. Lee, *Solid State Communications*, 2003, **126**, 305–308.
458 G. Shaw, I. P. Parkin, K. F. E. Pratt and D. E. Williams, *J. Mater. Chem.*, 2005, **15**, 149–154.
459 M. E. A. Warwick, I. Ridley and R. Binions, *Journal of Nanoscience and Nanotechnology*, 2011, **11**, 8158–8162.
460 J. Crane, M. Warwick, R. Smith, N. Furlan and R. Binions, *J. Electrochem. Soc.*, 2010, **158**, D62.
461 R. Naeem, S. Ahmed, K. M. Lo, W. J. Basirun, R. Yahya, M. Misran, T. A. N. Peiris, J. S. Sagu, K. G. U. Wijayantha, A. K. Thapa, G. U. Sumanasekera and M. Mazhar, *Chemical Vapor Deposition*, 2015, **21**, 360–368.
462 J.-Y. Lee and J.-H. Yoon, *Solid State Communications*, 2004, **132**, 627–630.
463 R. Naeem, R. Yahya, A. Pandikumar, H. N. Ming and M. Mazhar, *J Mater Sci: Mater Electron*, 2017, **28**, 868–877.
464 L. Issman, P. A. Kloza, J. Terrones Portas, B. Collins, A. Pendashteh, M. Pick, J. J. Vilatela, J. A. Elliott and A. Boies, *ACS Nano*, 2022, **16**, 9583–9597.
465 S. Zhao, Q. Feng, C. Gao, D. Wang, Y. Xing, J. Xie, Z. Dong, M. Li and H. Liang, *Materials Science in Semiconductor Processing*, 2020, **116**, 105142.
466 S.-H. Park, J.-W. Park, S.-M. Yang, K.-H. Kim and N.-M. Hwang, *J. Phys. Chem. C*, 2015, **119**, 25047–25052.
467 S. Park, J. Jung, K. Kim, K. Kim and N. Hwang, *Crystal Growth & Design*, 2018, **18**, 5816–5823.
468 D. Kim, D.-Y. Kim, J.-H. Kwon and N.-M. Hwang, *Coatings*, 2020, **10**, 726.
469 A. Gamboa, L. M. Marques and E. C. Fernandes, *Diamond and Related Materials*, 2021, **113**, 108274.
470 C. Luo, G. Liu and M. Zhang, *Front. Mater. Sci.*, 2019, **13**, 270–276.
471 C. Liao, Y. Zhang and C. Pan, *Journal of Applied Physics*, 2012, **112**, 114310.
472 H. Tani, R. Lu, S. Koganezawa and N. Tagawa, *IEEE Transactions on Magnetics*, 2017, **53**, 1–6.
473 N. M. Hwang, in *Non-Classical Crystallization of Thin Films and Nanostructures in CVD and PVD Processes*, ed. N. M. Hwang, Springer Netherlands, Dordrecht, 2016, pp. 261–289.
474 J.-W. Park, K.-H. Kim and N.-M. Hwang, *Advanced Materials Letters*, 2018, **9**, 638–642.
475 S.-W. Yoo, N.-M. Hwang, S.-J. You, J.-H. Kim and D.-J. Seong, *J Nanopart Res*, 2017, **19**, 374.
476 T. Sharda, M. Umeno, T. Soga and T. Jimbo, *Applied Physics Letters*, 2000, **77**, 4304–4306.
477 W. Chen, C. Xiao, Q. Yang, A. Moewes and A. Hirose, *Can. J. Phys.*, 2005, **83**, 753–759.
478 J.-I. Lee and N.-M. Hwang, *Carbon*, 2008, **46**, 1588–1592.
479 E. Plaza, H. Briceño-Fuenmayor, J. Arévalo, R. Atencio and L. Corredor, *J Nanopart Res*, 2015, **17**, 246.
480 H. Kanayama, K. Ikesugi, K. Shimanaka and H. Sato, *Diamond and Related Materials*, 2012, **24**, 83–87.
481 J. Zhang and C. Pan, *Journal of Alloys and Compounds*, 2010, **495**, 93–96.
482 S. A. Linnik, A. V. Gaydaychuk, A. S. Mitulinsky and S. P. Zenkin, *Materials Letters*, 2022, **324**, 132670.
483 K. Ishikawa, *Advanced Engineering Materials*, 2024, **26**, 2400679.
484 A. Roy and D. Das, *Diamond and Related Materials*, 2018, **88**, 204–214.
485 D. Das and A. Roy, *Applied Surface Science*, 2020, **515**, 146043.
486 M. G. Cuxart, I. Šics, A. R. Goñi, E. Pach, G. Sauthier, M. Paradinas, M. Foerster, L. Aballe, H. M.

View Article Online
DOI: 10.1039/D5TA01981K

Open Access Article. Published on 15 2025. Downloaded on 2025/6/3 7:37:30.
This article is licensed under a Creative Commons Attribution 3.0 Unported Licence.

Journal of Materials Chemistry A Accepted Manuscript

Fernandez, V. Carlino and E. Pellegrin, *Carbon*, 2017, **117**, 331–342.
487 Y. Qi, B. Deng, X. Guo, S. Chen, J. Gao, T. Li, Z. Dou, H. Ci, J. Sun, Z. Chen, R. Wang, L. Cui, X. Chen, K. Chen, H. Wang, S. Wang, P. Gao, M. H. Rummeli, H. Peng, Y. Zhang and Z. Liu, *Advanced Materials*, 2018, **30**, 1704839.
488 K. S. A. Butcher, V. Georgiev, D. Georgieva, R. Gergova, P. Terziyska and P. W. Binsted, *Coatings*, 2022, **12**, 1581.
489 T. Yoshikawa, D. Herrling, F. Meyer, F. Burmeister, C. E. Nebel, O. Ambacher and V. Lebedev, *Journal of Vacuum Science & Technology B*, 2019, **37**, 021207.
490 J. Reiprich, N. A. Isaac, L. Schlag, T. Kups, M. Hopfeld, G. Ecke, T. Stauden, J. Pezoldt and H. O. Jacobs, *ACS Nano*, 2020, **14**, 12885–12894.
491 L. Shi, F. Xu, J. Gao, M. Yuen, S. Sun, J. Xu, K. Jia and D. Zuo, *Diamond and Related Materials*, 2020, **109**, 108098.
492 J. Geiser and M. Arab, *Special Topics & Reviews in Porous Media: An International Journal*, 2010, **1**, 215–229.
493 L. Rudniak, *Computers & Chemical Engineering*, 1998, **22**, S755–S758.
494 D. Li-Fang, C. Jun-Ying, D. Guo-Yi and S. Yong, *Chinese Phys.*, 2002, **11**, 419.
495 D. Lifang, M. Boqin, S. Yong and W. Zhijun, *Plasma Sci. Technol.*, 2005, **7**, 2845.
496 M. Saeidi, M. Vaezzadeh and F. Badakhshan, *Physica B: Condensed Matter*, 2011, **406**, 1038–1040.
497 M. Saeidi, *Physica E: Low-dimensional Systems and Nanostructures*, 2015, **70**, 225–230.
498 M. Yan, T. Zhang, B. Wang, J. Liu, X. Liang, Y. Xu and F. Yi, *Journal of Applied Physics*, 2023, **134**, 155303.
499 V. Beladiya, T. Faraz, P. Schmitt, A.-S. Munser, S. Schröder, S. Riese, C. Mühlig, D. Schachtler, F. Steger, R. Botha, F. Otto, T. Fritz, C. van Helvoirt, W. M. M. Kessels, H. Gargouri and A. Szeghalmi, *ACS Appl. Mater. Interfaces*, 2022, **14**, 14677–14692.
500 B. Reeja-Jayan and J. Luo, *MRS Bulletin*, 2021, **46**, 26–35.
501 J. W. Strand, J. Cottom, L. Larcher and A. L. Shluger, *Phys. Rev. B*, 2020, **102**, 014106.
502 A. Ansh, U. Patbhaje, J. Kumar, A. Meersha and M. Shrivastava, *Commun Mater*, 2023, **4**, 1–11.
503 W.-K. Youn, S.-S. Lee, J.-Y. Lee, C.-S. Kim, N.-M. Hwang and S. Iijima, *J. Phys. Chem. C*, 2014, **118**, 11946–11953.
504 M. G. Byun, J. W. Yang, J. H. Park, N. M. Hwang, J. Park and B. D. Yu, *Crystal Growth & Design*, 2022, **22**, 2490–2498.
505 M. G. Byun, J. H. Park, J. W. Yang, N. M. Hwang, J. Park and B. D. Yu, *Electron. Mater. Lett.*, 2023, **19**, 218–228.
506 M. Yamaguchi and Y. Tanimoto, Eds., in *Magneto-Science: Magnetic Field Effects on Materials: Fundamentals and Applications*, Springer, Berlin, Heidelberg, 2006, pp. 1–40.
507 U. E. Steiner and T. Ulrich, *Chem. Rev.*, 1989, **89**, 51–147.
508 A. A. J. Kipriyanov and P. A. Purtov, *Bulletin of the Korean Chemical Society*, 2012, **33**, 1009–1014.
509 Y. Ma, K. Watanabe, S. Awaji and M. Motokawa, *Journal of Crystal Growth*, 2001, **233**, 483–489.
510 Y. Lu, C. Yang, H. Wang, L. Ma, M. Xu and L. Xi, *Vacuum*, 2023, **211**, 111912.
511 Z. Wu, Y. Zhang, Y. Shen, W. Zhang and G. Shao, *Advanced Materials Interfaces*, 2020, **7**, 2000854.
512 M. Baghgar, Y. Abdi and E. Arzi, *Eur. Phys. J. Appl. Phys.*, 2009, **48**, 20603.
513 H. Yasuda, *Magneto Luminous Chemical Vapor Deposition*, CRC Press, Boca Raton, 2012.
514 M. Taniguchi, M. Hirose, T. Hamasaki and Y. Osaka, *Applied Physics Letters*, 2008, **37**, 787–788.
515 T. Hamasaki, H. Kurata, M. Hirose and Y. Osaka, *Applied Physics Letters*, 2008, **37**, 1084–1086.
516 T. H. Yuzuriha, W. E. Mlynko and D. W. Hess, *Journal of Vacuum Science & Technology A*, 1985, **3**, 2135–2140.
517 Z. Sun, X. Shi and E. Liu, *Thin Solid Films*, 1999, **355–356**, 146–150.
518 S. R. P. Silva, K. J. Clay, S. P. Speakman and G. A. J. Amaratunga, *Diamond and Related Materials*, 1995, **4**, 977–983.
519 J. Schwan, S. Ulrich, K. Jung, H. Ehrhardt, R. Samlenski and R. Brenn, *Diamond and Related Materials*, 1995, **4**, 304–308.
520 C. Luo, D. Wan, J. Jia, D. Li, C. Pan and L. Liao, *Nanoscale*, 2016, **8**, 13017–13024.
521 G.-L. Tian, J.-Q. Huang, J. Li, Q. Zhang and F. Wei, *Carbon*, 2016, **108**, 404–411.
522 C. B. Lugod and J. Auresenia, *MATEC Web Conf.*, 2019, **268**, 05004.
523 X. Liu, K. Wen, X. Duan, C. Wang and H. Long, *Vacuum*, 2023, **218**, 112661.
524 F. Kwok, X. Du, Z. Sun, M. Ng, Q. Liu, LL Fan, W. Yip, D. Kwok and S. To, *Surface and Coatings Technology*, 2024, **483**, 130802.



This journal is © The Royal Society of Chemistry 20xx

Please do not adjust margins

View Article Online
DOI: 10.1039/D5TA01081K

525 Y. Wang, J. Li, H. Long, H. Luo, B. Zhou, Y. Xie, S. Li, Q. Wei and Z. Yu, *Surface and Coatings Technology*, 2016, **292**, 49–53.
526 F. M. Kwok, X. Du, Z. Sun, M. C. Ng, W. S. Yip, K. Y. D. Kwok and S. To, *Surface and Coatings Technology*, 2025, **495**, 131588.
527 D. Wei, Y. Liu, L. Cao, L. Fu, X. Li, Y. Wang and G. Yu, *J. Am. Chem. Soc.*, 2007, **129**, 7364–7368.
528 C. Luo, Q. Fu and C. Pan, *Sci Rep*, 2015, **5**, 9062.
529 A. Hamasaki, A. Furuse, J. Uchimura, Y. Takashima and S. Ozeki, *International Journal of Applied Electromagnetics and Mechanics*, 2023, **71**, S393–S401.
530 D. Stadler, D. N. Mueller, T. Brede, T. Duchoň, T. Fischer, A. Sarkar, M. Giesen, C. M. Schneider, C. A. Volkert and S. Mathur, *J. Phys. Chem. Lett.*, 2019, **10**, 6253–6259.
531 A. Raauf, J. Leduc, M. Frank, D. Stadler, D. Graf, M. Wilhelm, M. Grosch and S. Mathur, *Inorg. Chem.*, 2021, **60**, 1915–1921.
532 M. Pyeon, V. Rauch, D. Stadler, M. Gürsoy, M. Deo, Y. Gönüllü, T. Fischer, T. Hwang and S. Mathur, *Advanced Engineering Materials*, 2019, **21**, 1900195.
533 D. Stadler, T. Brede, D. Schwarzbach, F. Maccari, T. Fischer, O. Gutfleisch, C. A. Volkert and S. Mathur, *Nanoscale Adv.*, 2019, **1**, 4290–4295.
534 P. Tutacz, D. Stadler, T. Karimpour, T. Duchoň, S. Cramm, C. M. Schneider, T. Fischer, D. N. Mueller and S. Mathur, *Chem. Mater.*, 2023, **35**, 8050–8056.
535 H. Lee, Z. T. Aytuna, A. Bhardwaj, M. Wilhelm, K. Lê, B. May, D. N. Mueller and S. Mathur, *Advanced Engineering Materials*, 2023, **25**, 2300021.
536 M. Frank, L. Jürgensen, J. Leduc, D. Stadler, D. Graf, I. Gessner, F. Zajusch, T. Fischer, M.-A. Rose, D. N. Mueller and S. Mathur, *Inorg. Chem.*, 2019, **58**, 10408–10416.
537 R. B. Little and R. Goddard, *Journal of Applied Physics*, 2004, **95**, 2702–2712.
538 X. You, Z. Yu, L. Shi and L. Wang, *Journal of Crystal Growth*, 2009, **311**, 4675–4678.
539 H. Long, S. Li, H. Luo, Y. Wang, Q. P. Wei and Z. M. Yu, *Applied Surface Science*, 2015, **353**, 548–552.
540 X. Liu, K. Wen, X. Duan, C. Wang and H. Long, *Coatings*, 2023, **13**, 441.
541 Y. J. Kim, Y. S. Choi, K. S. Shin, S. H. Cho, I. S. Choi and J. G. Han, *Current Applied Physics*, 2010, **10**, S354–S356.
542 D.-H. Kim, H.-S. Jang, H.-R. Lee, C.-D. Kim and H.-D. Kang, *Applied Physics Letters*, 2004, **85**, 109–111.
543 A. Mettenbörger, T. Singh, A. P. Singh, T. T. Järvi, M. Moseler, M. Valldor and S. Mathur, *International Journal of Hydrogen Energy*, 2014, **39**, 4828–4835.
544 S. Awaji, K. Watanabe, Y. Ma and M. Motokawa, *Physica B: Condensed Matter*, 2001, **294–295**, 482–485.
545 M. Tahashi, K. Sassa and S. Asai, *Materials Transactions*, 2002, **43**, 2813–2817.
546 Y. Wu, H. Tao, S. Su, H. Yue, H. Li, Z. Zhang, Z. Ni and X. Chen, *Sci Rep*, 2017, **7**, 46583.
547 P. M. R. https://www.polarismarketresearch.com, Chemical Vapor Deposition Market Size, Growth Report, By 2032, https://www.polarismarketresearch.com/industry-analysis/chemical-vapor-deposition-cvd-market, (accessed December 3, 2024).

Open Access Article. Published on 15 2025. Downloaded on 2025/6/3 7:37:30.
This article is licensed under a Creative Commons Attribution 3.0 Unported Licence.

Journal of Materials Chemistry A Accepted Manuscript



Please do not adjust margins

View Article Online
DOI: 10.1039/D5TA01081K

**Data availability Statement**

No primary research results, software or code have been included and no new data were generated or analysed as part of this review.

Open Access Article. Published on 15 2025. Downloaded on 2025/6/3 7:37:30.
This article is licensed under a Creative Commons Attribution 3.0 Unported Licence.

Journal of Materials Chemistry A Accepted Manuscript